BERGISCHE UNIVERSITÄT WUPPERTAL

Fachbereich E
Elektrotechnik, Informationstechnik, Medientechnik

Lehrstuhl für Theoretische Elektrotechnik

Application of Non-Linear Microvaristor-Filled Materials in High-Voltage Devices and Algorithmic Optimization of High-Voltage Simulations Based on Surrogate Models

M.Sc. Hanyu Ye
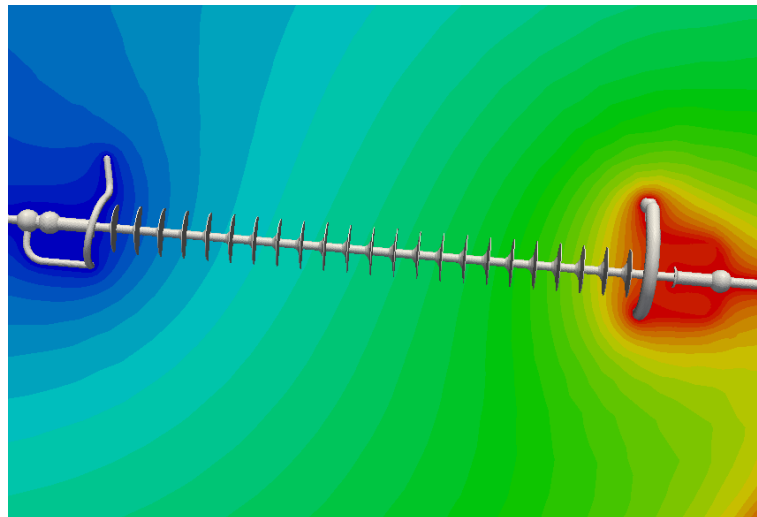
Application of Non-Linear Microvaristor-Filled Materials in High-Voltage Devices and Algorithmic Optimization of High-Voltage Simulations Based on Surrogate Models

Vom Fachbereich Elektrotechnik, Informationstechnik, Medientechnik
der Bergischen Universität Wuppertal
zur Erlangung
des akademischen Grades eines Doktor-Ingenieurs
genehmigte

Dissertation

M.Sc. Hanyu Ye
geboren am 10.09.1983 in Fujian, China

Referent:	Prof. Dr. rer. nat. Markus Clemens
Koreferent:	Prof. Dr.-Ing. Bernd Tibken
Tag der Einreichung:	17. Januar 2015
Tag der mündlichen Prüfung:	17. April 2015

Die Dissertation kann wie folgt zitiert werden:

Acknowledgment

I would like to express my sincere appreciation to my supervisor Prof. Dr. rer. nat. Markus Clemens for providing me the opportunity to perform this research at his Chair of Electromagnetic Theory at the Bergische Universität Wuppertal, the financial support and academic advices. I also want to thank Prof. Dr.-Ing. Bernd Tibken for his interest in my research and for agreeing to be the second supervisor.

I am very grateful to my colleagues Dipl.-Phys. Daniel Schmidthäusler, M.Sc. Oliver Spathmann, M.Sc. Carsten Cimala, M.Sc. Martin Zang, M.Sc. Simon Runke and M.Sc. Jennifer Dutiné for the great working atmosphere and wonderful time we spent together. With them I shared not only academic opinions but also life experience. A lot of events on which we played and discussed together are precious memories in my life. I also want to show my gratitude to Dr. Streckert whose academic expertise motivates me a lot as a young scientist. I also want to thank Mrs. Christa Kelly a lot for her patience, help and useful advices about the daily life.

I especially want to thank BU LIKE, Lapp Insulators GmbH in Wunsiedel for providing me the opportunity to participate in the research project, which helped me a lot to complete my thesis. In particular, I want to thank Dr. Jens Seifert for his interest in my work, encouragement and invaluable discussions. Special thanks go to Dr. Jan Schulte-Fischedick, Dr. Jürgen Witt, Mr. Heinz Denndörfer and Mrs. Kerstin Knoch for giving me an overview about the productions of high-voltage insulators and for sharing their knowledge. The great cooperation with them makes my stay at Lapp Insulators an unforgettable memory.

Special thanks to my family. Words can not express how grateful I am to my parents and my parents in law for their selfless help and endless support especially during the difficult days. I would also want to thank my friends who supported me in writing and motivated me to strive towards my goal. Last but not least, I want to express my deep gratitude to my husband Dipl.-Phys. Dipl.-Math. Eike Scholz for his patience, encouragement and support whenever it is needed.

Contents

Symbols

$\vec{A}$	vector potential
$\mathbf{B}_\varepsilon$	stiffness matrix of the linear permittivity
c	speed of light in vacuum
C	scalar value
C_{dry}	capacity of dry bands
C_{ins}	capacity of the silicone layer
$\vec{D}_o$	electric displacement field with $\vec{D}_o = \varepsilon \vec{E}_o$
d	diameter of a finite spatial domain Ω; dimension; distance between the corona ring and the energized end fitting
$\vec{E}$	electric field
$\vec{E}_i$	solenoidal part of the electric field $\vec{E}$ with $\vec{E}_i = -j\omega\vec{A}$
$\vec{E}_o$	irrotational part of the electric field $\vec{E}$ with $\vec{E}_o = -\mathrm{grad}\varphi$
E	magnitude of the electric field
$E_{\mathrm{b,powder}}$	switching electric field strength of microvaristor powder
$E_{\mathrm{b,composite}}$	switching electric field strength of microvaristor-filled composite
$|\vec{E}|$	magnitude of the electric field
E_a	activation energy
E_{max}	maximal electric field strength
f	objective function
$\hat{f}$	approximation of the objective function f
f^*	target objective function at the point $\mathbf{x}^*$
f_c	coarse cheap objective function
f_e	accurate expensive objective function
$\vec{H}$	magnetic field
$|\vec{H}|$	magnitude of the magnetic field
j	imaginary unit $j^2 = -1$
J	magnitude of the current density
$\vec{J}$	total current density
$\vec{J}_s$	impressed current density of the given source
I	current
k	scalar value

K	Lipschitz constant
k_B	Boltzmann constant
$\mathbf{K}_k(\mathbf{\Phi})$	stiffness matrix of the non-linear electrical conductivity
$\mathbf{p}$	system parameter of Kriging models
$\mathbf{r}$	correlation vector of the point $\mathbf{x}^*$ to the observed points $\mathbf{X}$
$\mathbf{R}$	$n \times n$ correlation matrix
R_{major}	major ring radius
R_{minor}	radius of the ring tube
R_{pol}	resistance of the wet polluted layer
$R_{\mu\mathrm{Var}}$	non-linear resistance of the microvaristor layer
T	absolute temperature in Kelvin
U	voltage
U_b	switching voltage
U_n	nominal voltage of a three-phase AC system
U_{peak}	peak value of a phase voltage with $U_{\mathrm{peak}} = U_{\mathrm{rms}} \cdot \sqrt{2}$
U_{rms}	effective phase voltage with $U_{\mathrm{rms}} = U_n/\sqrt{3}$
w	angular frequency; weighted parameter for the WEIF
w_e	electric energy density
w_m	magnetic energy density
w_q	upper angular frequency limit for validity range of slowly varying-fields
x^*	an unobserved point; new hypothetical point in one-stage approach
$(\mathbf{X}, \mathbf{y})$	the sample points $\mathbf{X}$ with the function values $\mathbf{y}$ at these points
$(\mathbf{X_c}, \mathbf{y_c})$	low-fidelity data for Co-Kriging models
$(\mathbf{X_e}, \mathbf{y_e})$	high-fidelity data for Co-Kriging models
y_{min}	current minimum of the objective function values of the sample points
α	no-linearity coefficient
δ	skin depth
κ	electrical conductivity
κ_{max}	maximum value of the electrical conductivity throughout the field domain Ω
μ	magnetic permeability; mean of a random process
ε	dielectric permittivity
ε_r	relative permittivity
ε_{max}	maximum value of dielectric permittivity throughout the field domain Ω
σ^2	variance of a random process
τ	time constant
τ_e	time constant of dielectric relaxation
τ_m	time constant of magnetic diffusion

$\boldsymbol{\theta}$ system parameter of Kriging models

φ scalar potential

$\boldsymbol{\Phi}$ vector of the nodal scalar potential

Index of Abbreviations

AC	Alternating Current
AiF	Arbeitsgemeinschaft industrieller Forschungsvereinigungen
ARC	Arcing
ATH	Aluminium Trihydrate
BEM	Boundary Element Method
CAD	Computer-Aided Design
ConCLL	Concentrated Conditional Log-Likelihood Function
ConLL	Concentrated Log-Likelihood Function
CL	Conditional Likelihood Function
CLL	Conditional Log-Likelihood Function
DC	Direct Current
DIRECT	DIViding RECTangles
DSB	Double Schottky Barrier
EVOP	Evolutionary Operation
FEM	Finite Element Method
EQS	Electro-Quasistatic
FIT	Finite Integration Technique
GFRP	Glass Fibre Reinforced Plastic
HTV	High Temperature Vulcanization
HV	High-Voltage
LHS	Latin Hypercubes Sampling

MEQSICO	Magneto-/Electro-Quasistatic-SImulation-COde
MLE	Maximum Likelihood Estimation
MSE	Mean Square Error
MQS	Magneto-Quasistatic
μVar	Microvaristor
PD	Partial Discharge
PDE	Partial Differential Equation
PEC	Perfect Electric Conductor
RMS	Root Mean Square
RMSE	Root Mean Square Error
SDIRK	Singly-Diagonal-Implicit-Runge-Kutta
SEM	Scanning Electron Microscope
SF$_6$	Sulfur Hexafluoride
SiC	Silicon Carbide
2D	Two Dimensional
3D	Three Dimensional
UV	Ultraviolet
VMQ	Vinyl-Methyl-Polysiloxan
Varistor	Variable Resistor
WEIF	Weighted Expected Improvement Function
ZnO	Zinc Oxide

1 Preface

1.1 Background

In high-voltage technology one of the most important tasks for designing a high-voltage device is to optimize electric field distributions in the device and around the surrounding environment. The reason for this is that high electric field strengths usually lead to some harmful phenomena, such as partial discharges along the surface of insulation materials, accelerated material ageing of polymeric materials and even worse, breakdown of the material and flashovers. To avoid such pitfalls, the optimization of the electric field distribution is desirable during the design of a high-voltage device. There are different techniques to reduce the electric field strength. The traditional field grading approaches, namely capacitive, refractive and geometrical field grading, usually require additional space and material leading to an over-dimensioned design and increased costs. An alternative approach is the use of non-linear field grading materials, which have an electric field strength dependent conductivity and change their electric state from insulating to conductive if the electric field strength exceeds a certain value. As a result, local high electric field strengths can be reduced.

This non-linear field grading approach has been used for decades for cable accessories and end corona protection of motor stator bars. For these applications fillers such as SiC (silicon carbide), carbon black and blends of different oxides are compounded into polymeric materials to be a functional polymeric composite. However, the non-linearity of these traditional field grading materials stems from particle-particle contacts and the material properties are therefore quite sensitive to the production process parameters and to a variety of external parameters such as humidity, contamination and pressure. Besides that, these materials have rather moderate electrical non-linearities and electric loadings [29]. Hence, the applications of these non-linear field grading materials are quite limited.

Another option to the traditional field grading materials is the use of microvaristor-based composite materials. Different from the traditional materials, the non-linearity is an intrinsic property of the interior of the microvaristor particle and the resistance of the particle-particle contact is low. As a result, microvaristor-filled materials are much more robust than the traditional field grading materials. As a spin-off product of ZnO (zinc oxide) ceramic varistor materials, microvaristor material is powder-shaped and has similar

fundamental properties. Mixed into an insulating or semiconducting material, microvaristor particles can transfer their non-linearity to composite materials, resulting in a high non-linearity of the final field grading composite material. Compared to the traditional field grading materials, which have a non-linear coefficient[1] between 3 to 8, microvaristor-filled composite materials have a much higher non-linear coefficient, typically varying from 20 to 30 [29]. With a higher non-linear coefficient the field grading effect can be improved [16]. Despite the fact that the non-linearity is an intrinsic property of the microvaristor particle, properties of the carrying matrix can also affect the properties of the final composite material consisting of microvaristor powder and the carrying matrix. Other than the high non-linearity, microvaristor-filled composite materials also have a comparable relative permittivity to refractive field grading materials.

Because of the above described advantages of microvaristor-filled materials, microvaristor-filled silicone composites have been successfully applied to cable terminations at medium voltages for several years [122]. However, the study of the application of microvaristor-filled materials in other high-voltage devices is still required. A grant research AiF-project [33] was carried out from 2008 to 2010 to research the possibilities of applying microvaristor-filled materials in high-voltage devices such as outdoor insulators [24][P2], cable accessories [126] and electrical machines [22][125]. In this thesis, the further application of the microvaristor-filled silicone rubber in outdoor insulators and the application of the microvaristor-filled epoxy resin in gas-insulated bushings is investigated.

1.2 Direction of Research and Objectives

The focus of the present research can mainly be divided into three parts. The first part is the application of microvaristor-filled silicone rubber to high-voltage outdoor polymeric insulators. Polymeric materials have been widely used for outdoor insulators since the 1970s. Compared to traditional ceramic insulators, composite polymeric insulators have many advantages such as light weight, easy transport and installation, low maintenance costs, hydrophobicity of the material surface and excellent electrical performance, especially under moderately to heavily polluted conditions. However, polymeric insulators suffer from a problem of material ageing. One of the primary factors causing the material degradation is high electric field strength. Thus, optimization of electric field distributions along the insulator surface is desirable for the polymeric insulator design. For this purpose, the microvaristor-filled silicone rubber, which is expected to reduce the peak of the electric field strength, is applied to outdoor insulators. In this thesis, the investigation of this application is carried out using FEM (Finite Element Method) simulations, which allow fast and

---

[1]The definition of the non-linear coefficient is given in chapter 2.

cost effective determination of electric field distributions with substantial accuracy. Different geometrical configurations for microvaristor materials are explored to get an optimized field grading effect. Furthermore, the electric field distributions along the surface of the insulators are calculated under different surface conditions, such as dry surface condition, a few water droplets on the surface and in the presence of dry bands. Additionally, the simulation results are also compared to experimental results, which are obtained in the high-voltage laboratory at the Technische Universität Darmstadt.

The second part of the thesis is the application of microvaristor-filled epoxy resin in high-voltage bushings. One common method to reduce the electric field strength in critical regions is to enlarge the diameter (geometrical field grading). Another method is the use of a shielding electrode (capacitive field grading). These two approaches lead to an over-dimensioned design and higher material costs. Compared to that the use of a microvaristor-filled epoxy resin layer allows for a compact design of bushings. By placing the microvaristor layer in the appropriate position and choosing a suitable switching point, the electric field strength in critical regions can be reduced. In this work, this idea is verified via FEM simulations and experiments in a high-voltage laboratory. FEM simulations are carried out to determine the suitable switching point and the position of the microvaristor layer. Furthermore, the influences of the length and the thickness of the microvaristor layer on electric field distributions along the surface of bushings are investigated. The prototypes, which are determined by FEM simulations, are built and tested in a high-voltage laboratory.

The third part of the research is about optimization algorithms using surrogate models. Some geometrical and material parameters can be optimized to get a better field grading effect. However, most of the high-voltage components considering high-voltage conductors and grounded parts are large-scale and non-rotationally symmetric. Hence, a 3D (three dimensional) FEM simulation with a fine mesh and higher order ansatz-functions is required to accurately calculate electric field distributions. However, a 3D accurate FEM simulation for a large-scale problem is usually quite time consuming. In this case, the number of 3D accurate FEM simulations should be limited, due to time constraints. To do this the Kriging method using one-then-two stage infill strategies is at first adjusted and tested to optimize the corona ring for outdoor insulators. However, the number of these simulations should be further limited with the increasing expense of a 3D simulation. For this purpose, the Co-Kriging method, which combines information of 3D simulations and cheaper lower quality simulations, such as reduced coarse 2D (two dimensional) simulations, is adopted for the optimization of the large-scale high-voltage devices.

In short, the specific objectives of the present research can be outlined as follows:

i) To investigate the potential use of non-linear microvaristor-filled silicone rubber in

outdoor insulators for controlling high electric field strength under different surface conditions.

ii) To verify the idea that the use of the microvaristor-filled epoxy resin in gas-insulated bushings allows for a compact design.

iii) To determine a suitable switching point and the geometrical parameters of the microvaristor layer.

iv) To choose and adjust suitable optimization algorithms, which allow for a faster, but still accurate optimization process.

v) To test these algorithms with analytical functions and use them for the corona ring design problem for outdoor insulators.

1.3 Organisation of this Thesis

This thesis is divided into eight chapters:

- **Chapter 1** gives an overview about this thesis, including the motivation, the direction and the organisation of the thesis.

- **Chapter 2** offers a review of the properties of microvaristor materials. The possible influences of external parameters on the microvaristor-filled composite materials used for this research are discussed.

- **Chapter 3** introduces the information about FEM simulations for high-voltages featuring non-linear field grading materials, including the electro-quasistatic approximation and the simulation process.

- **Chapter 4** presents the investigation of the possible use of the microvaristor-filled silicone rubber in high-voltage outdoor insulators. The different application possibilities of this material to insulators are compared and discussed.

- **Chapter 5** proposes the design of compact bushings using microvaristor-filled epoxy resin. The investigation using FEM simulations and measurements in a high-voltage laboratory is presented.

- **Chapter 6** proposes the optimization process using an adaptive Kriging method. Further, the algorithm is tested with analytical functions and the corona ring design problem for high-voltage insulators.

- **Chapter 7** presents the optimization of the corona ring design problem using the Co-Kriging method.

- **Chapter 8** gives general conclusions based on the findings of this research and outlines some recommendations for future investigation.

At the end of this thesis is a bibliography divided into three parts: a) the usual references; b) publications that were written while conducting research for this thesis are marked with a capital P when cited; c) the supervised master thesis during the research work is marked with a capital T when cited.

2 Properties of Microvaristors

2.1 Introduction

One of the most important properties of varistor (variable resistor) ceramics is its non-linear electrical characteristic. These materials change their electrical state from insulating to conductive in regions where the electric field strength exceeds a certain value. This value is usually called switching point. Additionally, varistors also have a high energy absorption ability. Functionally, varistors are analogous to two back-to-back Zener diodes, thus they are usually applied to limit transient over-voltage in both polarities from a few volts in electronics to 1000 kV in modern high-voltage systems [48]. Nowadays, varistors based on doped ZnO ceramics are widely used to protect against lightning impulse or electrical discharges [75].

As a spin-off from the metal-oxide varistor technology, microvaristors have been developed and used as a functional filler in an insulating or semiconducting matrix. In this case microvaristor particles can pass their electrical non-linearity directly to the composites [46], which lead to the versatility of mixing microvaristors with different matrices according to different applications. Despite microvaristors having the fundamental properties of varistors, the properties of the carrying matrix can also affect the final composite consisting of microvaristor powder and the insulating matrix. In this chapter, the fundamental properties of varistors and the characteristics of microvaristor-filled composite materials are introduced. Besides, the possible parameters which may have influence on electrical properties of microvaristor-filled materials are discussed.

2.2 Historical Background

The history of the original varistor ceramics can be traced back to the early 1930s. Bell System developed the materials consisting of sintered compacts of SiC particles to protect telephone systems [26]. In 1969 and 1971 Matsuoka published two papers [82][81] about the non-ohmic properties of ZnO based varistors, which captured public attention. During the two decades after the invention of the ZnO varistors, plenty of research was done, which provided the scientific basis for varistors as well as many of the key technological developments [18]. As a result, a number of products of ZnO varistors have been widely

used for protecting the devices from over-voltages. Recently, new non-linear field grading materials based on microvaristor fillers have become commercially available, which are superior over the traditional composites based on fillers such as SiC, carbon black or blends of different oxides [29]. Compared to those traditional varistor-type composites, ZnO microvaristors have a higher non-linearity coefficient. Besides, the non-linearity is an intrinsic bulk property of the ZnO particles resulting in an easier adjustability and lower sensitivity to percolation properties [16].

2.3 Fundamental Characteristics of Varistors

2.3.1 Electrical Properties

The most important property of the ZnO varistor is its non-linear current-voltage characteristic, as illustrated in Fig. (2.1).

Figure 2.1: Double logarithmic illustration with three different regions of a typical non-linear current-voltage characteristic of a varistor ceramic.
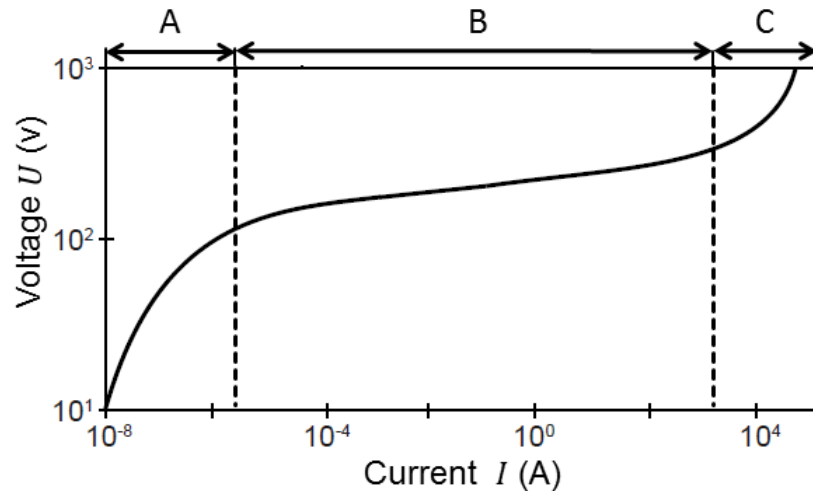
Mathematically the following equation can be used to describe the current-voltage characteristic of ZnO varistors:

$$I(U) = kU^\alpha. \tag{2.1}$$

Sometimes this characteristic is also defined in [31][76] as

$$I(U) = \left(\frac{U}{C}\right)^\alpha, \tag{2.2}$$

where k and C are scalar values which can be determined by measurements and α is the

non-linearity coefficient. The parameter α is generally defined in [18] as

$$\alpha = \frac{d\ln(I)}{d\ln(U)}. \tag{2.3}$$

or in [15] as

$$\alpha = \frac{d\ln(J)}{d\ln(E)} = 1 + \frac{d\ln(\kappa)}{d\ln(E)}, \tag{2.4}$$

where J is the magnitude of current density, E is the magnitude of electric field and κ is the electrical conductivity.

In Fig. (2.1) three regions can be distinguished in the current-voltage characteristic [48]:

A) Low-Current Linear Region: In the low-current region, which is also called pre-breakdown or pre-switch region or Ohmic region, the varistors show a nearly Ohmic and linear behavior. In this region, the AC (Alternating Current) leakage current is about 2 orders of magnitude higher than the DC (Direct Current) current, which is the result of the dielectric loss on application of an AC voltage [48]. The total AC current consists of a capacitive current and a resistive current. This small leakage current caused by thermally excited electrons increases with rising temperature according to the Arrhenius' equation

$$I \propto \exp\left(\frac{-E_a}{k_B T}\right), \tag{2.5}$$

where I is the leakage current, E_a is the activation energy, k_B is the Boltzmann constant and T is the absolute temperature in Kelvin. Hence in this region the current is strongly temperature dependent.

B) Non-Linear Breakdown Region: If the voltage exceeds a certain value, which is called the threshold or switching voltage, the ZnO varistor enters into the non-linear breakdown region in which the current increases rapidly for a small increase in voltage. The typical α value of ZnO varistors varies from 30 to 100, whereas an α value of conventional varistors such as SiC varistors does not exceed 10 [31]. In this region the charge carriers move through the barriers between the grains and the current is barely affected by the temperature.

C) High-Current Upturn Region: In this region, in which the current density is usually greater than 10^3 A/cm^2, the current-voltage characteristic is almost linear again, similar to that in the low-current region. This region is determined by the bulk of the doped ZnO grains.

Beside the non-linearity coefficient, an another important parameter for the current-voltage characteristic for both the varistors and microvaristors is the threshold or switching

voltage, sometimes also called switching point or switching electric field strength. However, there is not a common definition available yet. In [31] and [24] the switching voltage is defined as the point at which the current density 1 μA/cm^2 is achieved. In [93] the switching point is defined as the point with the current density 1 mA/cm^2. In [4] the switching point is given as the intersection point of the tangent of the steepest branch of the current-voltage characteristic using a double logarithmic plot with the voltage axis. In [5] a linear plot is used instead of a double logarithmic plot. In [91] the characteristic is plotted using semi-logarithms with the voltage on linear axis, as shown in Fig. (2.2). In this case, the two branches of the characteristic form nearly straight lines. Two tangents are drawn to these two branches and the intersection of these two tangents is defined as the switching electric field strength E_{var}. Meanwhile, it is also common to define the switching point as a certain switching electric field strength at which the resistivity begins to decrease greatly [30]. Most manufacturers define the switching voltage at the point where a certain current is achieved [35][92]. The manufacturer ABB Switzerland Ltd. defines the switching point of microvaristor powders as the electric field strength at which the current density reaches 0.13 mA/cm^2 [79].

Figure 2.2: Definition of switching electric field strength using the semi-logarithmic plot in [91].
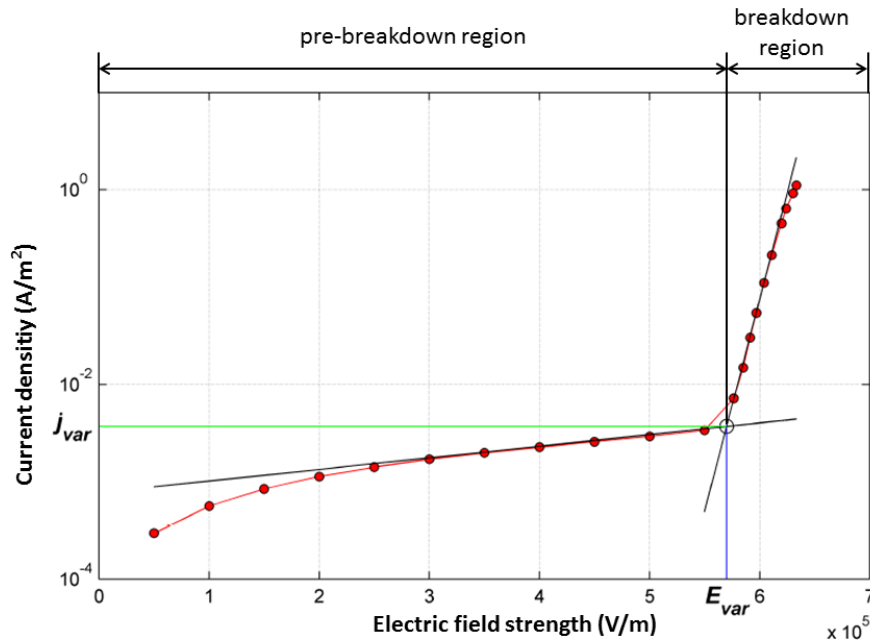
To characterize the current-voltage curve in the three regions of the ZnO varistors different measurement techniques are required. The $I - U$ characteristics below 100 mA/cm^2 can be measured using a DC or $50 \sim 60$ Hz AC electric source, whereas above 100 mA/cm^2 the characteristics are usually measured by an impulse current source, whose waveform has an 8-μs rise time and 20-μs decay time up to one-half of the peak value, to avoid heat

generation and thermal breakdown [31].

The electrical conductivity of ZnO varistors can be strongly affected by temperature. As described in Eqn. (2.5), in the pre-breakdown region the leakage current is small and temperature dependent. However, the temperature dependence decreases if the applied voltage increases. In the breakdown region the temperature dependence vanishes almost completely, as shown in Fig. (2.3). Beside the influence on the current, the high temperature also affects the degradation process of the varistor. Under extreme conditions, especially at elevated temperatures, the increase in leakage current leads to increased associated Joule heating and consequently may cause thermal runaway of the varistor [13]. However, the extend of degradation can be minimized and the degraded materials can be healed by an appropriate heat treatment [104].

Another important electrical property of ZnO varistors is the dielectric property, which is mainly caused by thin depletion layers at the grain boundaries. The relative permittivity ε_r of ZnO is 8.5, while that of a ZnO varistor is about 1000 [31].

Figure 2.3: Double logarithmic illustration of current-voltage characteristic for different temperatures [1].
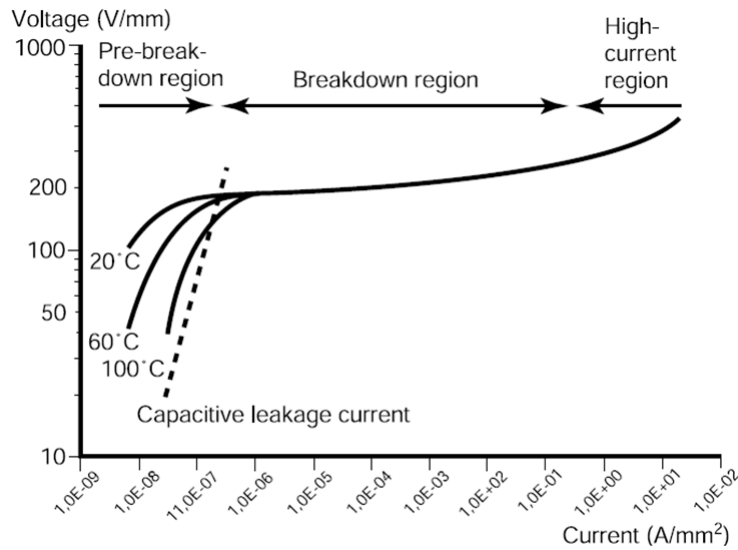
2.3.2 Chemical and Microstructural Properties

ZnO varistors are composed of ZnO and other metal oxides such as Bi_2O_3, Sb_2O_3, MnO_2, Co_3O_4, Cr_2O_3 and others as additives to get the desired characteristics of the varistors [84]. To achieve the non-linear property of the ZnO varistors Bi_2O_3 plays an essential role because it becomes a layer of inter-granular material and supplies ions to the ZnO grain boundaries, resulting in potential barriers at the grain boundaries. To dramatically

improve the non-linearity coefficient additional metal oxides are also required. The more detailed information about the chemical formulations and processes involved can be found in [81][89].

ZnO varistors are polycrystalline materials and consist of semiconducting ZnO matrix grains, the bismuth-rich phase, the spinels (nominally $Zn_7Sb_2O_{12}$), and sometimes also the pyrochlore phase (nominally $Zn_2Bi_3Sb_3O_{14}$). The microstructure is formed during sintering ZnO powder with small amounts of other metal oxides at a temperature in the range of 1100°C to 1300°C [84]. Although the microstructures of varistors vary from one manufacturer to another depending on different chemical formulations and processings, the typical microstructure can be demonstrated in Fig. (2.4). The white regions between the ZnO grains are bismuth-rich phases formed by solidification of the remnant liquid phase. The size of the ZnO grains, which determines the switching voltage of the current-voltage characteristics, is influenced by the usage of TiO_2 or BeO (to promote grain growth) and silicon dopant (to suppress grain growth), sintering temperature and time [18]. The larger the grains are, the smaller the number of grain boundaries become, which results in a lower switching voltage [29].

Figure 2.4: Microvaristor particle under the SEM (Scanning Electron Microscope) [121].
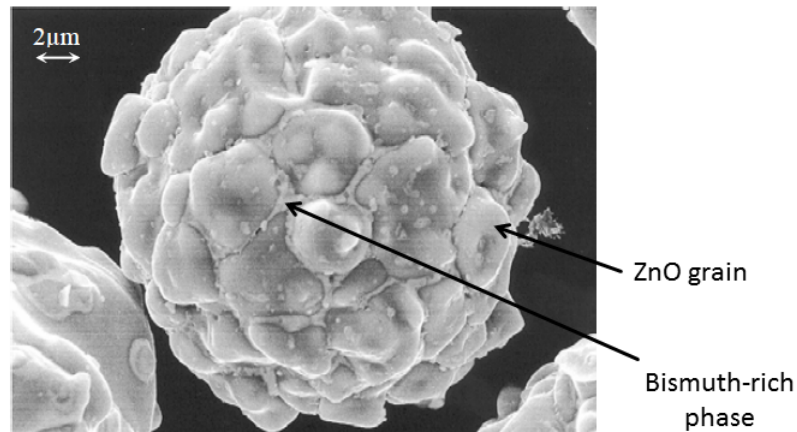
2.3.3 Physical Foundations

Compared to the conventional varistors such as SiC, whose electrical non-linear properties stem from the particle-particle contacts, the non-linearity is an intrinsic property of the ZnO varistors. The physical basis of the non-linear electrical property of the ZnO varistors is that the transport of the majority (electrons in the case of ZnO) crossing the charged grain boundaries is voltage dependent. The conducting mechanism in the ZnO varistors is

quite complicated and in the last four decades a large variety of models has been proposed to explain this mechanism. In [31] the different models were summarized based on the research conducted until 1989. The double Schottky barrier (DSB) model is considered to be the most adequate to describe the grain boundaries of the ZnO microstructure. In the pre-breakdown region the conducting mechanism is explained by means of energy barriers. At each boundary between ZnO grains, a potential barrier is formed by the capturing of electrons by acceptor impurities, resulting in a negative surface charge. The negative surface charge is compensated by positively charged donors in a space charge region, which is formed on each side of the grain boundary. The potential barriers are lowered if an electric field is applied, resulting in flow of a small current through the barriers. This current is temperature dependent because a high temperature increases the average energy of the electrons. In this case, the electrons can pass the barrier more easily. However, this model is limited to explain the phenomena such as the large non-linearities exhibited by varistors at small voltages (about 3.5 eV) per grain boundary or the switching voltage being above the band-gap of ZnO (3.3 eV) [18]. In [96] Pike showed that in the grain boundaries the minority carriers (in this case holes) are generated by "hot" electrons in the depletion layer at high electric fields. The minority carriers diffuse back to the grain boundaries because of the electrostatic field and compensate some of the trapped negative charge, resulting in lowering the potential barrier at the grain boundaries and consequently creating large non-linearity coefficients. More details describing the varistor behavior merging the minority carriers can be found in the research of Blatter and Greunter [7][45]. In the upturn region the voltage drop across the ZnO grains is dominating and the behavior can be controlled by means of doping the ZnO grains in order to adjust the grain resistivity.

2.4 Characteristics of Microvaristors

Microvaritors are powder-shaped ZnO varistors with the grain diameters in the range from 30 to 120 μm [44][46][122]. They are small sintered particles of doped ZnO with strongly non-linear electrical properties, which are similar to those of the varistor ceramics [28]. The main advantage of the powder form is that microvaristors can be mixed with a variety of materials to be the functional composites. As a functional filler in an insulating or semiconducting matrix the microvaritors can transfer their non-linearity and robustness directly to the composites. Although, the idea of imparting the properties of ZnO varistors to the composites can be traced back to the begin of the 1980s [49], the industrial feasibility was only achieved when spray drying of the granules was introduced [123].

Since the switching voltage is mainly determined by the size of the grains inside the particles, the size of the particles has a merely small influence on the switching voltage

and no influence on the non-linearity [29]. However, because microvaristors are usually used by mixing them into various insulating matrices, the properties of the matrix can also influence the electrical properties of the composites. In this section the electrical properties of the microvaristor-filled composites, using different insulating materials as the matrix, are introduced.

2.4.1 Microvaristor Powder

The microvaristor powders are produced by spray drying of the ZnO particles and several metal oxide dopants from a water-based slurry. Then the spray-dried granules are sintered at the temperature above 900°C. By tuning the parameters of the sintering process, the grain size is influenced, consequently the switching voltage. The larger the grains are, the smaller is the number of grain boundaries is, and as the result the switching voltage becomes lower. This allows to produce the microvaristors with the different switching voltages in a wide range for different applications. Depending on the processing route the powders may be slightly sintered together and a mechanical segregation may be required. Most microvaristor particles, produced by this process, are spherical, as shown in Fig. (2.5).

Figure 2.5: Microvaristor particles under the microscope (source: ABB Switzerland Ltd.).
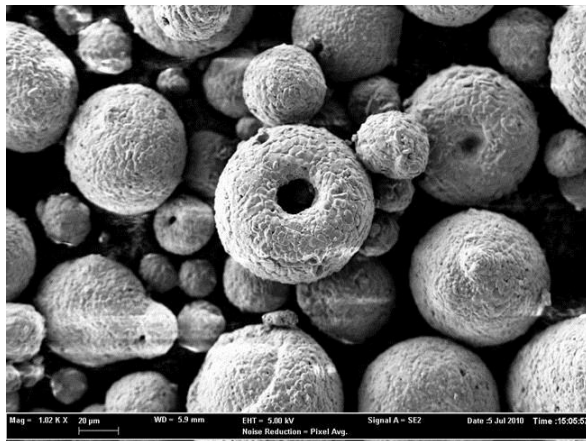
Unlike the traditional SiC varistors, whose non-linearity is based on the particle-particle contacts, the non-linearity of microvaristors is an intrinsic property of each particle and stems from the DSBs (double Schottky barriers), which are formed at the boundaries of the ZnO grains, as illustrated in Fig. (2.6). The non-linearity based on particle-particle contacts are hard to control since they are quite sensitive to some external parameters. Compared to that, the non-linearity of microvaristors stems from DSBs at each grain boundary inside the particles, which are at the origin of the highly non-linear current-voltage characteristics [45]. Hence, microvaristor-based materials are much more robust than the materials based on particle-particle contacts.

Figure 2.6: Schematic illustration of the microstructural possible current path inside field grading materials based on SiC (left) and microvaristors (right). Red: particle-particle contact; Orange: grain boundaries between the ZnO grains [28].
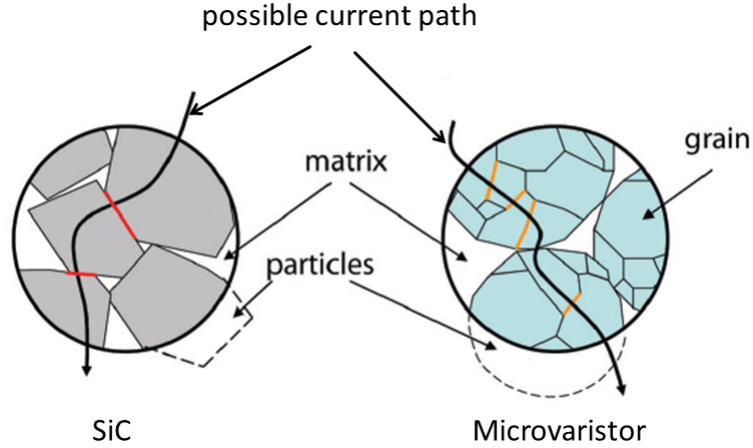
Each microvaristor particle, which includes a few grain boundaries, has itself a non-linear current-voltage characteristic. Each grain boundary along the current path contributes about 3.2 to 3.4 V to the switching voltage [45]. A typical current-voltage characteristic measured on a single microvaristor is shown in Fig. (2.7). This particle is measured by micro-contacting at diagonally opposite positions and has 4 active grain boundaries in this orientation. In [46] Greuter et al. also mention that the different switching voltages U_b are measured by contacting the same microvaristor particle randomly in different orientations. However, U_b is only less than or equal to 3 times of $\sim$ 3.2 V. Besides, Greuter et al. attempt to characterize the contact between two microvaristors A und B in air, which are measured individually and being connected in series. The measured switching voltages are $U_b(\text{A}) \sim 13$ V, $U_b(\text{B}) \sim 17$ V and $U_b(\text{A+B}) \sim 35$ V. These results indicate that a voltage drop of $\triangle U_G \sim 5$ V may exist. Greuter et al. explain this phenomena as the results of possible surface band bending and adsorbed layers, resulting in small extra barriers, which may contribute to the overall current-voltage characteristics, especially for low field composites.

To characterize the microvaristor powder a device is required that allows a dependable contacting of the powder in a defined way [90]. In [90] an arrangement with guard ring electrode and tempered electrodes, as demonstrated in Fig. (2.8), is adopted for the investigation of powder. The adopted electrodes are made from solid aluminium and are mounted on insulating plates, in which fluid ducts are integrated. This allows regulation of the temperature of the electrodes using a recirculating cooling/heating device. In [33] the use of a low viscous silicone oil is recommended to investigate the characteristics of microvaristor powder. The temperature dependent electrical characteristic of the powder is investigated

Figure 2.7: DC characteristics for a single microvaristor particle with the diameter 145 μm. The particle is measured by micro-contacting at diagonally opposite positions [46].
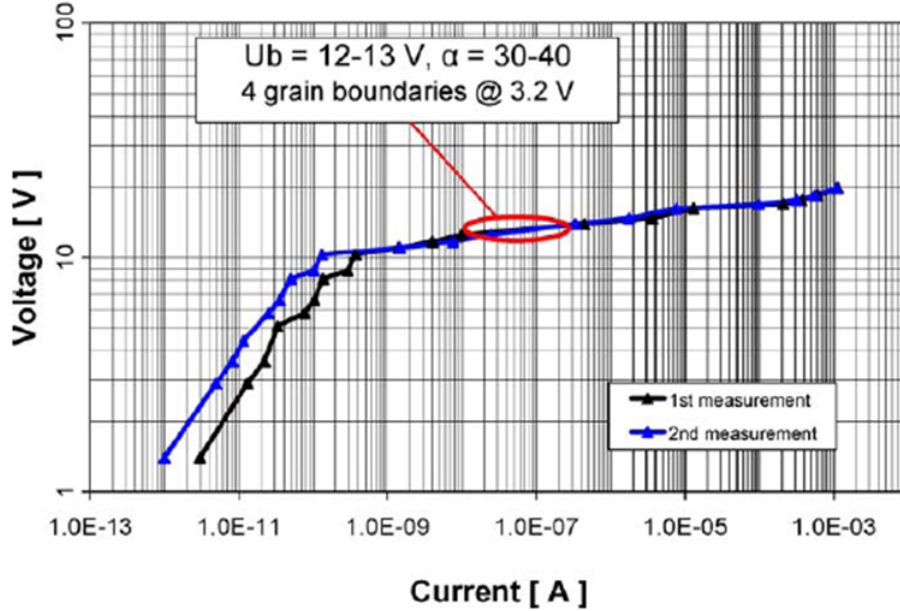
in [90]. The measurement results indicate that the leakage current in the pre-breakdown region increases approximately by one decade from 20°C to 80°C, which is also known to hold for solid varistors. However, in the breakdown region the behaviors of the microvaristor powder are quite different from the solid ZnO varistors as temperature increases. The characteristic of solid ZnO varistors is almost independent of the temperature, whilst the switching electric field strength of microvaristor powders decreases by approximated 15% with rising temperature from 20°C to 80°C. The influence of the other external parameters such as powder packing, materials of the electrode for the measurement and humidity can be found in [91].

2.4.2 Microvaristor-Filled Silicone Rubber

Microvaristor powder can be mixed into a silicone matrix to be a functional material. Today, microvaristors are typically applied in silicone rubber for field grading applications, i.e., stress cones for cable terminations [9][44][126] and the field control layer for outdoor long rod insulators [107][108]. The filler content of the microvaristor powder is typically at 40 volume percent. Depending on the filler content of the microvaristor compound the high permittivity of the microvaristors ($\varepsilon_r \approx 100\dots500$) can be transferred to the compound. Above the percolation threshold, which is almost 40 volume percent, the compound has a resulting relative permittivity of $\varepsilon_r \approx 12\dots16$. Fig. (2.9) presents the non-linear $E - J$ characteristics of two different microvaristor-filled silicone rubbers. In the silicone matrix

Figure 2.8: Schematic view of the measuring arrangement for the investigation of microvaristor powder [90].
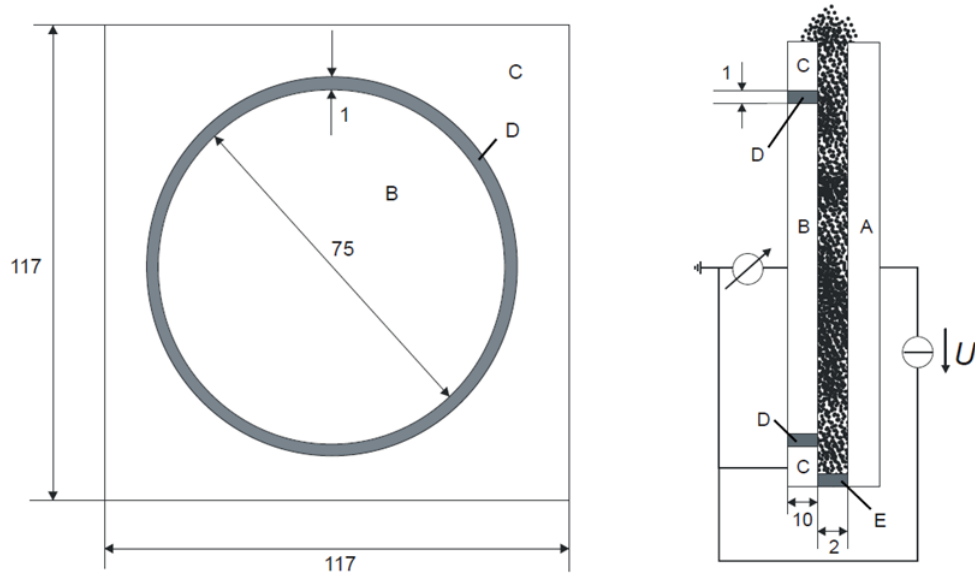
A: high-voltage electrode;   B: measuring electrode;   C: guard ring
D: polytetrafluoroethylene ring;   E: Spacer

the microvaristor particles are coupled to each other by the direct contact and/or capacitive effect. This explains why the $E - J$ curves measured under AC and DC are different.

To characterize the $U - I$ or $E - J$ curve of microvaristor-filled silicone rubber, plan-parallel electrodes are suggested to measure the disc-shaped samples. This use of the measuring arrangement achieves a homogeneous electric field strength in the measured samples. To avoid field disturbances and surface current effects, a guard ring is adopted as described in the standard DIN IEC 60093 [60]. The measurement arrangement is shown in Fig. (2.10). The DC characteristic is easier to measure. For the AC measurement a voltage source generating a sinusoidal voltage without harmonics is required to separate the total AC current into a capacitive and a resistive component [23]. As shown in Fig. (2.9), in the pre-breakdown region the capacitive current is much more dominant than the resistive current, while in the breakdown region the resistive current increases rapidly and is dominant in the total current. Further, the resistive current in the pre-breakdown region under AC voltage is greater than the current under DC voltage. However, in the breakdown region, the compounds tend to be slightly more conductive under DC than under AC conditions [23][29].

The current-voltage characteristic of microvaristor-filled silicone rubber compounds can be affected by some external parameters. In [29] the influence of temperature is investigated and the corresponding results are illustrated in Fig. (2.11). In the pre-breakdown

Figure 2.9: Non-linear AC and DC characteristics of the two different microvaristor-filled silicone rubbers. Blue: compound of the microvaristor powder with the switching electric field strength at 500 V/mm; Red: compound of the microvaristor powder with the switching electric field strength at 1000 V/mm. Here the switching point is defined at the point, at which the current density reaches 1 μA/cm² under DC [23].
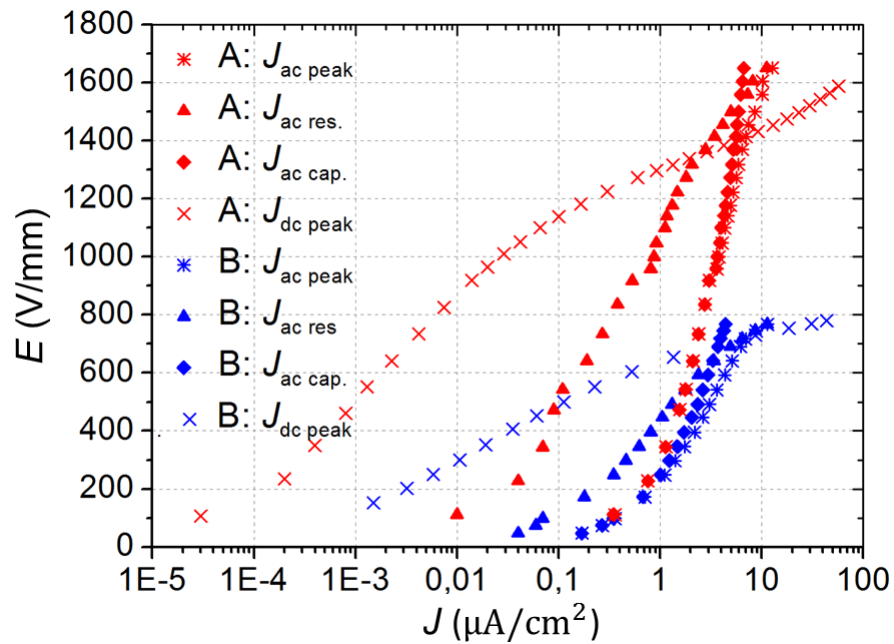
Figure 2.10: Sketch of measurement arrangement for disc-shaped samples [60].

(1) measuring electrode   (2) guard ring

(3) high-voltage electrode
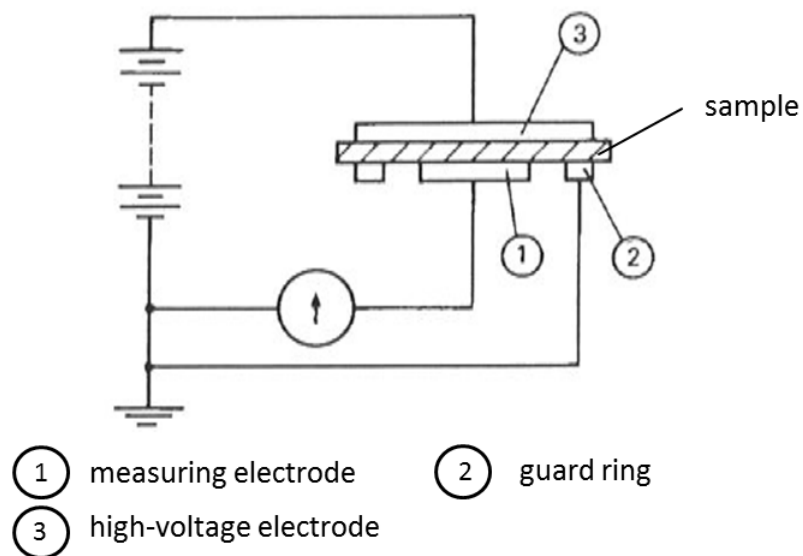
region, from room temperature to 70°C, the resistivity decreases with increasing temperature, which is similar to ZnO varistors. At 90°C the resistivity is again similar to the value at room temperature. A possible explanation of this phenomenon is that from room temperature to 70°C the effect of thermally activated transport of charges is dominant, whilst above 70°C the effect of thermal expansion of the silicone matrix is dominant, resulting in less conductive paths through the composites and consequently a slight increase of the switching electric field strength. In the mid field region the temperature-independent resistivity can be explained by the combined effect of thermally activated transport and thermal expansion of the silicone matrix. Similar results about the temperature influence on the microvaristor-filled silicone compounds are also observed in [33].

Figure 2.11: Temperature influence on the resistivity of the microvaristor-silicone compound: room temperature (circles), 70°C (triangles), and 90°C (squares) [29].
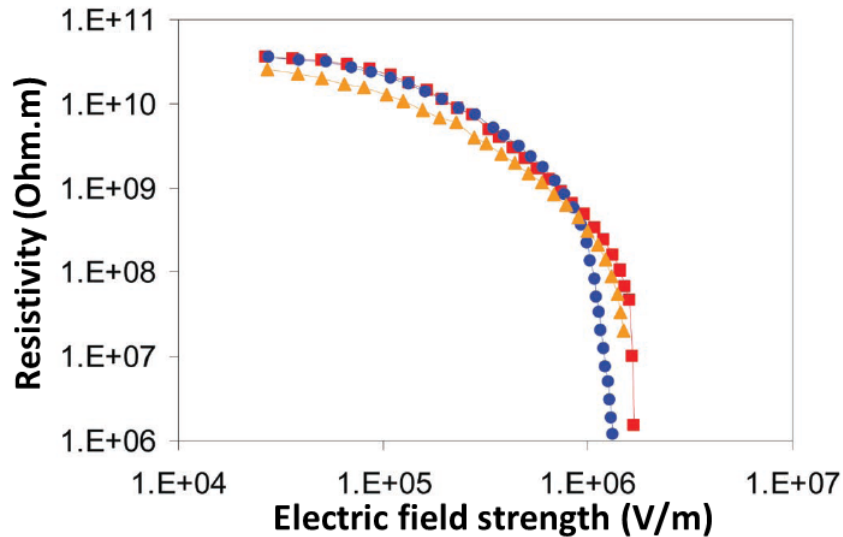
Another important external parameter, which could affect the electrical behaviors of the microvaristor-filled silicone rubber, is the mechanical stretching. This holds especially for the application of these materials for cable accessories. Under mechanical stress the compound is slightly less conductive in the pre-breakdown and the breakdown regions, whereas in the high-current region the difference is almost negligible [29]. These results show an advantage compared to the conventional field grading materials such as SiC and carbon-black, whose electrical characteristics are significantly affected by mechanical stretching effects.

Further, the treatment of the surface of microvaristor particles with a reactive silane has an influence on the electrical properties of the microvaristor-filled silicon rubber. Without the silanization microvaritor particles would fall out from the surrounding VMQ (Vinyl-Methyl-Polysiloxan) matrix under a mechanical stress/stretch test, since they do not have

adhesion and chemical connection to the VMQ matrix. This problem can be solved by silanization of microvaristor particles before the compounding with silicone rubber. The adhesions of the unsilanized and silanized microvaristor particles to the VMQ matrix are shown in Fig. (2.12). The silanised microvaristor-filled silicone compound shows a better conductivity than the unsilanised one [107].

Figure 2.12: The adhesions of the microvaristor particles to the VMQ matrix without (left) and with (right) silanization [107].

unsilanized microvaristor particles   silanized microvaristor particle
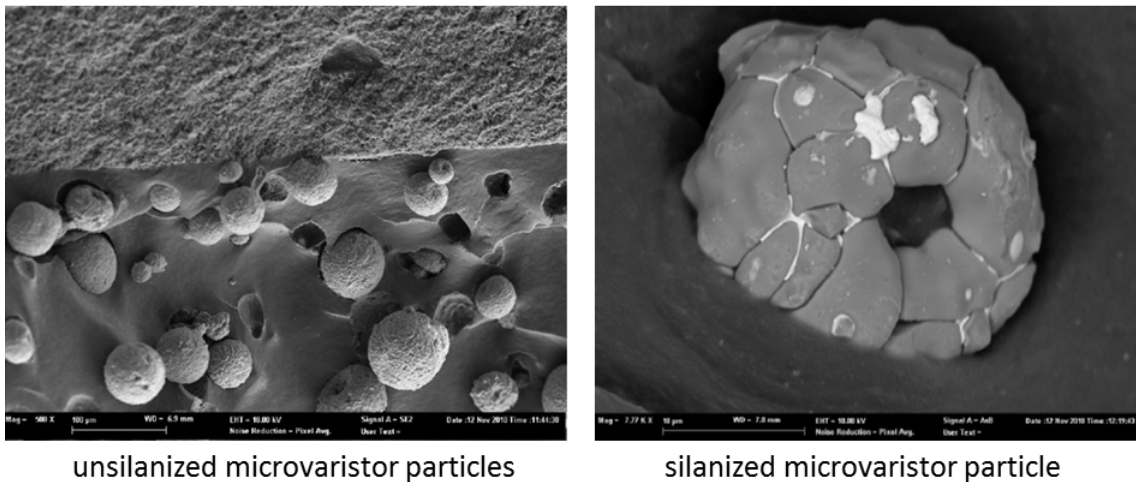
2.4.3 Microvaristor-Filled Epoxy Resin

For some applications microvaristor powders are mixed into the epoxy resin. Since the nature of the matrix can influence the electrical properties of the composites, differences of the electrical properties exist for different composites based on the same filler but different matrices. This can be seen in Fig. (2.13). The explanation of differences may be the degree of mechanical stresses, which is high in epoxy resin (shrinkage during cross-linking) but vanishes in the silicone oil. In this case, the packing and the contact properties of the microvaristor particles are different [29].

Up to today, there are already a few research results about the characterisation of microvaristor-filled silicon rubber composites and corresponding applications of these compounds [5][24][30][44]. However, the amount of literature about the microvaristor-filled epoxy resin is quite limited till now. The investigation of the electrical properties of microvaristor-filled epoxy resins with different microvaristor contents and at different temperatures will be described in the chapter 5.

Figure 2.13: Effect of the matrix on the resistivity of ZnO microvaristor composites: epoxy (circles) and silicone oil (triangles) [29].
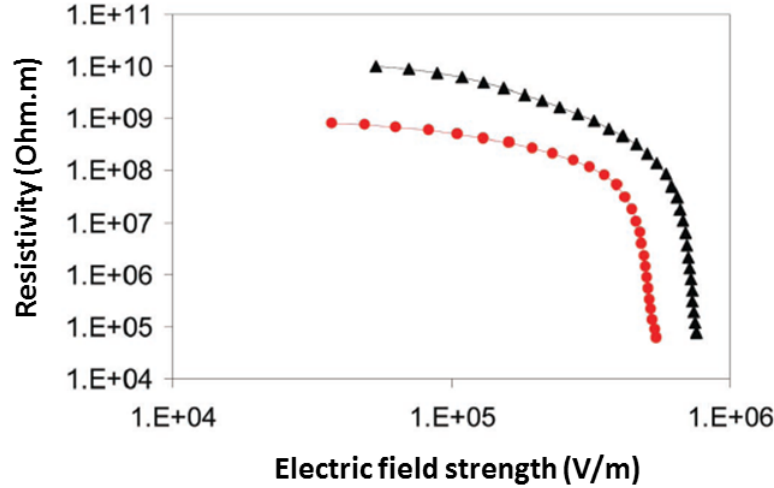
2.5 Summary

As a spin-off product of the traditional metal-oxide varistors, the powder-shaped microvaristors have similar electrical properties as the block-shaped metal-oxide varistors. For practical applications, microvaristor powders should be mixed into a carrier-matrix, such as silicone rubber, epoxy resin, silicone oil, etc., with a certain content above the percolation threshold, to be functional composite materials. Despite the fact that non-linearity of the microvaristors originates from the double Schottky contacts, which are located at the ZnO-grains boundaries, the nature of the carrier-matrices also has an influence on the electrical properties of the microvaristor-filled compounds. This is the reason why compounds with the same filler but different carrier-matrices show different electrical properties and are variously affected by the external parameters such as temperature and mechanical stress.

It should be noted that the switching points are differently defined by manufacturers and scientists. The microvaristor manufacturers provide just the technical data sheet of microvaristor powder. For the different applications, microvaristor powders are compounding into various matrices, resulting in the varying electrical properties as the original powders. Hence, investigations of the electrical properties of the different microvaristor-filled composite materials are necessary for practical applications.

3 FEM Simulations for Non-Linear Microvaristor-Filled Materials

3.1 Introduction

To computationally investigate possible applications of the microvaristor-filled compounds in high-voltage devices, numerical simulations are carried out under problem related approximations to Maxwell's equations. A finite-element-formulation based on the electro-quasistatic (EQS) approximation is adopted to simulate electric field distributions in the computational domain on unstructured meshes [118]. This formulation considers both capacitive effects and non-linear conductive effects in the insulation materials. Based on the continuity equation, the partial differential equations describing EQS potential problems yield non-linear transient systems of ordinary differential equations. Due to the non-linear switching characteristics of the microvaristor-filled compounds, these systems of equations are solved with time domain methods [19][32]. To solve this problem in time domain, a Singly-Diagonal-Implicit-Runge-Kutta methods (SDIRK3(2)) is adopted [120].

In this chapter, the different methods to validate the applicability of EQS approximation are introduced. Besides, the simulation process including pre-processing, FEM-calculation and post-processing is summarized.

3.2 Electro-Quasistatic Approximation

3.2.1 Applicability of Electro-Quasistatic Approximation

In order to efficiently analyse electromagnetic properties of high-voltage devices, numerical simulations can be run under problem related simplifications to Maxwell's equations. For many technical problems solutions of the full set of Maxwell's equations, which consider the coupling effects of electric and magnetic field, are not necessary. Beside that, most numerical formulations for solving the full set of Maxwell's equations become unstable if the frequency of the excitation tends to zero [58]. Hence, suitable approximations can be selected to solve for the electromagnetic fields related to different problems.

In the case of low frequency, respectively slowly time-varying fields, the electromagnetic wave propagation can be neglected, if the calculation domain is much smaller than the

distance an electromagnetic wave covers during the characteristic time of the device [120]. The characteristic time is estimated as the reciprocal of the highest frequency at which the device is operated [27]. In this case, the slowly varying fields can be approximated in the majority of cases by an electro-quasistatic field or a magneto-quasistatic field [119]. The electro-quasistatic (EQS) approximation, considering both capacitive and resistive effects whereas neglecting inductive effects, is usually applied to electric field problems in high-voltage technology [100][118], microelectronics [27], biological systems engineering and medical engineering [101]. On the contrary, the magneto-quasistatic (MQS) approximation is often applied to problems for which inductive and resistive effects need to be considered and capacitive effects can be neglected.

The next three different methods, which are introduced in the different references [27][54][119], can be adopted to classify EQS and MQS fields: 1) based on energy densities; 2) based on the time constant; 3) based on material parameters and frequency. Details about these three methods can be found in appendix A.

3.2.2 EQS Formulation for Non-Linear Materials

Under the electro-quasistatic approximation, the following Maxwell's equations in time domain can be obtained by neglecting the induced current density and the impressed current density of the given source:

$$\text{curl}\vec{H} = \kappa\vec{E} + \frac{\partial}{\partial t}(\varepsilon\vec{E}), \tag{3.1}$$

$$\text{curl}\vec{E} = 0, \tag{3.2}$$

where $\vec{H}$ is the magnetic field, $\vec{E}$ is the electric field, κ is electric conductivity and ε is the dielectric permittivity. If the premises of Poincare's lemma are satisfied, which can usually be assumed, then the following is valid:

$$\text{curl}\vec{E} = 0 \Leftrightarrow \vec{E} = -\text{grad}\varphi, \tag{3.3}$$

where φ is the scalar potential. Based on the Eqn. (3.1) the corresponding continuity equation is given by

$$\text{div}(\kappa\vec{E}) + \frac{\partial}{\partial t}\text{div}(\varepsilon\vec{E}) = 0. \tag{3.4}$$

By inserting the Eqn. (3.3) into Eqn. (3.4), the following equation can be obtained:

$$\text{div}(\kappa\text{grad}\varphi) + \frac{\partial}{\partial t}\text{div}(\varepsilon\text{grad}\varphi) = 0. \tag{3.5}$$

For the in this work investigated high-voltage devices featuring non-linear microvaristor-

filled composites the permittivity ε for each materials can be considered as a constant, while the conductivity of the microvaristor component is electric field dependent, that is $\kappa = \kappa(|\vec{E}|)$. Then Eqn. (3.5) can be further modified into:

$$\mathrm{div}\left(\kappa(\mathrm{grad}\varphi)\mathrm{grad}\varphi\right) + \frac{\partial}{\partial t}\mathrm{div}(\varepsilon\mathrm{grad}\varphi) = 0. \tag{3.6}$$

This non-linear partial differential equation (PDE) can be solved using diverse numerical techniques in space, i.e., the finite element method (FEM) [111], the finite integration technique (FIT) [131] and the coupled FEM-BEM method [116]. In this work the finite element method is adopted to simulate the high-voltage devices with microvaristor components. For this, Eqn. (3.6) is discretized in space using a FEM formulation, resulting in the matrix equation

$$\mathbf{K}_k\left(\mathbf{\Phi}\right)\mathbf{\Phi} + \mathbf{B}_\varepsilon\frac{\mathrm{d}}{\mathrm{d}t}\mathbf{\Phi} = 0, \tag{3.7}$$

where $\mathbf{\Phi}$ is the vector of the nodal scalar potential and $\mathbf{K}_k(\mathbf{\Phi})$ and $\mathbf{B}_\varepsilon$ represent stiffness matrices of the non-linear electrical conductivity and the linear permittivity, respectively. The Eqn. (3.7) represents a matrix system of stiff ordinary differential equations in time domain. This can be further solved by time integration using an implicit Euler method [14] or a stiffly accurate embedded Singly-Diagonal-Implicit-Runge-Kutta method (SDIRK3(2)), which is a one-step method with $s = 4$ internal stages [21][73][120].

3.3 Simulation Process

To simulate high-voltage devices with non-linear microvaristor components, the entire process can be divided into four parts:

1) Creation of CAD models.

2) Generation of unstructured meshes.

3) Computational calculation of the suitable PDE using the FEM method and an appropriate time integrator.

4) Evaluation of the simulation results.

The schematic view of the simulation process is illustrated in Fig. (3.1).

3.3.1 Creation of CAD Models

The simulated models of investigated high-voltage devices can be created using computer-aided design (CAD) software. It should be noted that CAD models for computational simulations are usually distinguished from CAD models for manufacturing. The CAD models

Figure 3.1: Schematic view of the simulation process
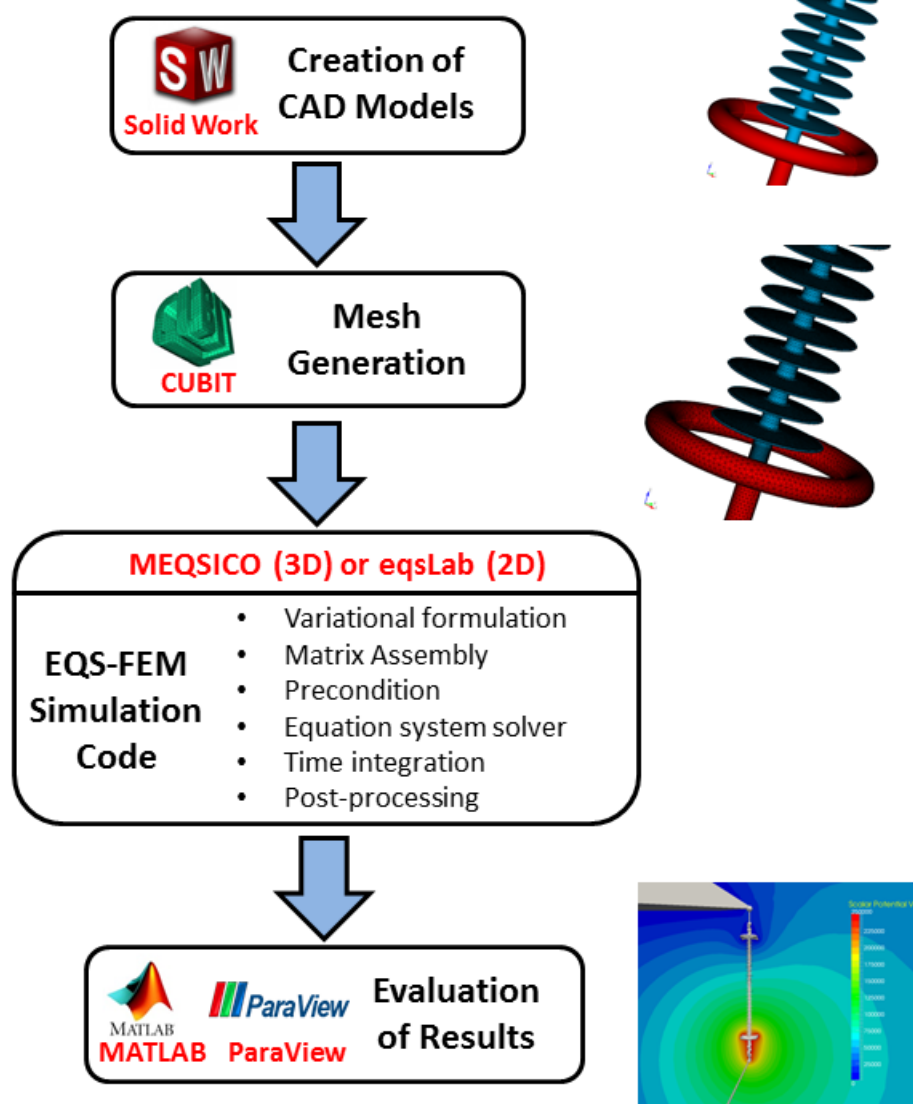
required for simulations should be more accurate (small tolerance) and should not contain overlapping geometries.

To simulate infinitely extended air ambience, the boundary element method (BEM) can be adopted to couple with the FEM [117]. However, because the in this work investigated high-voltage devices are experimentally investigated in high-voltage laboratories which are enclosed rooms with grounded walls, the air ambient region can be modelled as a finite volume. The size of the air-volume should be big enough, otherwise the electric field strength could be overestimated to a much higher value than the real value. The bottom surface of this air-volume (ground) is set to Dirichlet boundary condition of 0 V. The surfaces of the air-volume, which cut the transmission lines off, are typically set to homogeneous Neumann boundary conditions, since that is the simplest choice of the boundary conditions that are consistent with the physical existing tangential field along the cables.

3.3.2 Generation of Unstructured Meshes

In this work the software called CUBIT is adopted to discretise the CAD models into tetrahedrons. CUBIT, which is developed by Sandia National Laboratories, is a software toolkit for robust generation of two- and three-dimensional finite element grids. It also provides mesh generation for second order triangular and tetrahedral elements, allowing more exact approximation of curved geometries [129].

3.3.3 Computational Calculation using the FEM Method

The three dimensional simulation code MEQSICO (Magneto-/Electro-Quasistatic-SImulation-COde) [20][118] and the two dimensional simulation code eqsLab2D, which are developed using C++ and Matlab by the Chair of Electromagnetic Theory at the Bergische Universität Wuppertal, are adopted to simulate the electric field problems under the EQS assumption. Before starting the computational calculation, the following steps should be done first:

a) Verification of the applicability of the EQS assumption.

b) Definition of the materials parameters.

c) Definition of the boundary conditions.

Then the simulation code MEQSICO and eqsLab2D based on FEM can calculate the potential and electric field distribution of the simulated models. The whole process of the calculation can be divided into the following parts:

- Translation of the boundary value problems into the variational formulation for partial differential equations.

- Import the mesh file, which is generated by the mesh-generation software.

- Choosing an initial approximation guess solution in terms of nodal values of the elements and interpolation functions.

- Deriving element stiffness matrices with the help of a Gauß-Jacobi-Quadrature.

- Assembly of overall equations/matrices.

- Linearisation of the algebraic equation system.

- Solving the system of algebraic equation.

- Converting the electric potential solution to the electric field solution.

- Time integration.

3.3.4 Evaluation of the Simulation Results

In this work ParaView and Matlab are used for the visualization of the simulation results. ParaView is an open-source software and is able to visualise and analyse simulation results using qualitative and quantitative techniques, such as slice plot, contour plot and plot over a line. Matlab is used to plot the potential and electric field distribution along evaluation lines, which are given by coordination of evaluation points within the calculation domain.

3.4 Summary

In this chapter three different methods are presented to classify problem related simplifications of Maxwell's equations. For high-voltage devices with non-linear microvaristor-filled materials, the EQS assumption is adopted to simplify the continuity equation. In this work investigated devices are operated under 50 Hz and thus the propagation of an electromagnetic wave can be neglected. Further, these non-linear materials have a moderate conductivity. Hence, the EQS assumption is applicable to the problems at hand.

Under the EQS assumption, the continuity equation can be simplified yielding non-linear transient systems of ordinary differential equations. The simulation process is also presented and mainly divided into four parts, as illustrated in Fig. (3.1).

4 Investigation of Insulators with Microvaristor-Filled Silicone Rubber Components

4.1 Introduction

In 1963 composite polymeric insulators were first developed and are now widely used in power systems because they have significant advantages compared to ceramic and glass insulators: light weight, a higher mechanical strength, ease of transportation and installation, lower maintenance cost, better performance in outdoor service in the presence of heavy pollution, hydrophobic properties and comparable or better withstand voltage [51]. However, composite insulators may be subjected to accelerated ageing caused by tracking and erosion effects [109]. Tracking is the production of a resistive path by degradation of the polymer usually because of deposition of carbon. Erosion is the loss of surface material which arises mainly from electrical discharges or from electrochemical reactions in the layer of a contaminant [78]. If tracking and erosion occurred, the final failure can appear by water induced stress corrosion, cracking the glass fibre core, as shown in Fig. (4.1). One of the most important factors leading to discharge and consequently degradation of the material is a high electric field strength along the surface. Hence, minimizing the maximum of the electric field strength along the insulator surface under wet and polluted surface conditions is desirable for insulator designs.

In [34] positive effects of a semiconducting glaze on porcelain insulators are reported. Using this glaze with a low conductivity affects the electric field distribution along the insulator under rain and polluted conditions and allows the "dry band arcing" performance to be improved. However, it is difficult to produce reproducible electrical properties. Thus using microvaristor-filled silicone rubber is an alternative option to control the electric field distribution on the insulator surface.

In this chapter tangential electric field distributions of applying the microvaristor-filled silicone directly on the surface of insulators with different geometrical configurations are compared using different models of wet polluted surfaces. Additionally, the application of the microvaristor-filled silicone layer under a protection silicone layer is investigated. Tangential electric field distributions along the surface of insulators are evaluated under

Figure 4.1: Final failure of polymeric insulators by water induced stress corrosion (Source: Lapp Insulators GmbH).

the dry surface condition, with water droplets on the surface and on the presences of wet polluted conductive surfaces.

4.2 The Role of the Electric Field Strength for Electrical Discharges

The electric field distribution along the insulator surface plays a key role for the insulator design. The principal task of designing insulators is to ensure that the electric field strength along the insulator surface does not exceed critical values [95] which could lead to electrical discharges in the form of corona discharges, dry band arcing and even worse flashovers [106], which will be shortly discussed next.

4.2.1 Metal Electrode Initiated Corona

The electric field distribution along the polymeric insulator is usually non-uniform and the highest value is normally at regions near the energized and grounded end fittings under dry conditions [53][112]. If the local electric field strength reaches the air ionisation threshold, a corona occurs. The corona discharge starts from the metal fittings on locations with the greatest electric field strength, which is usually the so called triple junction point of the metal fitting, the air and the polymeric material. Through secondary reactions ozone and nitrogen oxides are generated, which, when dissolved in moisture, can lead to the formation of acidic water on the polymeric surface [86]. In this case, the insulation surface

is attacked by the acidic water by destroying cross-links in the polymeric compound, leading to degradation of the material. In extreme cases this results in a cracking of the polymeric sheds.

4.2.2 Water Droplet Initiated Corona

It is well known that water droplet coronas have been shown to generate audible noise, radio noise and television interference in wet weather [43]. Beside that, water droplet corona discharge is also a major cause of degradation of the silicon rubber material of composite insulators [11][94]. Due to the high relative permittivity of water droplets, the electric field strength is amplified nearby. This effect is shown at the triple point, which is the junction point of water, air and polymeric material, if water droplets are stressed under the tangential electric field strength, as shown in Fig. (4.2), and at the tip of the water droplets if they are stressed under the normal electric field strength, as illustrated in Fig. (4.3). These locations are also the locations for discharge activity reported in [87] and [12]. Under the electric field strength, the water droplets vibrate (under AC) and elongate in the direction of the electric field. This distortion shortens the insulating distance, enhances the electric field strength and consequently results in corona discharges on the surface if the electric field strength exceeds the corona inception onset. The water droplet corona inception onset depends not only on the orientation of the electric field strength in terms of tangential and normal components, but also on parameters such as droplet size and shape, surface materials and atmospheric conditions [47][94][124]. If intense and continuous discharge activities occur, the polymeric surface will lose its hydrophobicity[1], consequently leading to an increase in surface wettability, hence forming water films on hydrophilic regions. More details about investigations of water droplet initiated corona discharges can be found in [56] and [36].

4.2.3 Dry Band Arcing

As described in the last subsection, polymeric materials will lose their hydrophobicity under intense and continuous corona discharges. This loss of hydrophobicity leads to the spreading of water on the surface and the formation of dry bands [37]. Besides that, outdoor insulators are usually contaminated by natural pollution (e.g. sea salt and sand), industrial pollution (e.g. industrial dust), acid rain and gas, especially by sulphuric oxide (SO_x) and nitric oxide (NO_x). In heavy polluted regions, the surface conductivity on outdoor insulators can exceed the value of 100 µS, which leads to arcing development and eventually to a flashover at a continuous operation voltage [17]. If the humidity has the opportunity

---

[1]Hydrophobicity is the ability of a surface to repel water droplets on the surface. On a hydrophobic surface no water film will be formed.

Figure 4.2: Equipotential contour lines of potential distributions for a static water droplet under the tangential electric field strength.
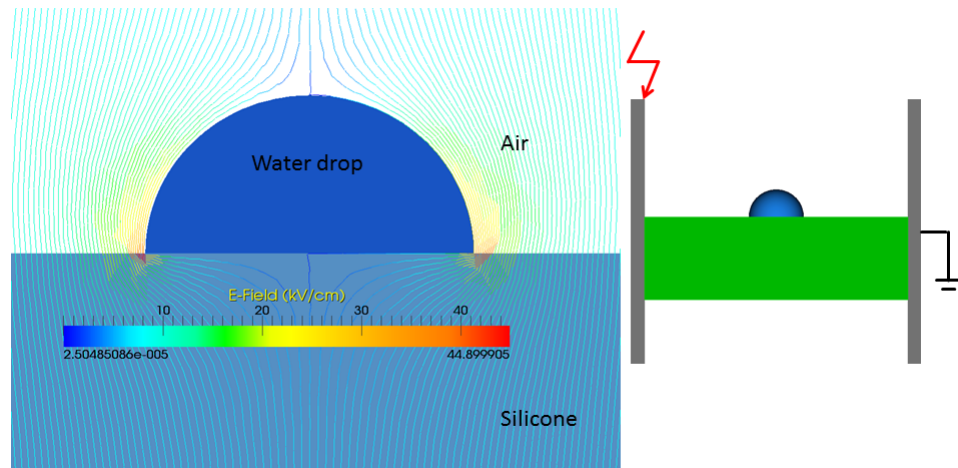
Figure 4.3: Equipotential contour lines of potential distributions for a static water droplet under the normal electric field strength.
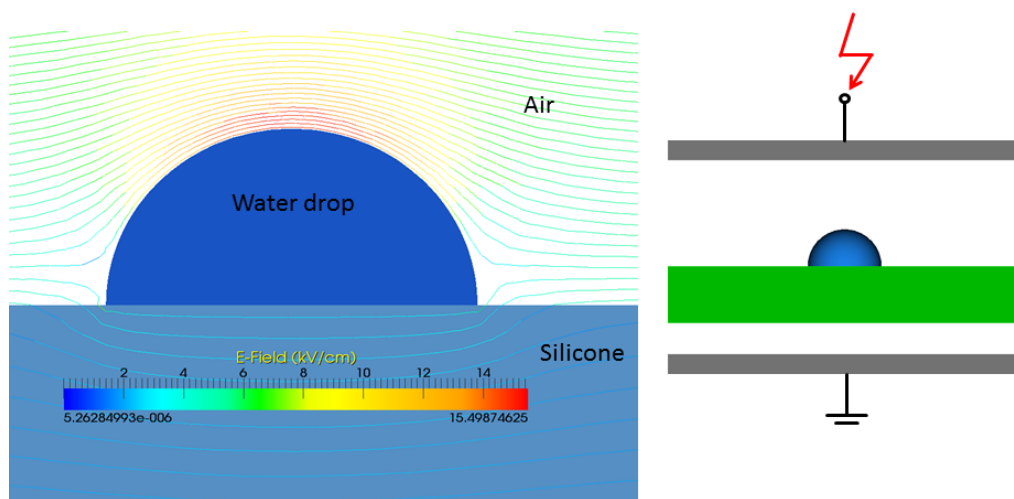
to wet the polymeric surface containing the contamination layer, continuous conductive films are formed on the polymeric surface, which causes a leakage current flowing along the creepage distance, resulting in Joule heating. This heating effect evaporates the water from the conductive layer and dries out the wet polymeric surface. However, this process is not uniform along the conductive path, leading to different drying rates of humidity. The possibility of the formation of dry bands is high in regions of highest current density values and dissipated power [52]. If a dry band appears, the flow of the leakage current is limited and charges are gathering at the interface between the conductive film and the dry band, resulting in a high electric field strength and consequently intense electric discharges that bridge the dry region, as illustrated in Fig. (4.4).

Figure 4.4: Schematic illustration of dry band arcing
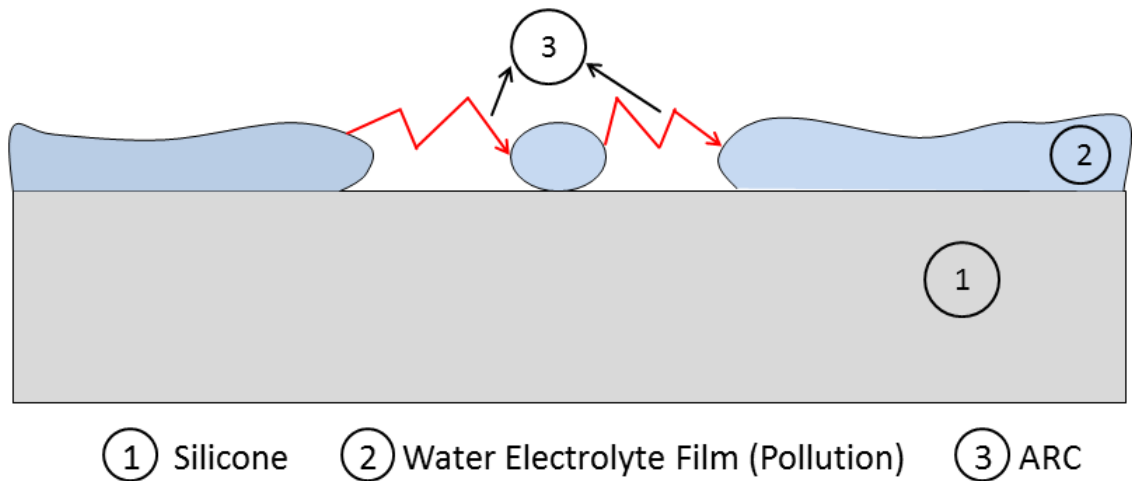
4.2.4 Flashover under Contaminated Conditions

Flashovers of insulators under contaminated conditions are a limiting factor for outdoor power delivery [8]. Active discharge activities, which are results from metal electrode initiated corona, water droplets initiated corona and consequently dry band arcing, produce considerable Joule heating that further dries the insulator surface [99]. In such cases the dry bands widen and the electric discharges elongate. Depending on the layer resistance and arc length local discharges may extend over multiple dry bands and can eventually lead to a complete flashover [69].

4.3 Application of Microvaristor-Filled Silicone Rubber

As described above, local high electric field strength is usually the main reason of certain harmful physical phenomena, which should be prevented. For this reason, one of the most important aspects of insulator design is to reduce the electric field strength along the insulation surface, especially under wet polluted surface conditions. One option is the use of semi-conductive glazes, which reduce the electric field strength and consequently discharges on ceramic insulators. However, there is uncertainty regarding the stability in the long term [103]. The semi-conductive glaze mainly has the following functions [80]:

- Drying the insulator by the Joule heating, which is generated by a continuous current of about 1 mA flowing through the semi-conductive glaze.

- Homogenization of the voltage distribution along the insulator surface with the semi-conductive glaze. It reduces the resistance of the dry bands and thereby reduces the electric field strength across the dry bands.

However, it is difficult to produce the glazes with desired electrical properties. These properties are strongly depending on the firing process during the production. In order to obtain the desired conductivity, the firing process should be repeated many times, leading to significantly increased costs. To get rid of this problem, another option is adopted to locally reduce the electric field strength, namely the use of field dependent non-linear microvaristor-filled materials.

4.3.1 Functional Principle

The microvaristor-filled materials, which have a non-linear conductivity, can be used to homogenize the electric field by bypassing dry regions in the rain test and under the wet polluted surface condition [127][P2]. The function principle of microvaristor-filled field-grading material is explained by the simplified equivalent circuit in Fig. (4.5). The insulator itself can be considered as a series connection of capacitors. The wet layers on the insulator caused by rain or humidity in the surrounding ambience are equivalent to resistors with low resistance which are connected in parallel to the capacitors. The electric field strength at the places without wet layers are significantly higher. In this case microvaristor-filled material becomes conductive and reduces the electric field strength at the dry regions and consequently the occurrence of partial discharges.

4.3.2 Modelling of Wet Polluted Surfaces

It is not simple to model the wet contaminated layers on the surface of insulators since the performance of insulators is strongly affected by the severity and type of pollution [2]. In

Figure 4.5: Simplified equivalent circuits without and with microvaristor-filled composites for the dry and wet insulators.
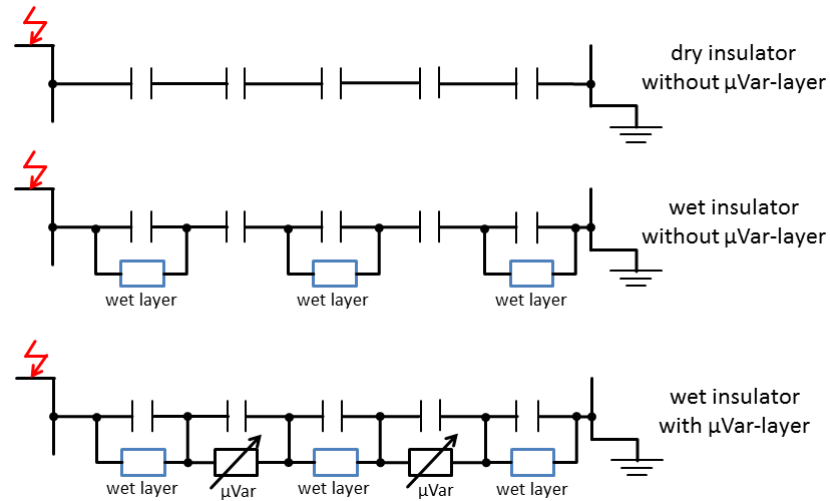
the case of fog, tiny water droplets move slowly in random motion so that they can reach the insulator surface from almost any directions. In this case, wet pollution layers can be modelled as constant and uniform layers and the electric field is relatively uniformly distributed along the surface of the insulator. In comparison to the fog condition, under light or medium artificial rainfall, the areas which face the rainfall are considered to be high wetting regions, whereas the regions under the shed surface are lowly wetted and are assumed to be almost dry, as demonstrated in Fig. (4.6). The corresponding modelling of wet surfaces is shown in Fig. (4.7). Due to the excellent hydrophobicity of the polymeric insulator, wet layers can be simplified modelled as several separate water layers as in [P2] (see Fig. (4.8)). In the highly polluted region the dew moistened polluted layers on the insulator form an uniform conductive layer. However, the electric field strength is higher under the shed to a certain extend [2], hence the water is faster vaporized from the wet pollution layer in these regions. In this case, the dry bands usually appear under each shed, as shown in Fig. (4.9). In this work, these different possibilities of modelling the wet contaminated layers are adopted to investigate the possibility of application of microvaristor-filled silicone rubber. Besides, these thin wet polluted layers can be modelled as thin 3D volumes and as 2D surfaces. The use of 2D thin layer modelling results in the reduction of simulation time and modelling complexity, as is shown in [128][130].

4.3.3 Material Parameters and Applied Voltage

In this subsection the material parameters and the applied voltage used for FEM simulations are given.

Figure 4.6: Subdivision of the pollution layer on the insulator under light and medium rain conditions into the highly wetted and the nearly dry regions.
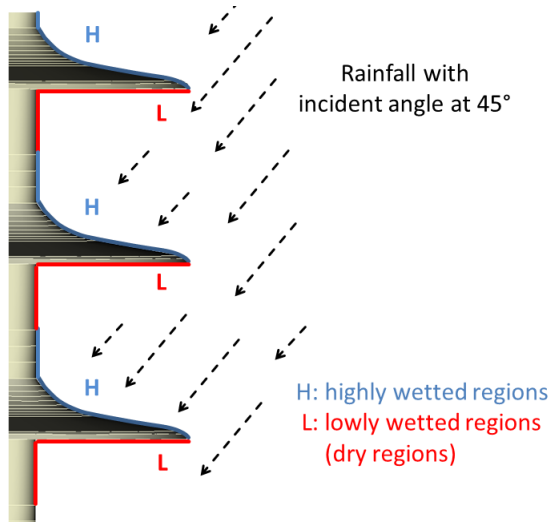
Figure 4.7: Modelling of the wet layers on the surface of an insulator. The regions under the shed surface are considered to be dry.
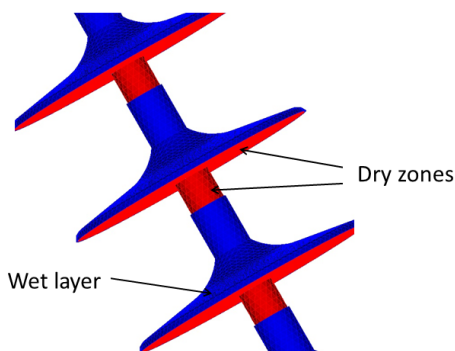
Figure 4.8: Modelling of the wet layers on the surface of insulator. Due to the hydrophobicity of the polymeric material the wet layers are modelled as separate water rings [P2].
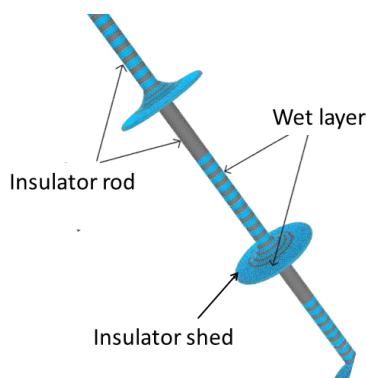
Figure 4.9: Modelling of the wet layers on the surface of insulator. The dry bands appear on the rod of the insulator under each shed.
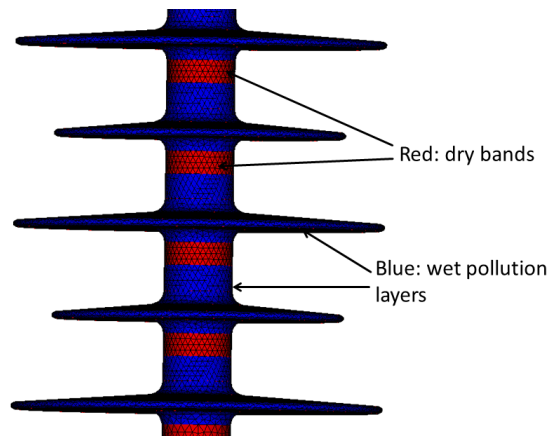
Material Parameters

The material parameters applied for FEM simulations are summarized in Table (4.1). The high-voltage cables, corona rings, end fittings and the traverse are modelled here as perfect electric conductors (PEC).

Table 4.1: Material parameters for insulators featuring microvaristor-filled silicone rubber

Material	rel. permittivity ε_r	conductivity κ
Silicone	3.2	0.0
Glass-fibre reinforced plastic	4.0	0.0
Air ambient	1.0	0.0
Water droplets	81.0	50 μS/m
Wet polluted layer	81.0	100 μS/m
Microvaristor-filled silicone rubber	12.0	see Fig. (4.10)

Applied Voltage

The simulations are performed at different voltage levels. To simulate insulators operated under nominal- and over-voltage, a sinus AC voltage with a frequency of 50 Hz is applied in both cases. Due to a rapid application of the voltage to the non-linear microvaristor-filled material, a switch-on effect can occur. In order to minimize the switch-on effect, the sinusoidal voltage is multiplied with a linear increasing function for the first period. The resulted normalized applied voltage profile is shown in Fig. (4.11). The results are evaluated at the third period, where the switch-on effect is considered to have vanished.

Figure 4.10: The non-linear electric conductivities of the microvaristor-filled silicon rubber with different switching points. Here, the switching point is defined as the point, at which the current density reaches $0.13 \ \mathrm{mA/cm^2}$.
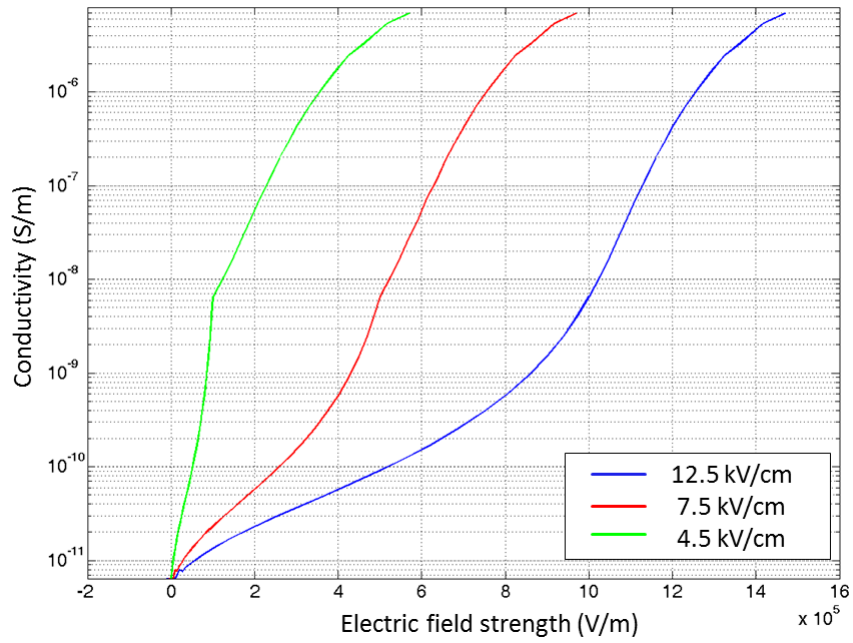
Figure 4.11: Normalized applied voltage for the simulations.
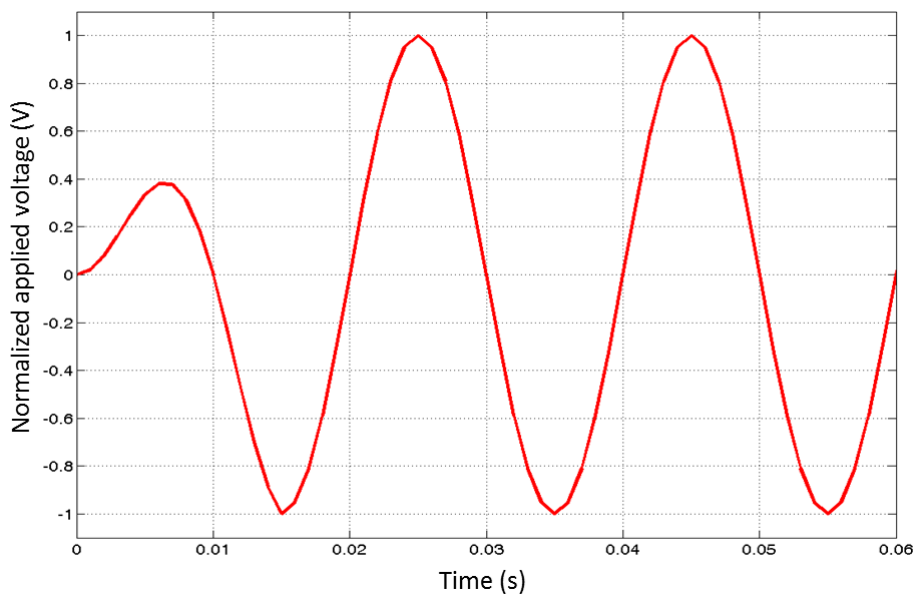
4.4 Investigation of Applications of Microvaristor-filled Material Directly onto the Surface

There are different possibilities to apply microvaristor-filled silicone rubber to insulators. For example, one option is to apply this material directly on the surface of insulators. In this section the field grading effects of microvaristor material for different geometrical configurations and under different surface conditions are investigated.

In the investigations, four variations of insulators with different geometrical configurations, as shown in Fig. (4.12), are investigated: conventional insulator; with microvaristor sheds and conventional rod; with microvaristor rod and conventional sheds; with microvaristor sheds and microvaristor rod.

Figure 4.12: Four variations of long rod insulators without and with microvaristor materials.
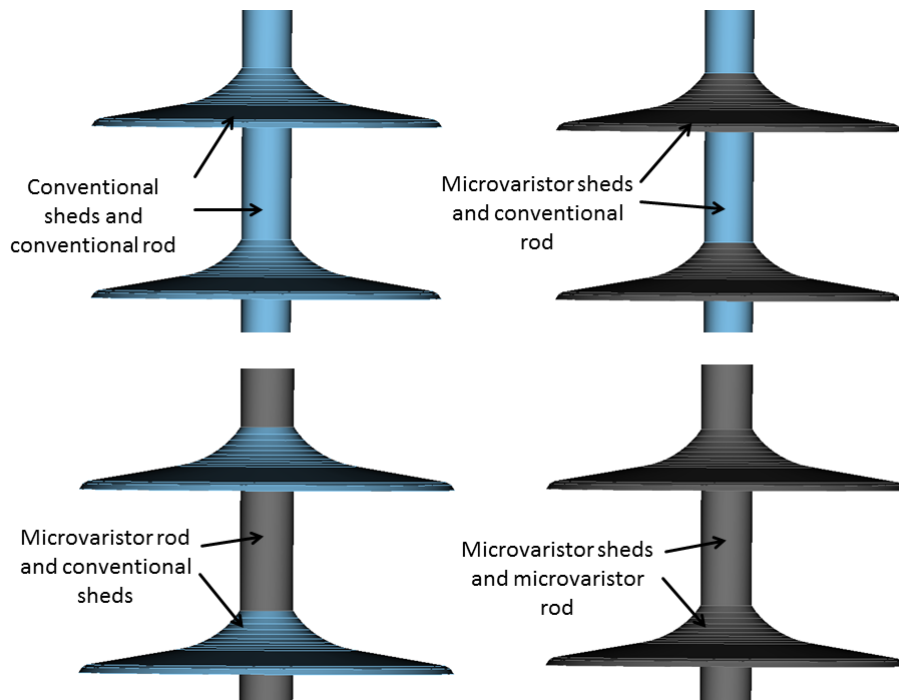
4.4.1 Homogenization of the Potential Distribution under the Dry Surface Condition

For this case, 170 kV insulators ($U_\mathrm{n} = 170$ kV) with the dry surface condition under the nominal voltage and over-voltage are investigated first. The results are evaluated along the surface of the insulator from the grounded end fitting to the energized end fitting. In Fig. (4.13) the simulated 3D model and the evaluation line along the surface of the insulator are illustrated. The 3D model consists of a grounded traverse with grounded end

fitting, an insulator with 17 sheds, a corona ring for the energized side and the high-voltage cable with energized end fitting.

Figure 4.13: The simulated 3D model of the 170 kV insulator (left) and the evaluation line along the surface of the insulator (right).
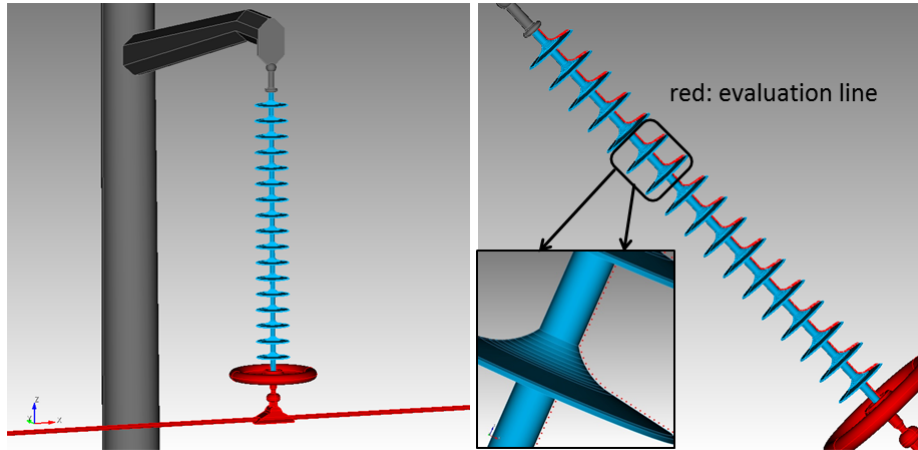
FEM simulations under the electro-quasistatic approximation are carried out to simulate the potential and the tangential electric field distributions along the surface of the insulators. In Fig. (4.14), the potential distributions from the grounded end fitting to the energized end fitting at the peak value ($U_{\text{peak}} = 139$ kV) of the third period are presented. The potential distributions along insulators with microvaristor components are almost the same as for the conventional insulator. This indicates that the microvaristor-filled material is insulating with the dry surface condition under the nominal voltage, which is expected because the microvaristor component should be insulating under the nominal voltage to avoid the increase of the leakage current and consequently preventing increasing energy losses and thermal breakdown.

If over-voltage occurs in the power grid, local high electric field strengths may appear, leading to partial discharges along the the surface of the insulators. In this case, the microvaristor-filled silicone rubber is supposed to become conductive to reduce the high electric field strengths. Fig. (4.15) illustrates the potential distributions along the surface of insulators at over-voltage ($U_{\text{peak}} = 594$ kV). The results indicate that the potentials are homogenized at the end of the energized end fitting by applying the microvaristor-filled material to the rod of the insulator and to both the rod and the sheds of the insulator. If the microvaristor-filled material is just applied to the sheds of the insulator, the potential distribution is very similar to the one of the conventional insulator. For this reason, both configurations, microvaristor applied on both the rod and the sheds and microvaristor just applied on the rod, have a better performance. The homogenization of the potential distributions at the energized side results in a reduction of the electric field strength, as

Figure 4.14: The potential distributions of 170 kV insulators for the different geometrical configurations at the peak value of the nominal voltage $U_{\mathrm{peak}} = 139$ kV. The applied microvaristor-filled silicone rubber has the switching threshold at 12.5 kV/cm. The vertical lines mark the positions of the shed peaks.
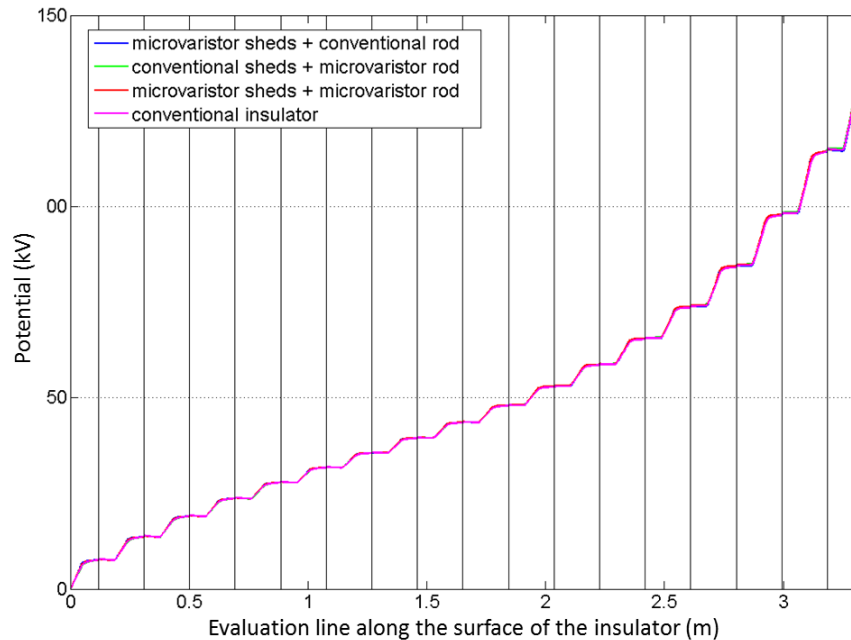
shown in Fig. (4.16). This homogenization effect is more obvious using the microvaristor-filled silicone rubber with lower switching points.

4.4.2 Prevention of Water Corona Discharges

To investigate the field grading effect of microvaristor-filled silicone rubber at the triple points of water droplets, a model with a static single water droplet on the silicone rubber with and without microvaristor material is developed. In [T1] the behavior of water droplets on silicone rubber, depending on the contact angles, the shape of the water droplets, the distance between the two water droplets and the number of water droplets, is systematically investigated. Fig. (4.17) shows the simulated models with and without the microvaristor-filled component for a water droplet under the tangential electric field strength. The water droplets are modelled as a hemisphere. The distance between the two parallel conductors in Fig. (4.17) is 5 cm and the applied voltage is 30 kV. Fig. (4.18) shows that the high electric field strengths at triple points of water droplets can be reduced by using the microvaristor layer. Consequently, the water droplets corona discharges are reduced as well.

In [T1] a few water droplets are placed on the rod and the sheds of a 420 kV insulator to investigate the field grading effect of the microvaristor-filled silicon rubber layer at the triple points of the droplets. The simulated model is demonstrated in Fig. (4.19). The

Figure 4.15: The potential distributions of 170 kV insulators for the different geometrical configurations at the peak value of the over-voltage of $U_{\text{peak}} = 594$ kV of the third period. The vertical lines mark the positions of the shed peaks.
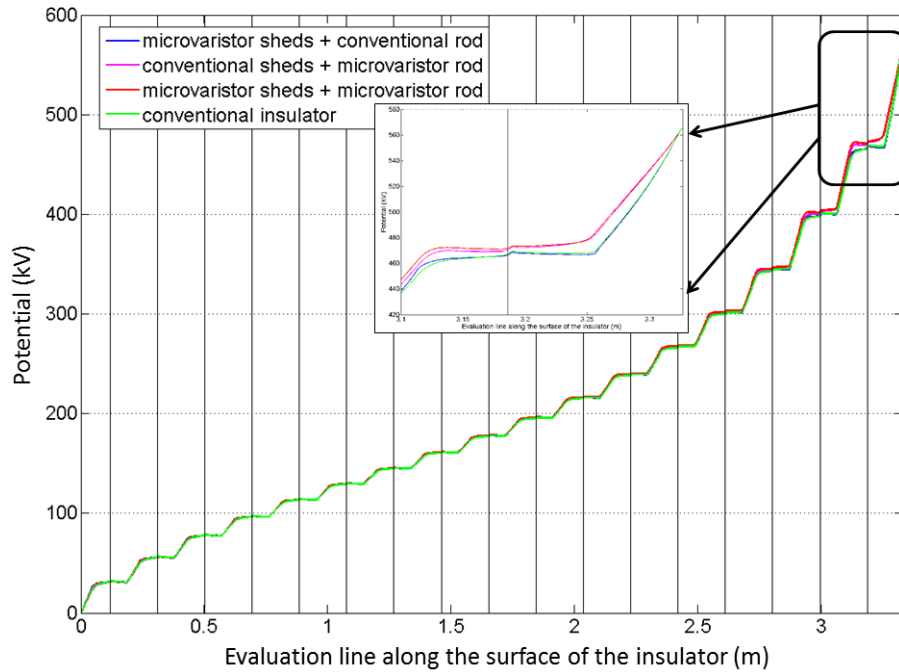
Figure 4.16: The electric field distribution at the energized side of the insulators at the over voltage of $U_{\text{peak}} = 594$ kV. The vertical lines mark the positions of the shed peaks.
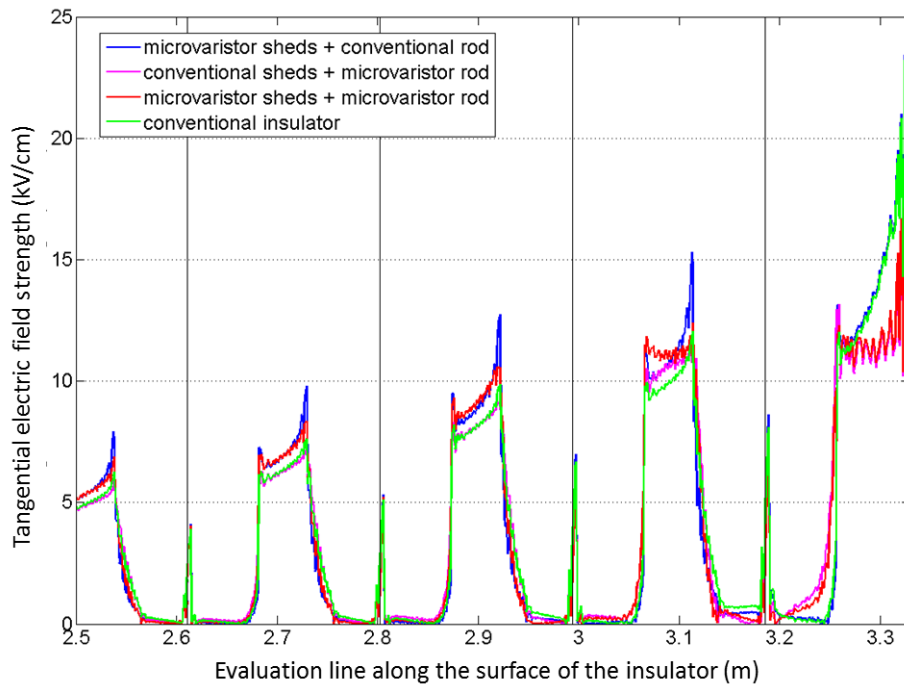
Figure 4.17: The simulated models of a static water droplet under the tangential electric field strength. Green: microvaristor layer; Magenta: silicone rubber; Blue: water droplet; Red line: evaluation line.
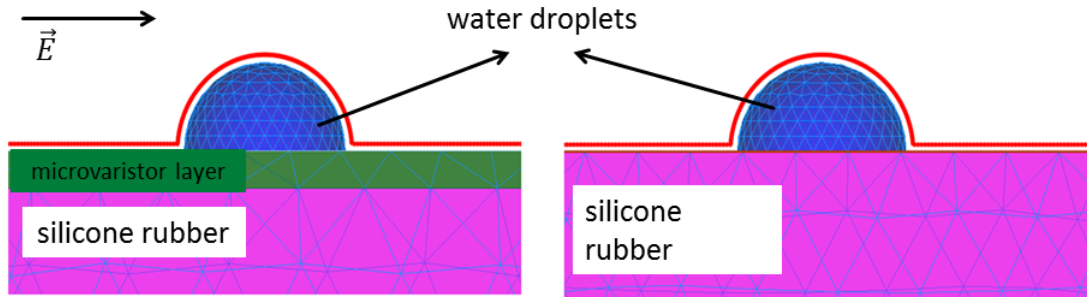
Figure 4.18: The field grading effect at the triple points of water droplets by using the microvaristor layer at the voltage of $U_{\mathrm{peak}} = 30$ kV.
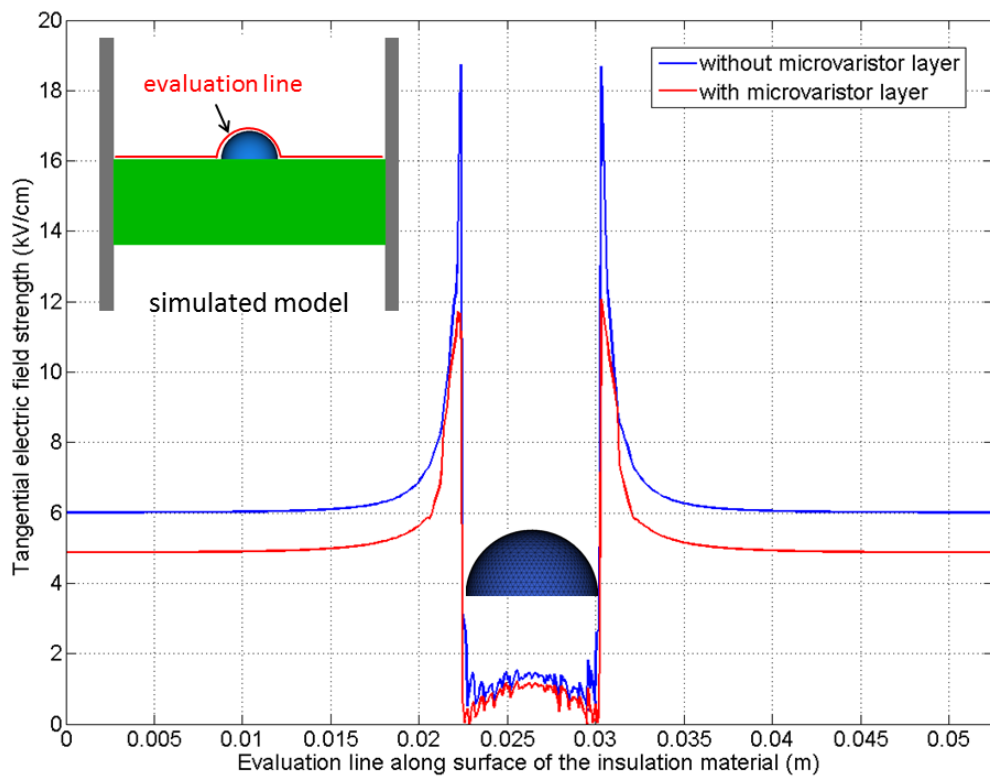
results of the FEM simulations in Fig. (4.20) show that the maximal electric field strength $E_{\mathrm{max}} = 18.5$ kV/cm at the triple points can be reduced to the $E_{\mathrm{max}} = 15$ kV/cm by the application of the microvaristor-filled silicone rubber layer.

Figure 4.19: A few water droplets on the rod and the sheds of a 420 kV insulator.
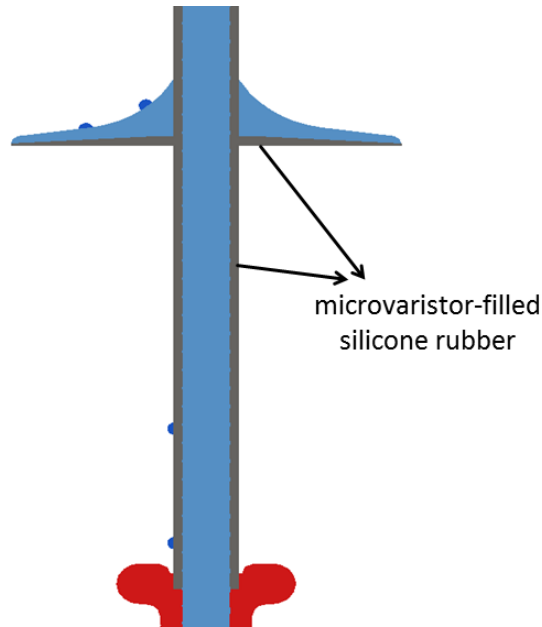
4.4.3 Prevention of the Dry Band Arcing

The formation of dry bands on outdoor insulators is quite complicated. This process is supposed to be dynamical and in this subsection, the simulated models considering the water pollution are simplified. Under light rain conditions, the surface area on the insulator facing the rainfall is exposed to water, whereas the downfaced areas located under the sheds are assumed to be dry. The pollution layer is subdivided into two main regions namely: a highly wetted area and a low wetted area. The moisture from the rain can easily reach the highly wetted area without any obstacles. The low wetted regions are protected by the sheds, consequently considered to be the nearly dry regions. For simulations the wet polluted layers are considered to have a homogeneous material property. A section of the 170 kV insulator structure used for the simulations with the wet pollution layers is shown in Fig. (4.21).

The simulation results at $U_{\mathrm{rms}} = 98$ kV are plotted in Fig. (4.22). The tangential electric field peaks for the insulator configurations with microvaristor material on both the rod and microvaristor material on the rod and the sheds are reduced. As expected, the tangential electric field strength at the over-voltage $U_{\mathrm{rms}} = 420$ kV is significantly higher than at

Figure 4.20: Simulated electric field distribution at the end of a 420 kV insulator in the presence of a few single water droplets at the voltage of $U_{\mathrm{rms}} = 243$ kV. Left: without microvaristor layer; Right: with microvaristor layer [T1].

without microvaristor layer   with microvaristor layer
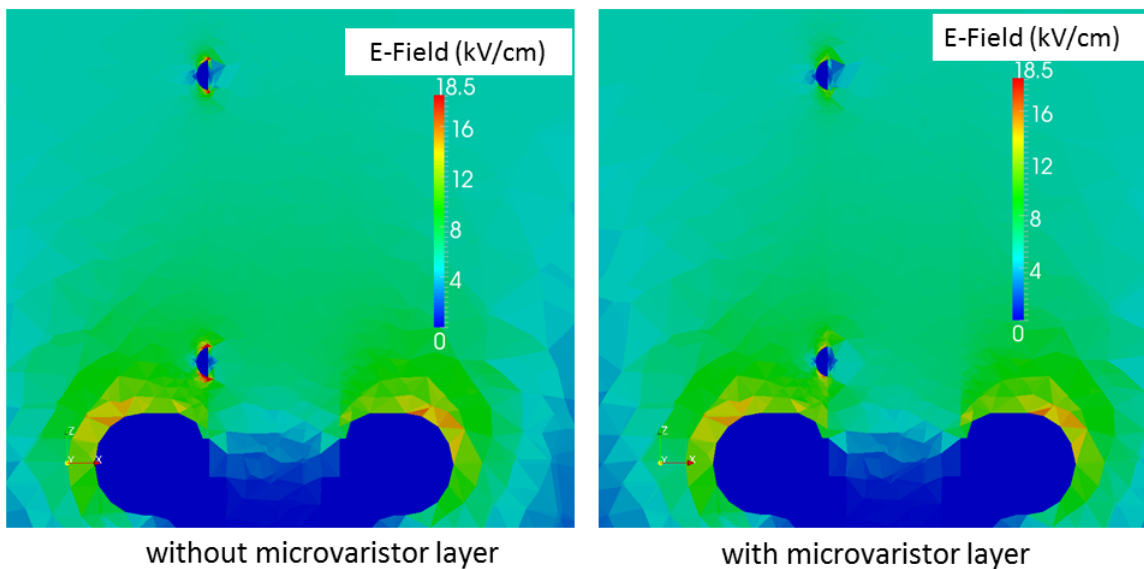
Figure 4.21: The simulated insulator structure with wet pollution layers. The surfaces of the insulator facing the rainfall are highly wetted regions. The surfaces under the sheds are considered to be dry.
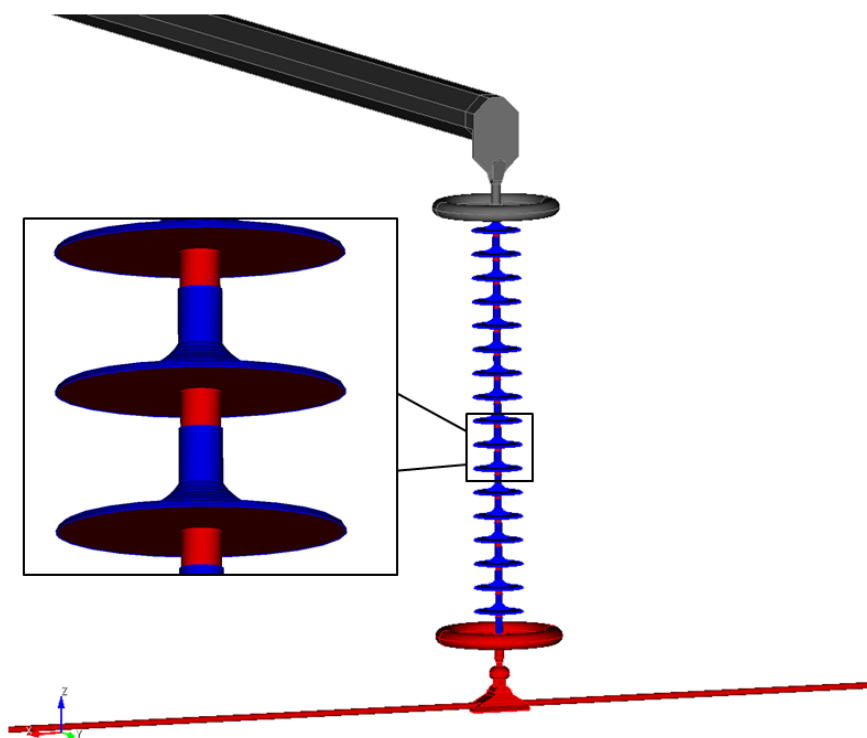
$U_{\text{rms}} = 98$ kV, as shown in Fig. (4.23). The dotted red horizontal lines mark the electric field strength $E = 30$ kV/cm [102], at which the breakdown of the air may occur. Only for the insulator with microvaristor material on the rod and the insulator with microvaristor material both on the rod and the sheds, the tangential electric field strength does not exceed this value. Besides, the configuration with microvaristor material on the rod and sheds outperforms the other configurations. The corresponding potential distributions along the surface of the insulators are illustrated in Fig. (4.24). These results also indicate the homogenization effect of the potential by applying the microvaristor material on the rod and on both the rod and the sheds.

Figure 4.22: Tangential electric field distributions along the surface of the insulator at $U_{\text{rms}} = 98$ kV. The red crosses refer to the positions of the shed peaks.
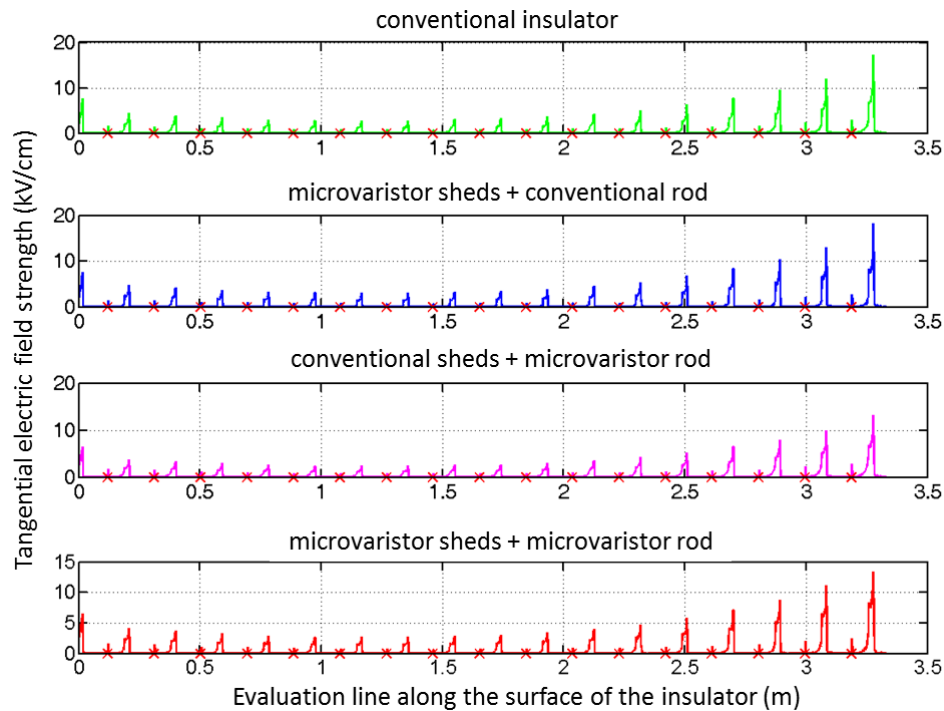
In [P2] the investigation of a 420 kV insulator with 10 sheds and a length of 2930 mm in rain test is carried out. The rain is modelled as separate conductive water rings on the wet regions of the water-repellent composite insulator. The results also indicate the positive effect of applying the microvaristor material at least on the rod of the insulator.

4.4.4 Experimental Results

Partial discharges

In the high-voltage laboratory at the Technische Universität Darmstadt, the four configurations of 420 kV insulators with and without microvaristor-filled material were built up

Figure 4.23: Tangential electric field distributions along the surface of the insulator at $U_{\mathrm{rms}} = 420$ kV. The red crosses refer to the position of the shed peaks. The dotted red horizontal lines mark the electric field strength $E = 30$ kV/cm, at which the breakdown of the air may occur.
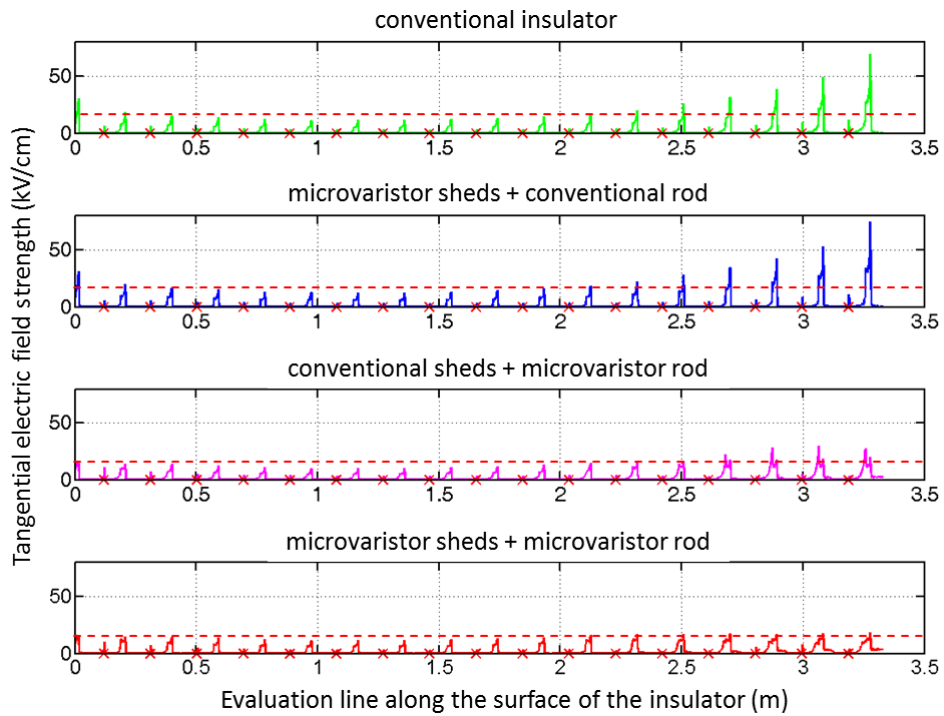
Figure 4.24: Potential distributions along the surface of the insulator at $U_{\mathrm{rms}} = 420$ kV. The black vertical lines refer to the shed peaks of the insulator.
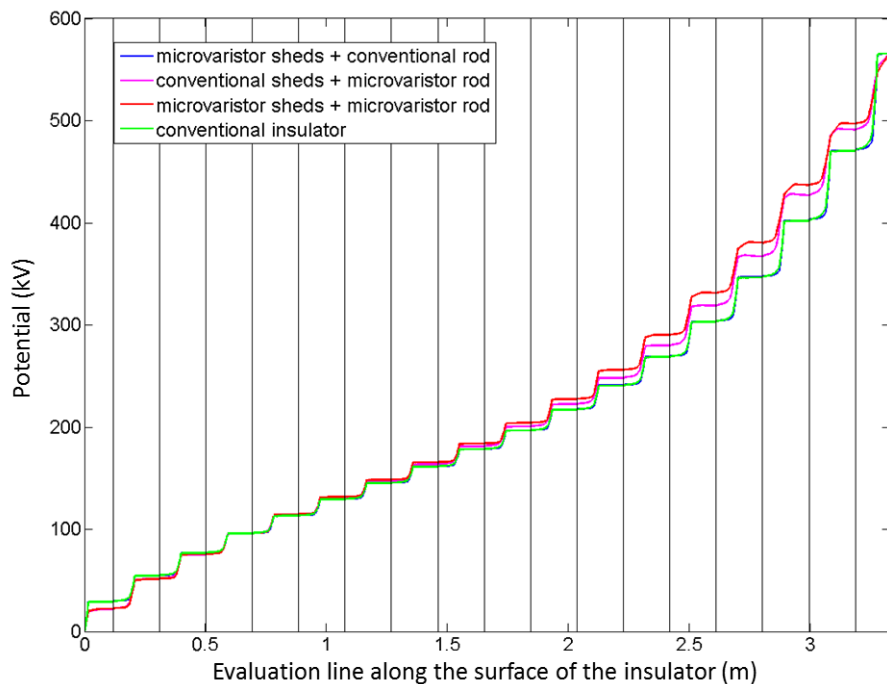
und investigated. Partial discharges were measured under the rain test. The experimental results are shown in Fig. (4.25). For the insulator with microvaristor material on the rod and sheds no discharges are visible, neither on the rod nor underneath the sheds. The insulator with microvaristor material on the rod also performs well. For the conventional insulator, there are obvious discharges under the last two sheds at the energized side. These results indicate that the electric field strength is reduced by using the microvaristor material, consequently the partial discharges. More information about the experiment can be found in [24][107]. The experimental results show quite a good agreement with the FEM simulation results shown in subsection 4.4.3.

Figure 4.25: Partial discharges along the insulators with different configurations [107].
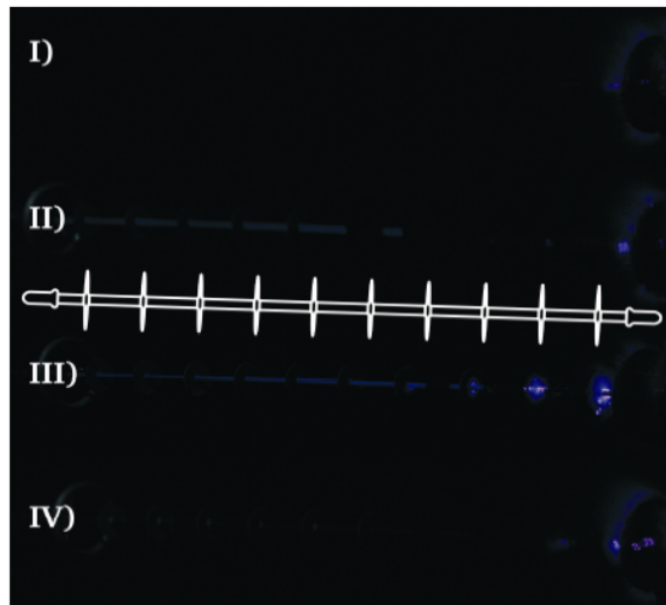
I)   microvaristor rod + microvaristor sheds
II) conventional rod + microvaristor sheds
III) conventional insulator
IV) microvaristor rod + conventional sheds

Testing of tracking and erosion

For outdoor applications, the tracing and erosion resistance of the insulation material is very important. For this aim, an inclined plane test and a weather ageing test under salt fog are carried out in [24]. The insulators with microvaristor-filled material show no deterioration of the insulation material at all. However, in the inclined plane test the microvaristor-filled silicone rubber shows rather good, but not sufficient tracking and erosion resistance.

To improve the outdoor applicability a microvaristor-filled silicone rubber with lower switching point could be more suitable or a thin protection layer of silicone rubber can be applied on the surface of the microvaristor-filled silicone rubber to avoid exposition of the microvaristor material environmental stress.

4.5 Investigation of Application of the Microvaristor Material under a Silicone Layer

As mentioned in the last section, to improve the outdoor performance of the insulator featuring microvaristor-filled material, a protection layer of silicone rubber can be applied on the microvaristor layer. In this section, the electrical behavior of insulators featuring a microvaristor layer and a protection layer on top of it are investigated.

4.5.1 Simulated Insulators

The starting point of the investigation is a realistic 3D model of a 765 kV long rod composite insulator, which is about 6 m long and has 20 sheds each at the energized and grounded end fittings. The whole 3D model for the electrical simulations consists of a 38 m high traverse, the insulator with corona rings and the attached transmission lines, as illustrated in Fig. (4.26). The microvaristor material is modelled as a cylindrical layer along the rod and covered by a silicone rubber protection layer. Near the energized end fitting the microvaristor material is modelled as a cone-shape layer, which accommodates the high field in these regions and allows better adhesion of the silicon rubber housing [3]. The electric field distributions of the configurations of a 2 mm thick microvaristor-material layer with a cone-shaped layer and without a cone-shape layer at the end of the insulators are compared in Fig. (4.27) and Fig. (4.28). The results indicate that the configuration without the cone-shaped microvaristor layer has a greater tangential electrical field strength at the end of the insulator for both dry and wet surface conditions. Hence it is better to use the cone-shaped microvaristor layer at the energized end of the insulator.

The whole model is located in a calculation domain with the dimension 16 m x 35.9 m x 45.2 m. The traverse, the grounded upper end of the insulator and the bottom surface of the calculation domain are set to Dirichlet boundary conditions of 0 V. The transmission lines, the lower end of the insulator and the corona ring are applied with a sinusoidal volatage of U_n = 765 kV, corresponding to a phase voltage with the effective value of U_rms = 442 kV. The surfaces of the calculation domain which cut the transmission lines off are set to homogeneous Neumann boundary conditions.

Figure 4.26: The simulated 765 kV insulator with a traverse and the transmission lines and a cut-view of a section of the insulator with microvaristor layer [P7].
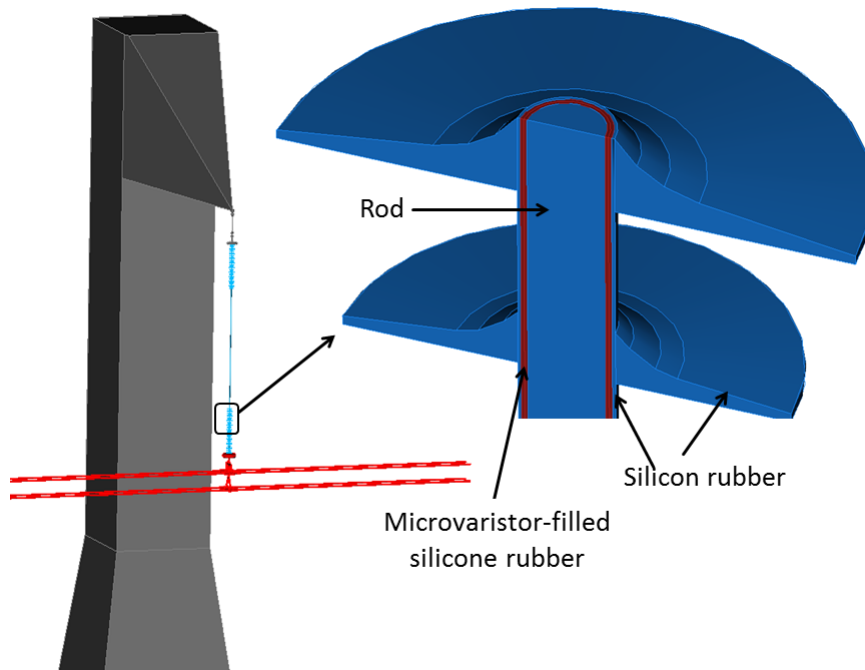
Figure 4.27: The tangential electric field distributions for the configurations with and without cone-shaped material layer under the dry surface condition [P7].
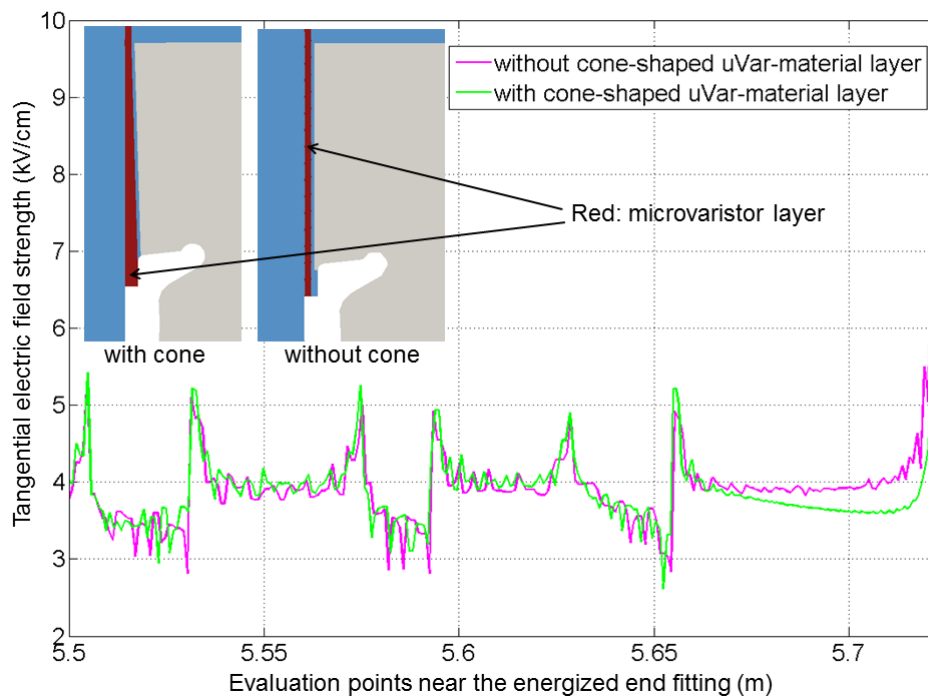
Figure 4.28: The tangential electric field distributions for the configurations with and without cone-shaped material layer in the presence of a few water drops on the surface [P7].
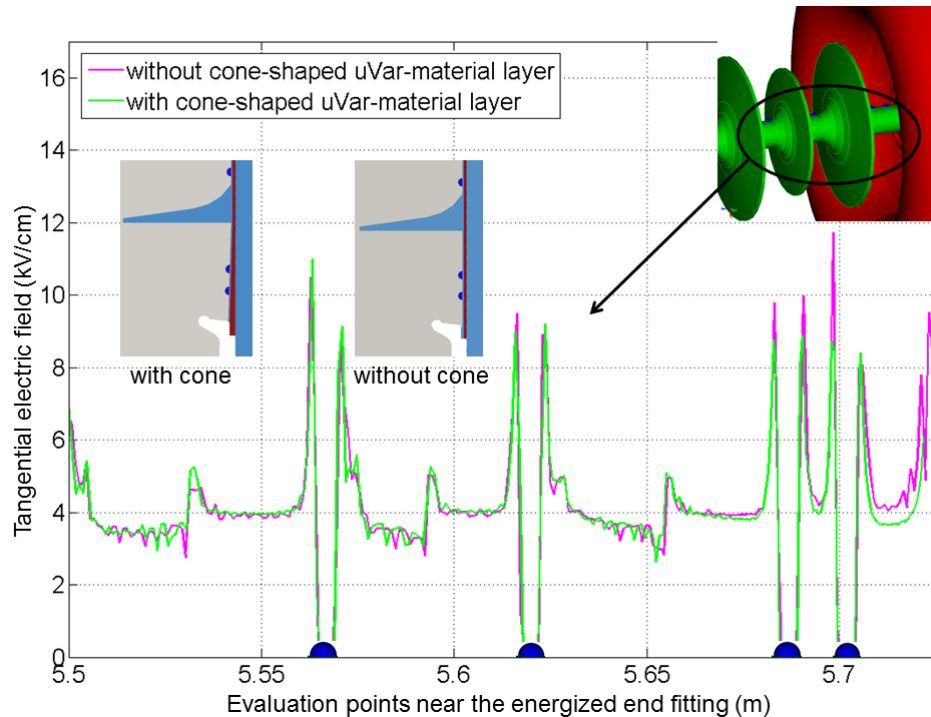
4.5.2 Reduction of the Electric Field Strength for Dry Conditions

To better homogenize the potential distributions and consequently the electrical field strength, the microvaristor-filled silicone rubber with lower switching points are investigated. In Fig. (4.29) the tangential electrical field distributions near the energized end fitting using microvaristor-filled composite materials with different switching points are shown. The switching points of these two composite materials are 4.5 kV/cm and 5.5 kV/cm respectively, according to the definition of the manufacturer ABB, namely the point at which the current density is 0.13 mA/cm^2. The results demonstrate that the electric field strength can be better damped using the lower switching point. However, the switching point should not be too low. This is because the microvaristor material produces Joule heating if it becomes conductive. Hence, the switching point should be above the nominal electric field strength to avoid thermal instability and energy losses.

4.5.3 Prevention of Water Corona Discharges

The microvaristor layer can also reduce the high electric field strength at the triple points of the water drops if they are on the surface of the protection silicon layer near to the energized end fitting, as demonstrated in Fig. (4.30). For simulations, the water droplets are modelled as a hemisphere which has a 90° contact angle with the silicon surface.

Figure 4.29: The tangential electric field distributions of the dry insulators featuring microvaristor composite materials with different switching points.
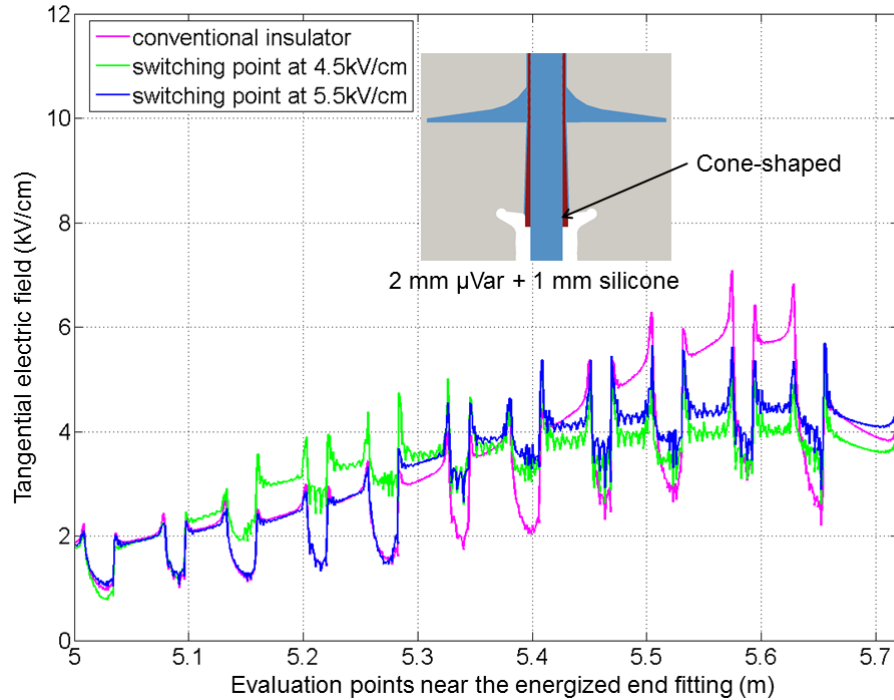
Figure 4.30: The tangential electric field distributions of the insulators featuring microvaristor composite materials with different switching points, if a few water droplets are present on the surface of the silicon protection layer.
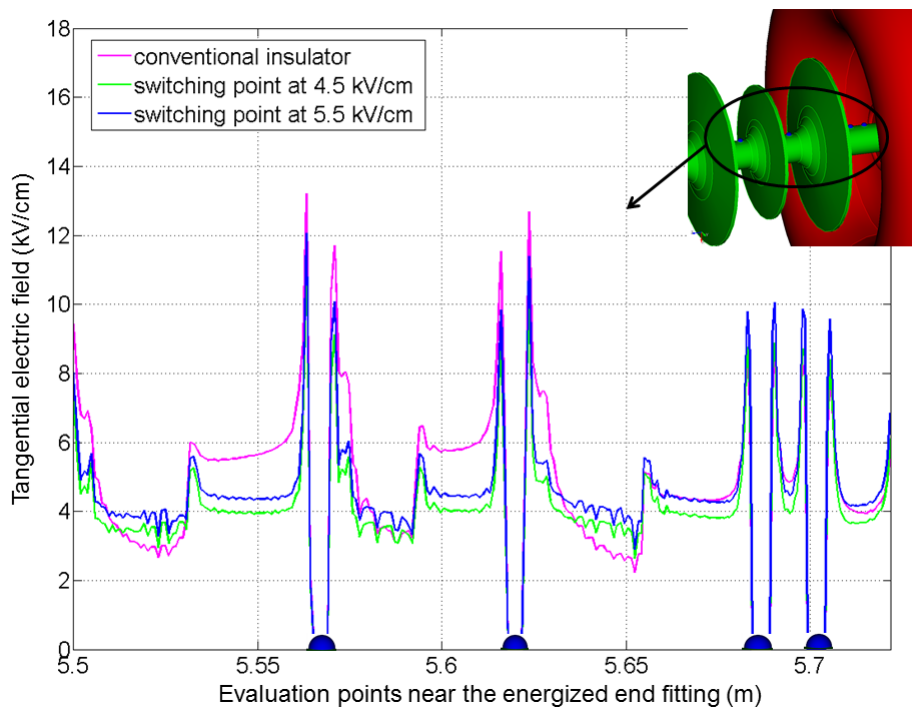
4.5.4 Effect of the Silicon Layer in the Presence of Dry Bands

As described in the subsection 4.4.3, the high electric field strength between the dry bands on the insulator surface can be reduced by applying microvaristor composite material directly onto the surface of insulators, because the current flowing through the wet pollution layers can bypass the dry bands through the microvaristor material when it becomes conductive. However, if the microvaristor layer is applied under a protection silicon layer, this effect is much less obvious. To investigate this phenomenon, a 420 kV insulator is simulated and the dry bands are modelled as 1 cm wide rings and are located under the sheds, as shown in Fig. (4.31). The wet polluted layers are 1 mm thick and have a relative permittivity of 81 and a conductivity of 100 µS/m. The microvaristor composite material with 5 kV/cm switching point is covered by a 2.5 mm thick silicone rubber layer.

Figure 4.31: The positions of the dry bands under the sheds. The width of the dry bands is 1 cm.
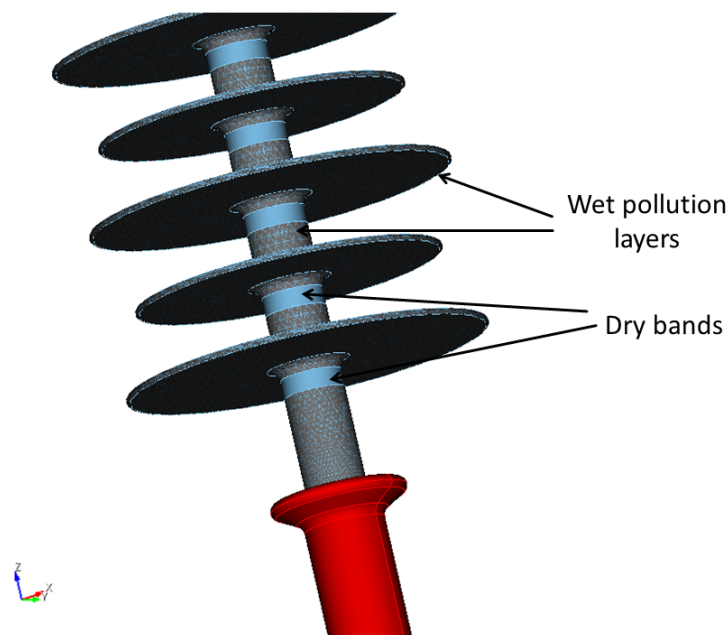
The simulation results are shown in Fig. (4.32) and compared with a conventional insulator and the insulator with the microvaristor layer direct on the insulator surface. As seen in the figure, the high electrical field strength appearing between the dry bands near the energized end fitting can be slightly reduced using the microvaristor layer under a silicone layer, whilst the electric field strength can be damped much more by applying the microvaristor material directly onto the insulator surface. The reason is that the protection silicone layer can be seen as a capacitor C_{ins}, which prevents the current from flowing through the microvaristor layer under the low frequency of 50 Hz. Equivalent circuit representations for this are shown in Fig. (4.33).

Figure 4.32: The tangential electric field distributions of the conventional insulator, the insulator with microvaristor material under a silicone layer and the insulator with microvaristor directly applied on the surface in the presence of dry bands under the each shed. The results are evaluated at the peak value of the voltage.
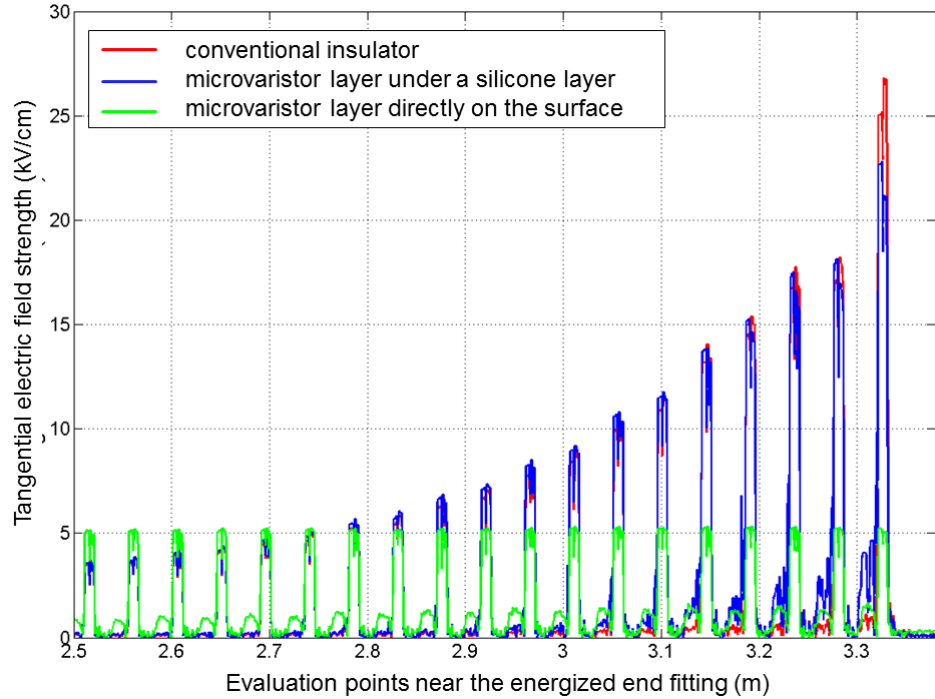
Figure 4.33: The equivalent circuits for the explanation of the effect that the electrical field strength is slightly reduced by applying the microvaristor layer under a silicone layer. R_{pol}: resistance of the wet polluted layer; C_{dry}: capacitor of dry band; C_{ins}: capacitor of the silicone layer; $R_{\mu Var}$: non-linear resistance of the microvaristor layer.
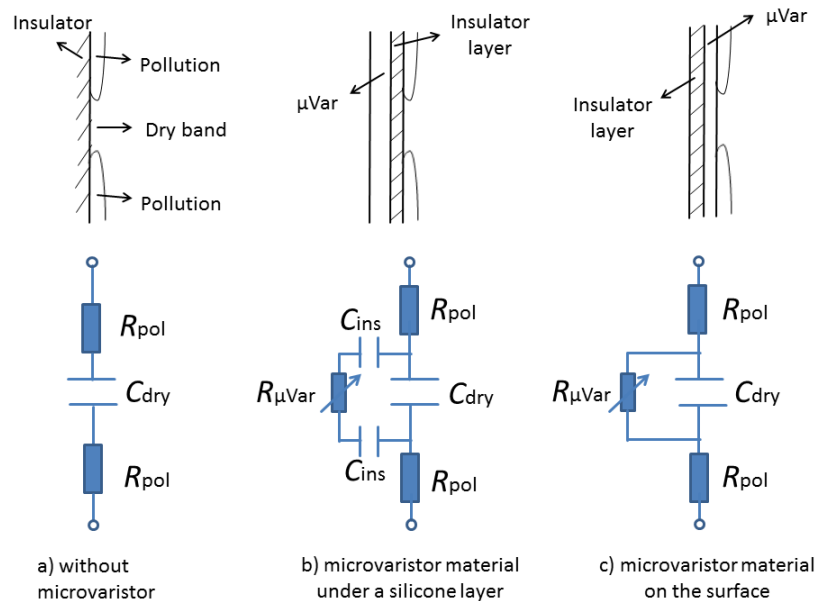
4.5.5 Influence of the Switching Point of the Microvaristor Layer

The influence of the switching point of the microvaristor-filled composite material for the reduction of the electric field across the dry bands under every shed is investigated. In Fig. (4.34) the tangential electric field distributions for insulators with the microvaristor layer with two different switching points are presented. Using the microvaristor with lower switching point can further reduce the electrical field strength in the critical regions near to the energized end fitting for a few percentages. However, it is noticeable that the switching point of the microvaristor should not be too low. The reason is that if the switching point is too low, the microvaristor material is conductive under the nominal voltage. In this case, a large leakage current will flow through the microvaristor layer resulting in certain energy losses under permanent operation and consequently thermal damage to the material.

Figure 4.34: The tangential electric field distributions of the 420 kV insulator featuring microvaristor materials with different switching points. The peak of electric field appears across the dry band under the last shed near the energized end fitting.
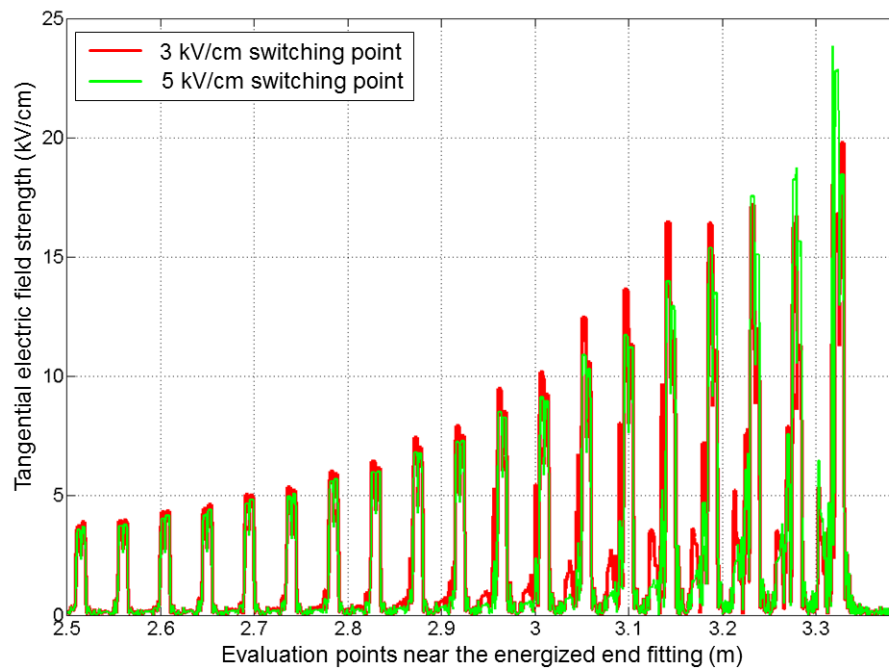
4.5.6 Influence of the Thickness of the Silicone Layer

The thickness of the protection silicone layer may have an influence of the electric field distribution along the surface of the insulator. In [P7] different geometrical configurations of insulators with microvaristor layer are adopted for FEM simulations to investigate this influence, under the dry surface condition and a few water droplets on the insulator surface. As reported in [P7], the peak of electric fields can be better homogenized by the

configuration using 2 mm thick microvaristor material covered by a 1 mm thick silicone rubber layer than the configuration using 1 mm thick microvaristor layer covered by 2 mm thick silicone rubber layer. This effect is much more obvious for the dry surface condition than a few water droplets on the surface.

To investigate the influence of the silicone layer on the electric field distribution in the presence of dry bands, a small insulator, which is almost 0.4 m long and has 7 sheds, is adopted. The different geometrical configurations investigated are shown in Fig. (4.35). The dry bands are 1 mm wide and located under each shed. The potential distributions and electric field distributions are respectively presented in Fig. (4.36) and Fig. (4.37). As seen in Fig. (4.36), the potential distribution is globally better homogenized if the silicone protection layer is thinner. However, the locally high peak values of electric field strength, which are at the edges of wet pollution layers, are not better damped using thinner silicone protection layer.

Figure 4.35: Different geometrical configurations of the microvaristor layer and the silicone protection layer.
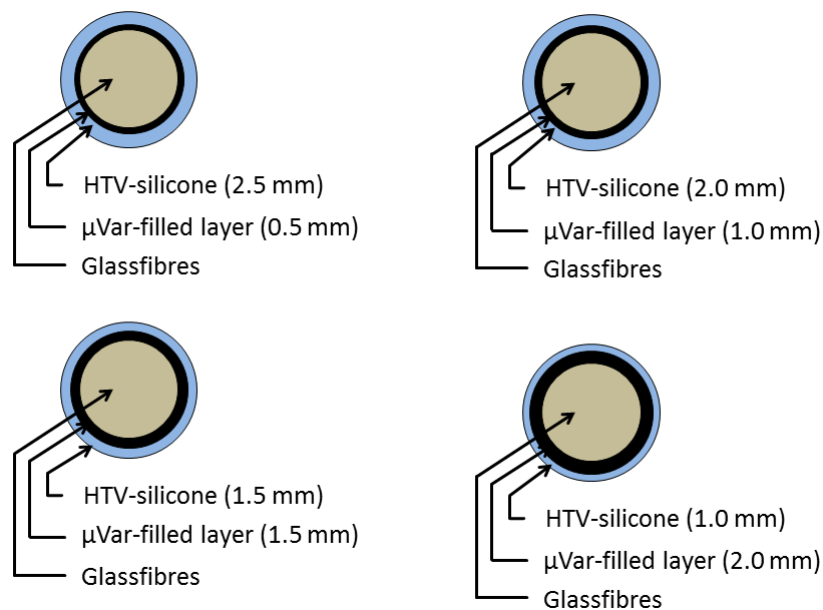
4.5.7 Experimental Results

Artificial Rain Test

For experiments in a high-voltage laboratory an insulator is produced with microvaristor-filled silicone covered by an outer layer of conventional silicone rubber with an addition of approx. 60% aluminium trihydrate (ATH) which is usually used to improve the outdoor

Figure 4.36: Comparison of potential distributions along the investigated small insulator with different geometrical configurations.
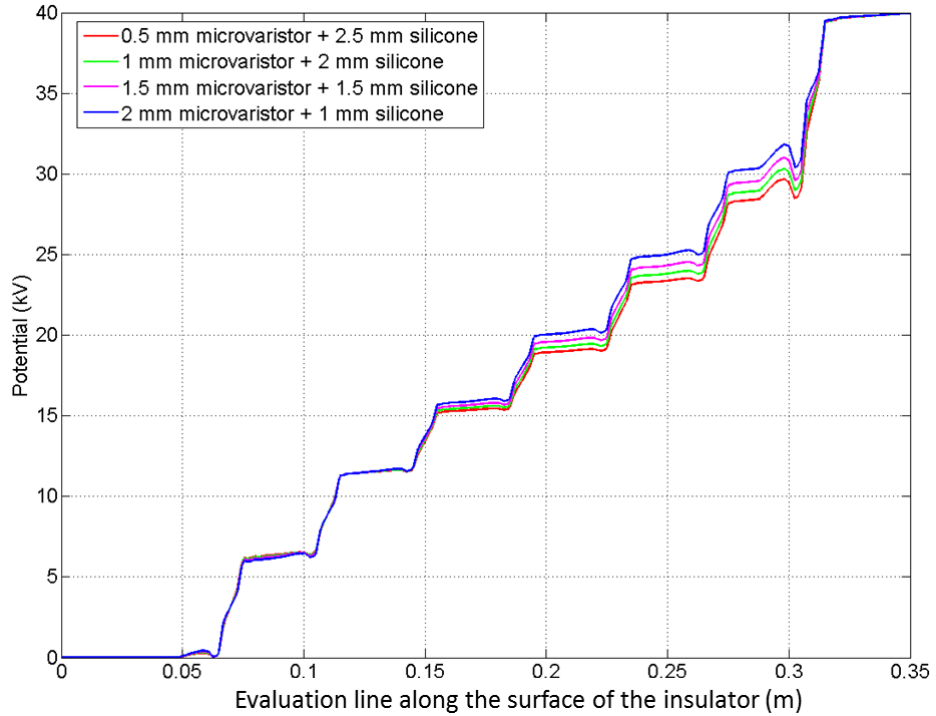
Figure 4.37: Comparison of electric field distributions along the investigated small insulator with different geometrical configurations.
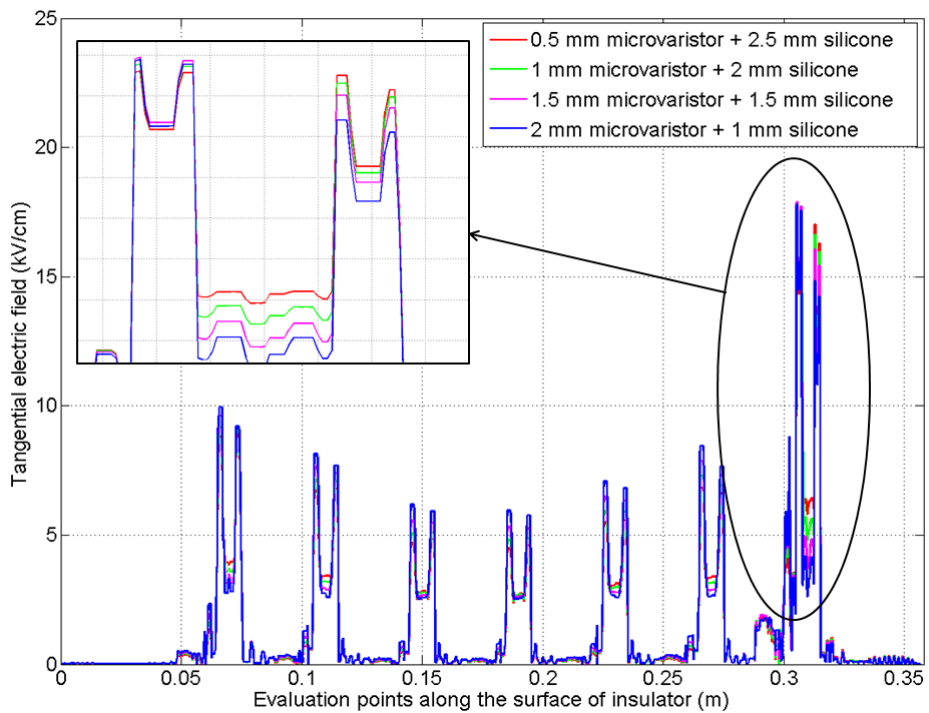
performance of polymeric insulators. The laboratory tests are carried out in the high-voltage laboratory at the Technische Universität Darmstadt. The partial discharges are measured using an UV (Ultraviolet) daylight camera. The experimental results indicate that the partial discharge activities can be reduced by using a microvaristor layer under the silicone layer. For more information the readers are referred to [23][41].

Artificial Pollution Test

Artificial pollution tests are also carried out for insulators with microvaristor composite materials under a protection silicone layer in the high-voltage laboratory at the Hochschule Zittau/Görlitz, according to the standard IEC 60507 [61]. The results indicate that the insulator with microvaristors inside covered by the silicone protection layer has nearly no improvement compared to a conventional insulator. More information can be found in [42].

4.6 Summary

In this chapter, the application of microvaristor-filled silicone rubber to outdoor long-rod insulators is investigated. FEM simulations are carried out for insulators with different geometrical configurations for the microvaristor material. If the microvaristor is applied directly on the surface of the insulator, the local high electrical field strength can be reduced well. This holds not only at the triple points of water droplets, but also across the dry bands on the surface of the insulator. The laboratory test shows quite a good agreement to FEM simulation results. However, this configuration shows quite a good field grading effect, but not a sufficient tracking and erosion resistance in the laboratory test. Thus, this configuration is not quite suitable for outdoor applications.

An option to solve this problem is to use a protection silicone layer above the microvaristor layer. Using this configuration the potential distributions along the surface of dry insulators can be homogenized and the high electric field at the triple points of water drops can also be reduced. This effect is more obvious if the protection silicone layer is thin. However, in the presence of the dry bands on the surface of the insulator, the high electric field strength across the dry bands can just be reduced slightly using this configuration. Even though choosing the microvaristor material with a low switching point can further reduce the electric field between the dry bands by a few percents, the field grading effect of the microvaristor material under a silicone layer is not as significant as for the configuration with the microvaristor direct on the surface. By reducing the thickness of the silicone layer, the potential distribution along the insulator is globally better homogenized, but the peak values of the electric field at the edges of dry bands are not better reduced.

5 Investigation of compact Bushings with Microvaristor-Filled Epoxy Resin

5.1 Introduction

The gas-insulated bushing is an insulation device in power systems which allows a high-voltage conductor to safely pass through a grounded barrier, for example the wall of a transformer. One of the main tasks of the design of high-voltage bushings is to obtain an optimal electric field distribution along the surface of the insulation materials, especially in the air side. The dielectric strength of SF_6 (Sulphur Hexafluoride), used as a gaseous dielectric medium inside the bushings, can be increased by raising the pressure. However, the pressure in the surrounding air is considered to be constant. Hence, the obvious way to prevent the breakdown of the air is to reduce the electric field strength near the surface of the insulator. A common traditional approach to reduce the electric field strength is geometrical field grading, which usually leads to an over-dimensioned product design as the voltage increases [57]. Another solution is the so-called capacitive field grading approach, which usually requires additional shielding electrodes, resulting in increased costs and higher space requirements [16]. A new option is the use of non-linear resistive field grading materials such as microvaristor-filled compounds in critical regions.

A non-linear microvaristor-filled epoxy resin component can be applied to design a compact SF_6-insulated bushing, which has a smaller diameter than conventional bushings. By placing a microvaristor-filled epoxy resin layer in the critical region, i.e. around the area of the grounded electrode, the electric field strength can be reduced and consequently partial discharges as well. This concept is illustrated in Fig. (5.1). By choosing a suitable switching point for the microvaristor-filled epoxy resin component, the diameter of 550 kV bushing can be reduced by 30%. In this case, less SF_6 gas is required. Hence, this design concept using microvaristor-filled epoxy resin leads to a more eco-friendly and economical product.

In this chapter, the non-linear electrical properties of the microvaristor-filled epoxy resin are investigated for different parameters, such as microvaristor contents and temperatures. Beside that, the application of this component in 550 kV compact bushings is computationally and experimentally tested and verified.

Figure 5.1: Comparison of a conventional bushing (left) and a compact bushing (right) with $d_1 > d_2$ [P4].
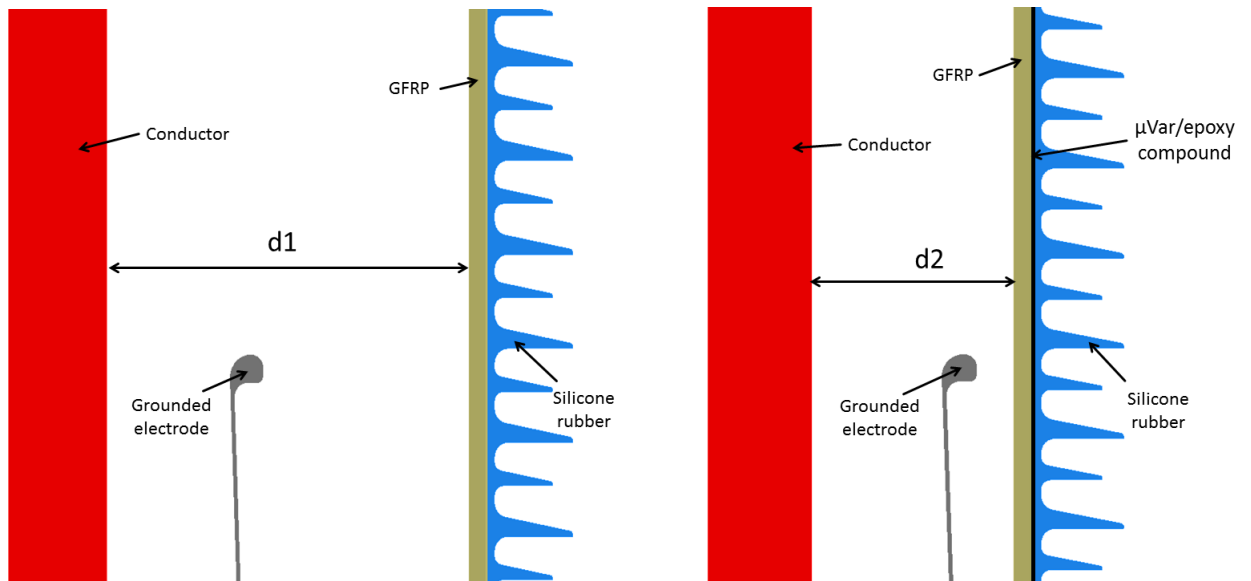
5.2 Electrical Properties of Microvaristor-Filled Epoxy Resin

As mentioned in chapter 2, microvaristor powder can be mixed with different matrices to be a non-linear functional field grading material. To get a better adhesion of the compound to the GFRP (Glass Fibre Reinforced Plastic) composite, the microvaristor powder is compounded into the epoxy resin. To systematically investigate the electrical properties of microvaristor-filled epoxy resins, microvaristor-filled epoxy resin samples with different microvaristor contents are produced and measurements of these samples at different temperatures are carried out.

5.2.1 Setup of Measurement

To measure the $E - J$ curve of microvaristor-filled epoxy resin samples, plan-parallel electrodes are adopted to achieve a homogeneous electric field strength in the measured samples. Besides, a guard ring is adopted to avoid field disturbances and surface current effects. This measurement arrangement is shown in Fig. (5.2).

5.2.2 Influence of Different Microvaristor Contents

To get a stable non-linear electrical property for microvaristor-filled epoxy resin compounds, the microvaristor filling content should be above the percolation threshold in order

Figure 5.2: Electrode configuration for measurements [P1].
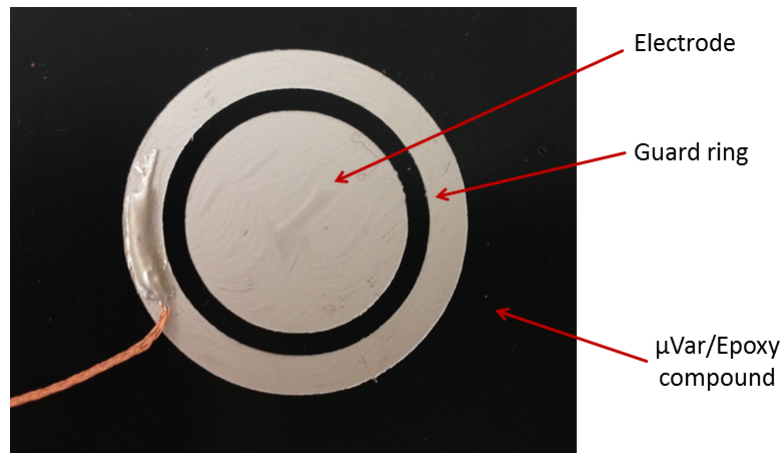
to form conductive particle-particle paths within the compounds. Compared to epoxy resin, microvaristor powder is heavier and more expensive, which is a disadvantage for the application in high-voltage devices. Hence, it is desirable to find the content of microvaristor powder necessary for industrial applications.

For this aim, samples with 65 m%, 75 m% and 84 m% filler contents (m%: mass percent) are investigated. To produce samples, microvaristor powder is mixed with epoxy resin and hardener. Besides, a little amount of a thickening agent is added into the mixture to avoid sedimentation. Then the mixture is evacuated and vacuum-cast into a planar mold with a height of 2 mm. The results of measurements under AC at room temperature are shown in Fig. (5.3). The results demonstrate that, if using microvaristors with 65 m% content, the compound does not show the non-linear property. The probable reason for that is 65 m% content is below the percolation threshold, resulting in sparse conducting paths through the sample. Above 75 m% content the compounds have an obviously sharp transition from insulating to conducting state. Hence, 75 m%, as suggested in [63], is a moderate choice considering both the reasonable electrical non-linearity and industrial application possibility.

However, if the microvaristor powder with a certain switching point $E_{b,powder}$ is mixed with the epoxy resin with 75 m% filler contents, the switching point of the composite $E_{b,composite}$ is somewhat higher than the switching point of the powder $E_{b,powder}$.

5.2.3 Influence of Different Temperatures

Temperature can also have an influence on the $E - J$ characteristics of microvaristor-filled epoxy resin compounds. It is already well-known that the characteristics of microvaristor powders are dependent on the temperature, especially in the pre-breakdown region [90].

Figure 5.3: $E - J$ AC characteristics of the 65 m%, 75 m% and 84 m% microvaristor-filled epoxy resin samples [P4].
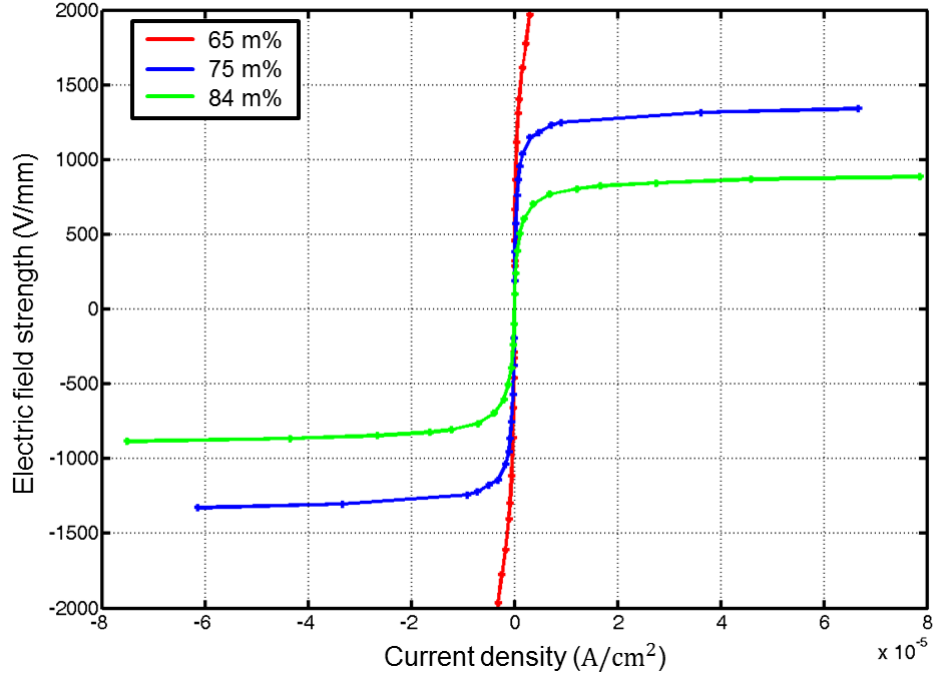
The leakage current increases with rising temperature, whereas the switching point of the microvaristor powder decreases with rising temperature. However, if microvaristor powder is mixed with epoxy resin as an insulating matrix, the thermal behavior of the epoxy resin can also affect the temperature-dependent conductivity of the whole compound.

The $E - J$ curves are measured at the different temperatures, 23°C, 30°C, 40°C, 50°C and 80°C. A temperature chamber is adopted, as shown in Fig. (5.4), to get a constant temperature in the samples and the surrounding environment. The measurement results are shown in Fig. (5.4). As seen in this figure, the electrical conductivity increases in the pre-breakdown region when the temperature rises from room temperature 23°C to 40°C. In this case, the leakage current of microvaristor particles is thermally activated. However, the electrical behavior is very similar to each other in the range from 40°C to 80°C. An explanation could be that, above a certain temperature, the thermal expansion of the epoxy resin matrix results in fewer contacts of the microvaristor particles which leads to a reduced amount of conducting paths through the samples. This effect compensates the thermal activation effect of microvaristor particles, whose conductivity increases with rising temperature. The results also indicate that the switching points of the measured sample are just slightly affected by the temperature in the range from 23°C to 80°C. Hence, this composite material can be considered to be thermally stable.

Figure 5.4: Measurement arrangement in a temperature chamber.

Figure 5.5: Double logarithmic plots of the measured $E-J$ AC characteristics of microvaristor-filled epoxy resin compound at different temperatures [P1].
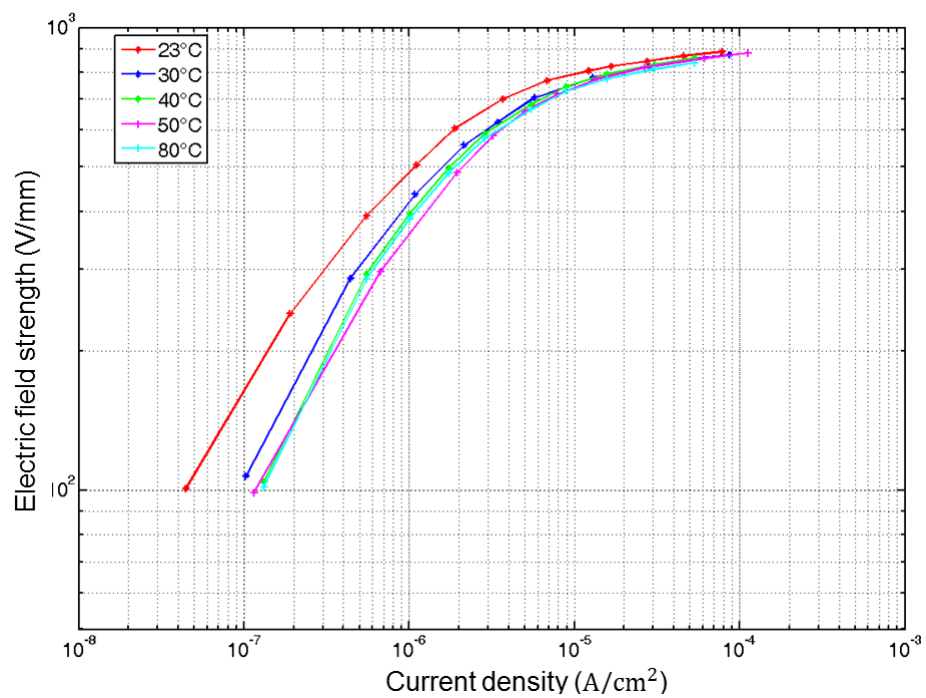
5.3 Computational Investigation

In this section the computational investigation of the application of microvaristor-filled epoxy resin layer in compact bushings is discussed. Further, influences of the switching point, thickness and the length of microvaristor-filled epoxy resin layer on the electric field distribution are investigated.

5.3.1 The Simulated Bushing and Material Properties

The simulated bushing for this compact design is a 550 kV bushing which is almost 4.5 m high and has 94 large and 93 small sheds. The diameter of this bushing is 340 mm. The microvaristor material layer is applied on the outer surface of the GFRP tube, between the GFRP tube and silicone layer. The rotationally symmetric 2D model (rz-geometric) of the simulated bushing is shown in Fig. (5.6). The space between the high-voltage conductor and the GFRP tube is filled with SF_6 gas, which has a much higher dielectric strength than air and hence is usually used as a gaseous dielectric medium.

Figure 5.6: The rotationally symmetric 2D model of the simulated compact bushing. The microvaristor layer is placed between the GFRP tube and silicone layer.
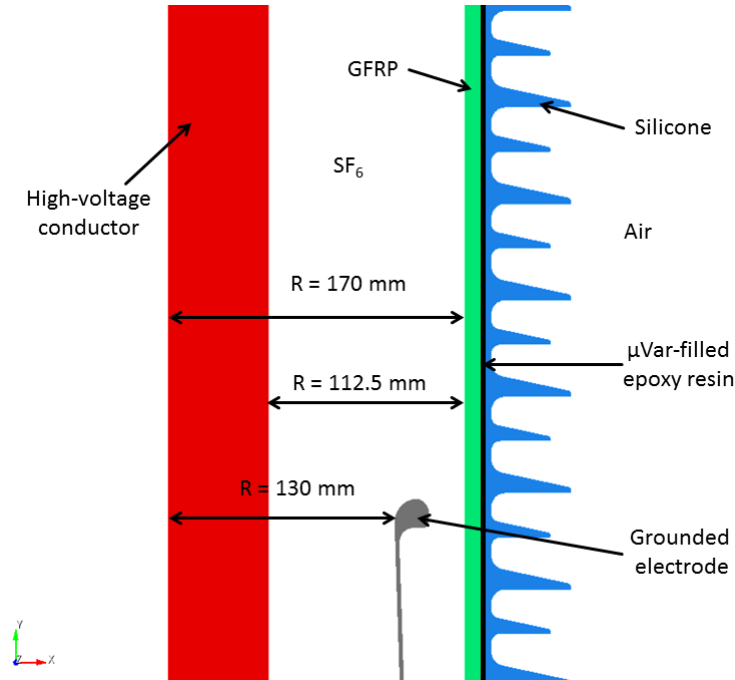
The applied material parameters for FEM simulations are summarized in Table (5.1). The high-voltage conductor and the grounded electrode are modelled as PECs.

Table 5.1: Material parameters for the bushing featuring microvaristor-filled epoxy resin

Material	rel. permittivity ε_r	conductivity κ
Silicone	3.2	0.0
Glass-fibre reinforced plastic	4.0	0.0
Air ambient	1.0	0.0
SF$_6$ gas	1.0	0.0
Water drops	81.0	50 µS/m
Microvaristor-filled epoxy resin	$12.0 \sim 16.0$	non-linear

5.3.2 Choosing the Switching Point of the Microvaristor Composite

As known, the microvaristor-filled composite can produce Joule heat if it becomes conductive, which may lead to thermal breakdown of the material under the permanent operation. Hence, the microvaristor-filled epoxy resin should be insulating under the nominal voltage but becomes conductive if an over-voltage occurs. FEM simulations are carried out to determinate a suitable switching point of the microvaristor-filled composite. As shown in Fig. (5.7), the maximal electric field strength, in the position where the microvaristor layer is planned to be placed, is almost 11.5 kV/cm under the nominal operation voltage of $U_{\text{rms}} = 318$ kV. Hence, the switching point of the microvaristor-filled epoxy resin should be above the nominal electric field strength to avoid thermal instability. On the other hand, the switching point should be less than the critical electric field strength in case of over-voltages to reduce discharge activities. Considering both these aspects the switching point can be e.g. 12 kV/cm.

Simulations are carried out to compare the electric field distributions for the bushings with and without microvaristor-filled epoxy resin under the test over-voltage of $U_{\text{rms}} = 476$ kV. As illustrated in Fig. (5.8), the electric field strength along the surface of the bushing in the air near the grounded electrode can be reduced by almost 30 % at the position where the microvaristor-filled epoxy layer is applied and becomes conductive. This result verifies that the diameter of bushings can be reduced without the increase of the electric field strength in the critical region, namely around the grounded electrode, if the microvaristor-filled epoxy layer is applied.

5.3.3 Reduction of the Water Drop Corona on the Surface of Bushings

Using the microvaristor-filled epoxy resin under the silicone surface in bushings can also dampen the high electric field strength at the triple point of the water droplets, the air and the silicone surface. This can be verified by the computational results shown in

Figure 5.7: The electric field strength distribution in the region, where the microvaristor-filled epoxy resin should be placed, under nominal operation voltage. The results are evaluated at the peak value of the voltage with $U_{\mathrm{peak}} = 449$ kV.
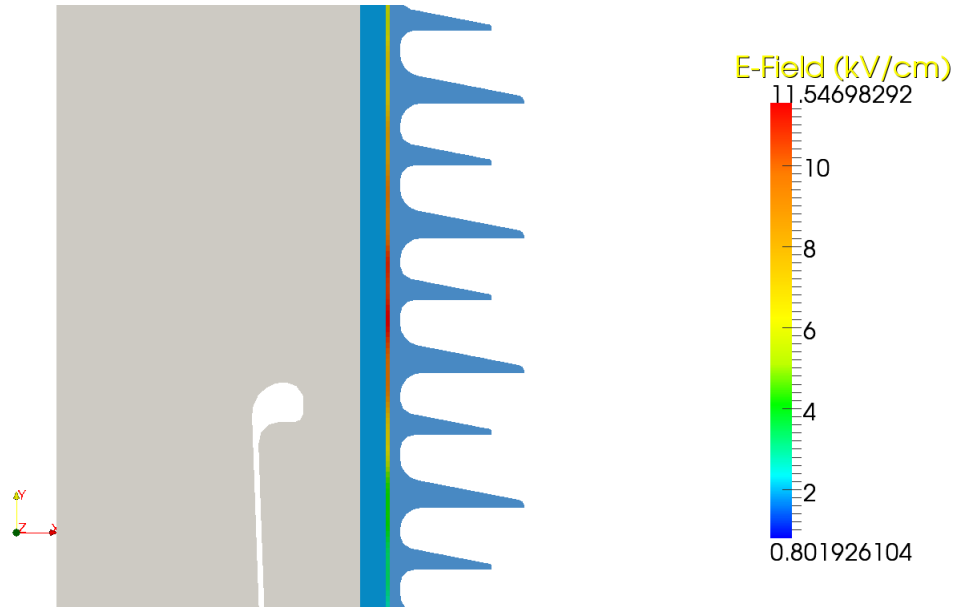
Figure 5.8: The electric field distributions for the bushings with and without microvaristor-filled epoxy layer under the over-voltage. The results are evaluated along the surface of the bushing in the air at the peak value of the voltage $U_{\mathrm{peak}} = 673$ kV.
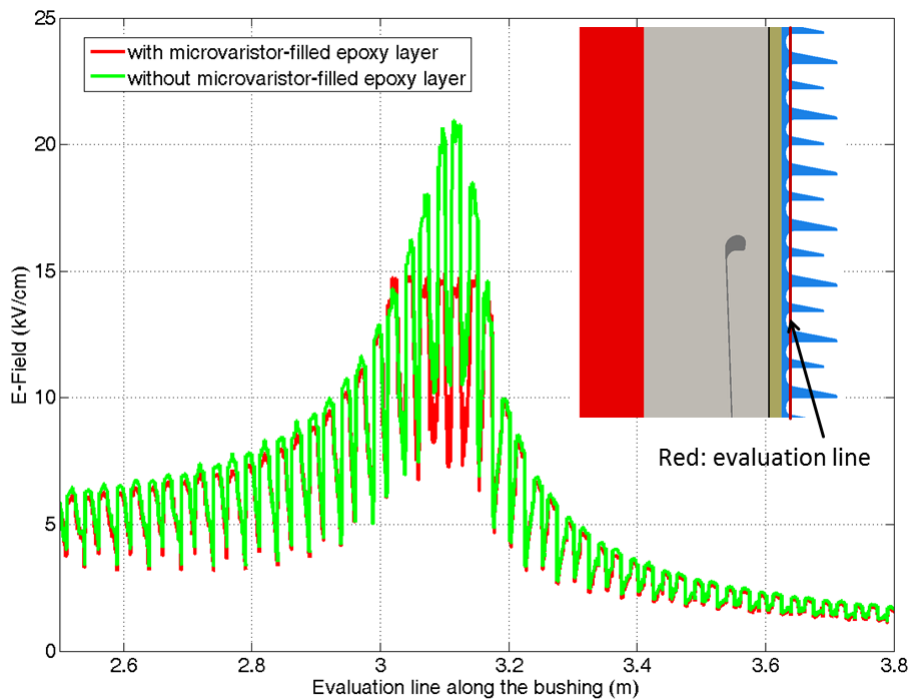
Fig. (5.9). For simulations, just a few water droplets are placed on the surface of the silicone, which are modelled as a hemisphere. The simulation results demonstrate that the high electric field strength at the triple points of the water drop near the grounded electrode can be reduced from almost 28 kV/cm to 18 kV/cm if the microvaristor layer is applied.

Figure 5.9: The electric field distributions for the bushings with a) and without microvaristor-filled epoxy layer b) in the case that a few water droplets are present on the surface of the silicone surface of the bushing.

a) without microvaristor layer   b) with microvaristor layer
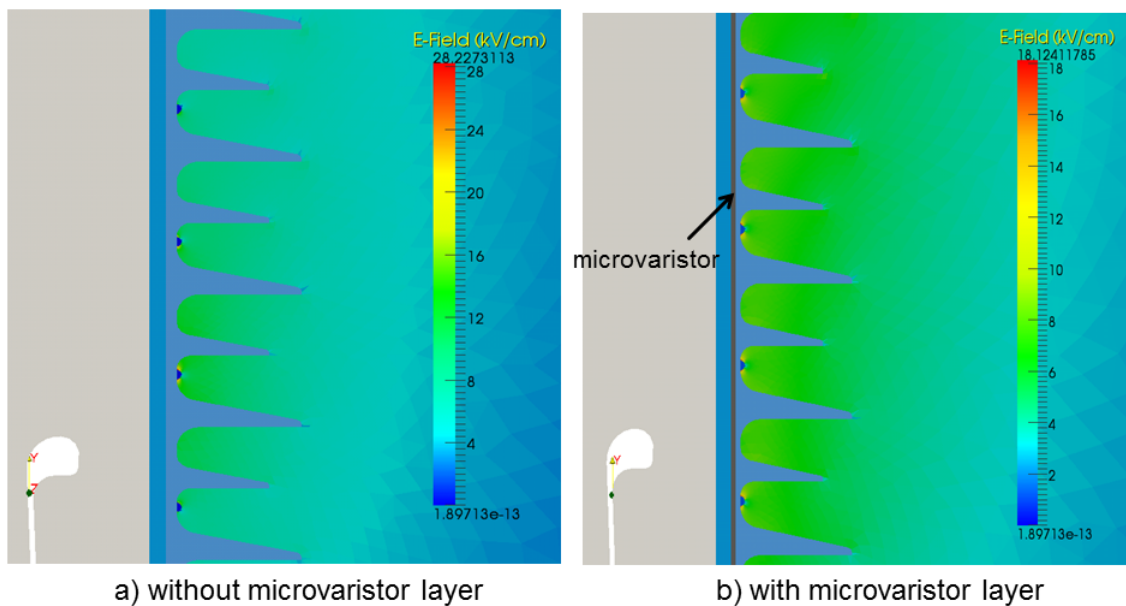
5.3.4 Determination of the Necessary Length of the Microvaristor Layer

In addition to the switching point, the length of the microvaristor-filled epoxy layer is also investigated. Considering the material cost and the industrial application it is not necessary to apply the microvaristor layer along the entire bushing. On the other hand the length should not be too short. Otherwise high electric field strength can appear at the end of the microvaristor layer. In Fig. (5.10) an example is given to show this effect. Simulations with different lengths of microvaristor layer for the same switching point are carried out to determine the necessary length. The applied length should be longer than this necessary length to avoid a local increase of electric field strength at the end of the microvaristor layer.

Also, the switching point has an influence of the necessary length on the microvaristor layer. To investigate this influence simulations for a compact 420 kV bushing featuring

Figure 5.10: An example of the effect that, if the microvaristor layer is too short, the local high electric field strength can appear at the end of the layer.
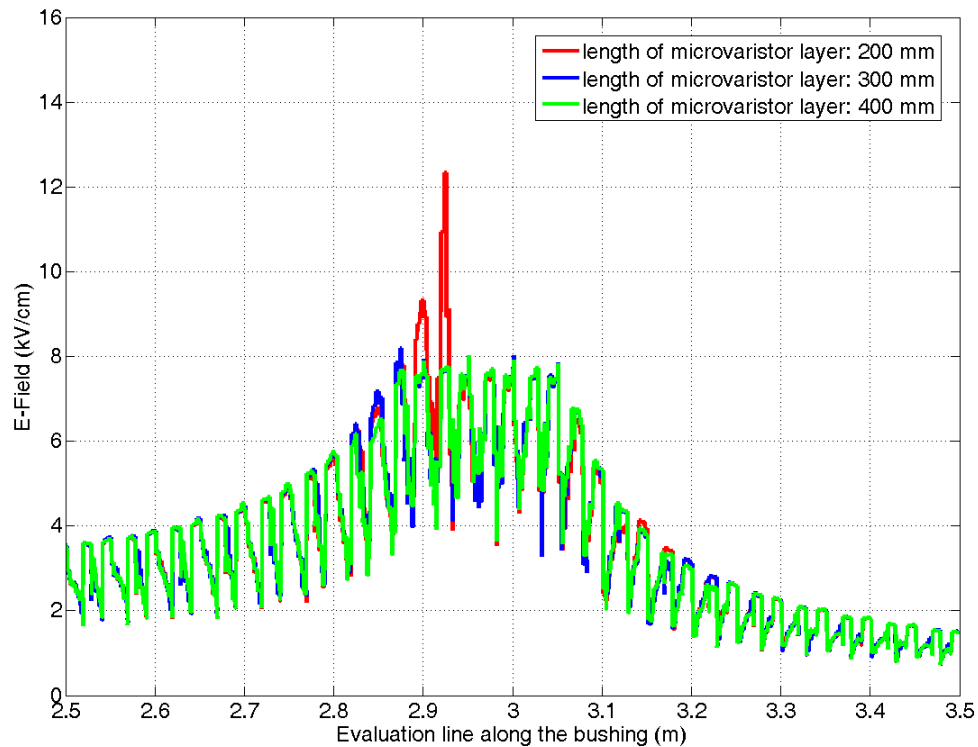
microvaristor-filled epoxy layer with different switching points are carried out. As shown in Fig. (5.11), the necessary length of the layer should be 400 mm, if the microvaristor layer with the switching point at 7.5 kV/cm is applied. Compared to that, the necessary length of the microvaristor layer with the switching point at 6 kV/cm is about 600 mm, as shown in Fig. (5.12). These results indicate that, using the lower switching point of the microvaristor layer, the electric field strength can be better damped. However, for the microvaristor layer with the lower switching point the necessary length is longer.

In addition, the design voltage also affects the necessary length of the microvaristor layer. The higher the design voltage is, the longer the microvaristor layer should be. Hence, for determination of the length of the microvaristor layer, both the chosen switching point and the design voltage should be taken into consideration. Considering both aspects the necessary length of the microvaristor layer for the 550 kV compact bushing can be determined by FEM simulations. The final length is decided by this necessary length plus a safety factor.

5.3.5 Influence of the Thickness of the Microvaristor Layer

To investigate the influence of the thickness of the microvaristor layer on the electric field distribution along the surface of the bushing simulations for the 550 kV compact

Figure 5.11: Determination of the necessary length of the microvaristor layer with the switching point at 7.5 kV/cm for a 420 kV compact bushing.
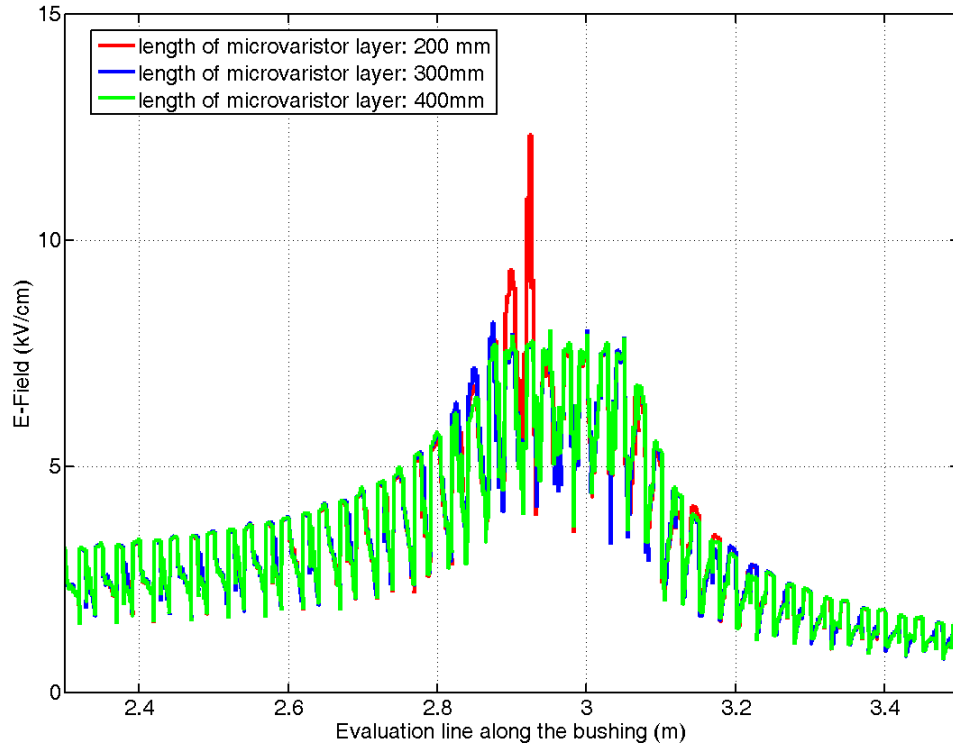
Figure 5.12: Determination of the necessary length of the microvaristor layer with the switching point at 6 kV/cm for a 420 kV compact bushing.
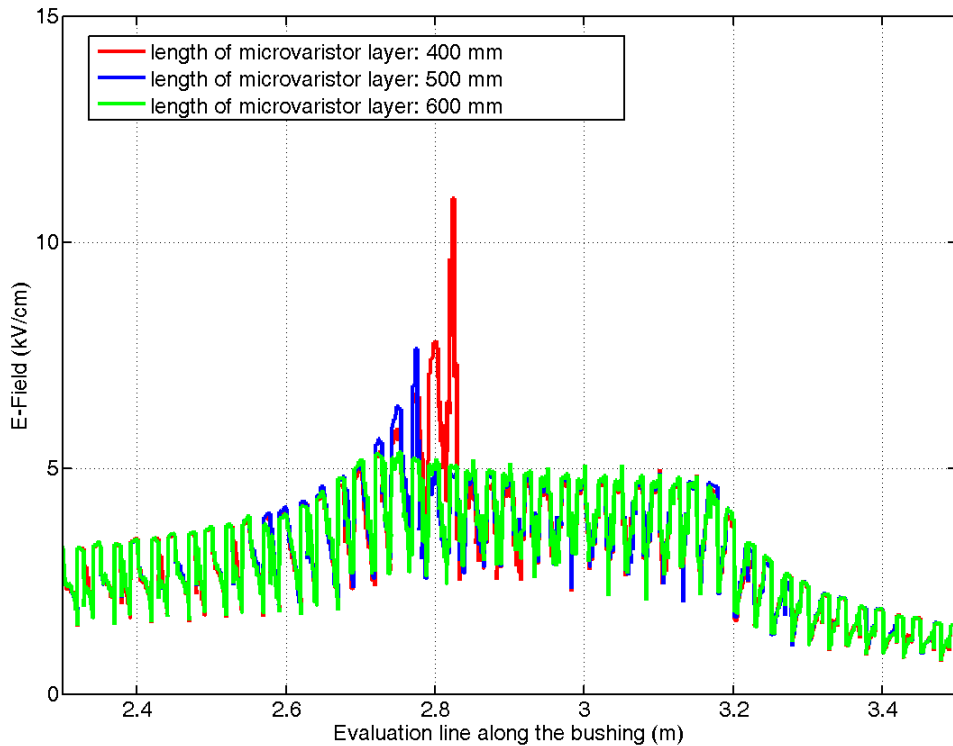
bushing with 600 mm long microvaristor layer with different thickness are carried out. The simulations are performed for the microvaristor layer with the switching point at $12\,\mathrm{kV/cm}$ and under the over-voltage with $U_{\mathrm{rms}} = 476\,\mathrm{kV}$. The results illustrated in Fig. (5.13) show that the thickness of the microvaristor layer has no significant influence on the electric field distribution along the surface of the bushing.

Figure 5.13: Influence of the thickness of a microvaristor-filled epoxy resin layer on the electric field distribution along the surface of bushings. The results are evaluated along the surface of the bushing in the air at the peak value of the voltage $U_{\mathrm{peak}} = 673$ kV.
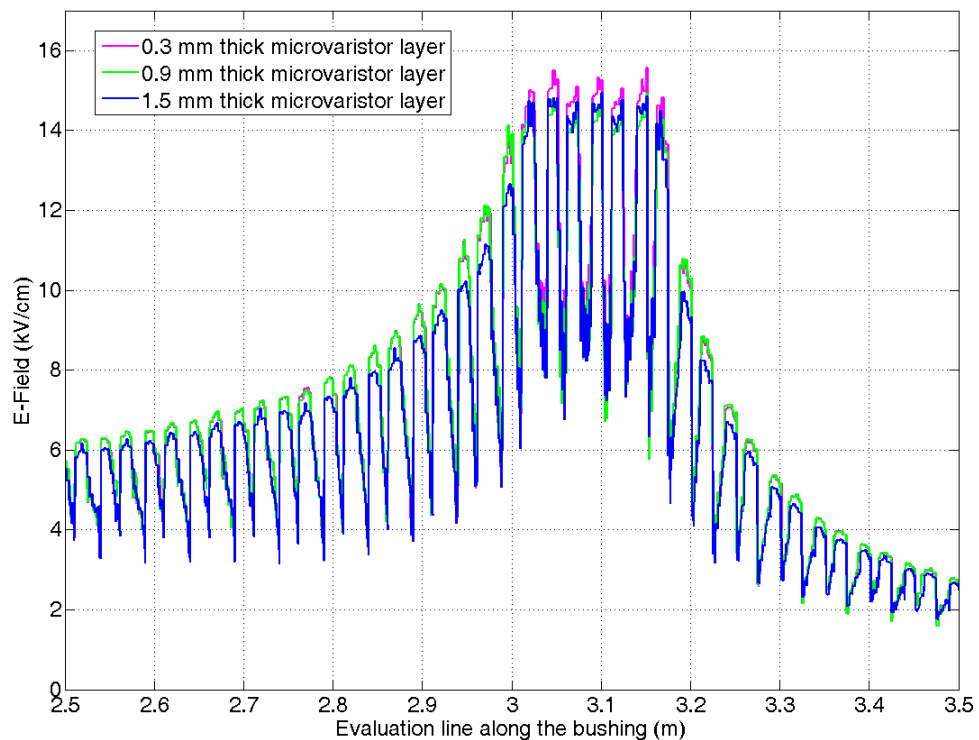
5.4 Experimental Investigation

Prototypes of the compact 550 kV bushing featuring microvaristor-filled epoxy resin are built and experimentally investigated in the high-voltage laboratory of Lapp Insulators GmbH, Wunsiedel. The microvaristor layer is placed onto the GFRP tube near the grounded electrode, as shown in Fig. (5.14). The tested compact bushing and the conventional bushing as comparison are demonstrated in Fig. (5.15).

5.4.1 Partial Discharge Measurements

A partial discharge (PD) measuring system is adopted to measure the partial discharges of bushings, according to the IEC standard 60137 [62]. The applied voltage is slowly raised

Figure 5.14: Microvaristor-filled epoxy resin component placed on the GFRP tube [P4].
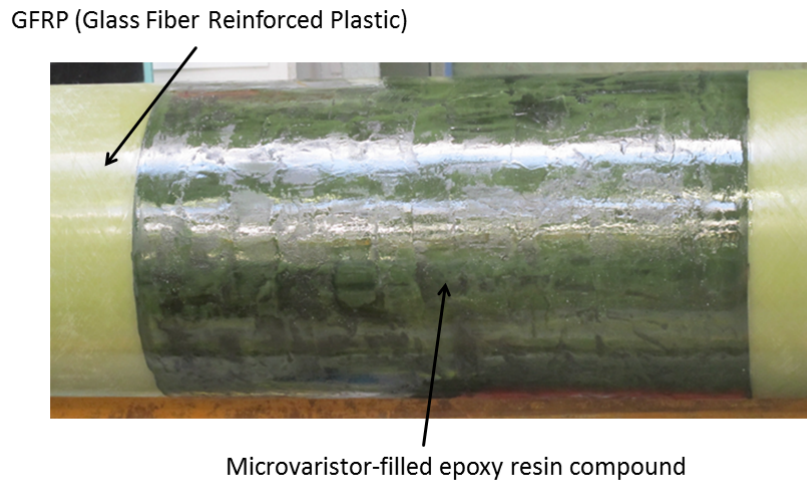
Figure 5.15: Comparison of the 550 kV compact bushing and the conventional bushing in the high-voltage laboratory of Lapp Insulators GmbH [P4].
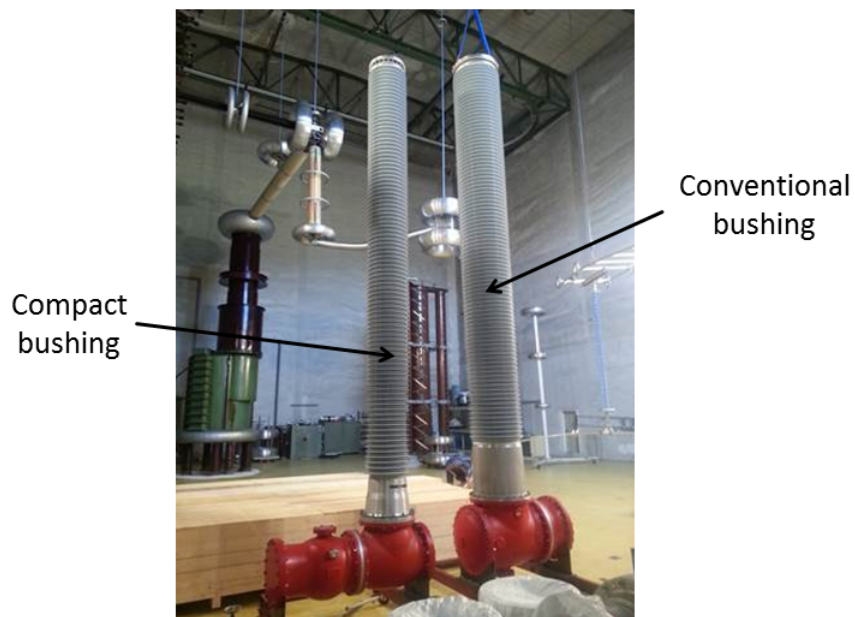
to $U_\text{rms} = 710$ kV, then is kept on this value for a few minutes. After that, the voltage is decreased till zero. In the entire process, the partial discharges are less than 5 pC at an over-voltage of $U_\text{rms} = 476$ kV. These results indicate that no partial discharges occur at the voltage of $U_\text{rms} = 476$ kV. This specification should be fulfilled for designing a bushing[1]. Without the microvaristor component the PD are much higher than 10 pC.

5.4.2 Temperature Measurements

Beside the partial discharges, the temperature on the surface of bushings is also observed. For this observation an infrared camera is adopted. Under normal operation voltage no increase of temperature is detected after 20 minutes. However, if the test over-voltage with $U_\text{rms} = 476$ kV is applied, the temperature increases from 23°C (room temperature) to 30°C after approximate 10 minutes. This result is shown in Fig. (5.16). The increase of the temperature indicates that the microvaristor layer becomes conductive under the over-voltage as desired to reduce the electric field strength in the critical region.

Figure 5.16: Image of temperature increase after 10 minutes, taken by an infrared camera. The indicated position is the position of the microvaristor-filled epoxy resin [P4].
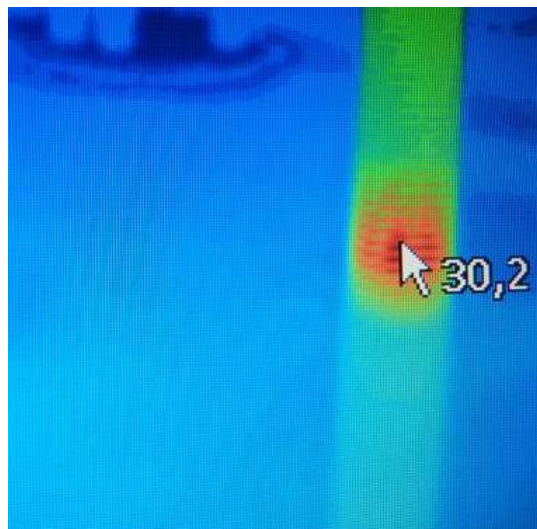
5.5 Summary

In this chapter the application of the microvaristor-filled epoxy resin into the bushings is investigated. The diameter of the compact bushing is smaller than the conventional one leading to an increase of the electric field strength on the surface of the bushing and

---

[1]According to the IEC standard 60137, partial discharges should be less than 10 pC at the voltage of $U_\text{rms} = 476$ kV, for a 550 kV bushing.

consequently to partial discharges at over-voltages. However, the partial discharges should be less than 10 pC at the over-voltage of 476 kV for a 550 kV bushing, according to the IEC standard 60137. To design a compact bushing, which has smaller diameter but still meets the requirements of the standard, the microvaristor-filled epoxy resin layer is applied to the critical region of bushings to reduce the electric field strength if an over-voltage occurs.

Since there is limited research about the electrical properties of the microvaristor-filled epoxy resin, the investigation of this composite is necessary. Hence, samples are produced to investigate the influences of the filler content and temperature on the electrical properties of the composite. Based on the experimental results, the required content of the microvaristor powder is about 75 m% to have an obvious switching transition. Further, the switching point is almost unaffected by the temperature from 23°C to 80°C.

In addition, both non-linear FEM simulations and experiments in the high-voltage laboratory are carried out for the investigation of application of the microvaristor-filled epoxy resin layer in 550 kV compact bushings. Using the FEM simulations, the switching point, the position, the required length and the influence of thickness of this composite layer can be explored at low cost. The prototypes of this compact bushing, which is determined by the FEM simulations, are built and tested in the high-voltage laboratory. Both theoretical and experimental results demonstrate that the application of the microvaristor-filled epoxy resin layer can effectively reduce the peak electric field strength in the critical region in the air near the grounded electrode, consequently avoiding the occurrence of partial discharges.

6 Optimization of HV Devices Using an Adaptive Kriging Method

6.1 Introduction

In order to reduce the electric field strength in high-voltage (HV) devices diverse field grading measurements are adopted for the design of a HV device. To get the maximal field grading effect, some geometrical and material parameters can be optimized. Optimization of complex design problems for large scale HV devices usually involve extensive use of simulation based design and analysis tools, such as finite element analysis and other computationally intensive models [10][114]. Since the high-voltage devices are usually very large-scale and non-rotationally symmetric, the 3D accurate simulations usually require a long time to evaluate a specific design. In this case, surrogate models are appropriate to approximate the real-world model [25]. These allow to optimize very time-consuming large-scale problems. These would be almost impossible to optimize using the standard optimization methods without surrogate models. For an accurate optimization, a surrogate model with a good quality is required. The quality of surrogate model usually depends on:

- the topography of function being approximated.

- the type of approximation technique.

- the sampling strategy.

- number of sample points available for approximation.

- locations of sample points.

One of the most popular surrogate models is the Kriging model [74]. In this chapter the use of an adaptive Kriging surrogate modelling for time efficient optimization of large-scale high-voltage devices is discussed. Since these are time-consuming design problems, a new problem specific adaptation of an so-called adaptive one-then-two stage Kriging method [55] is proposed and tested. The described algorithm uses space-filling LHS (Latin Hypercubes Sampling) and a one-stage approach, which is also called goal seeking, to get the initial sample points to build the first surrogate model. Then a two-stage approach using

the weighted expected improvement function is adopted to get further infill points. This reduces the total number of computationally very expensive 3D simulations for the evaluation of given parameter sets and hence speeds up the optimization process. This algorithm is implemented using Python and tested with a few analytical test functions and a realistic corona ring design problem for outdoor insulators. The results are also compared to an other global algorithm without surrogate model, the DIRECT (DIViding RECTangles) algorithm [65]. The content of this chapter is mainly based on [P3][P6].

6.2 Mathematical Background of the Kriging Method

One of the most popular methods to build a surrogate model of computationally expensive deterministic simulations is the Kriging method [77]. This is because this method can not only predict the shape of the expensive objective function based only on limited sample points, but also estimate the accuracy of this prediction. The following mathematical formulations are based on [39][65][68].

Suppose a set of sample data $\mathbf{X} = (\mathbf{x}^1, \mathbf{x}^2, \cdots, \mathbf{x^n})$ with observed responses $\mathbf{y} = (y^1, y^2, \cdots, y^n)$ is given. The basic idea of the Kriging method is that the observed responses are viewed as if they were from a stochastic process [68]. For the Kriging meta-modelling a response value of the objective function is globally estimated by a known polynomial p and a random derivation Z from this polynomial:

$$y(\mathbf{x}) = p(\mathbf{x}) + Z(\mathbf{x}) \, , \tag{6.1}$$

where $Z(\mathbf{x})$ is assumed to be a realization of a random process with a mean of μ and variance of σ^2. The correlation of these random variables with each other is given by

$$\mathrm{cor}[Z(\mathbf{x}^i), Z(\mathbf{x}^j)] = \exp\left(-\sum_{l=1}^{d} \theta_l |x_l^i - x_l^j|^{p_l}\right), \tag{6.2}$$

where d is the dimension of the variables, θ_l determines how fast the correlation drops off as one moves in the lth coordinate direction, and p_l determines the smoothness of the function in the lth coordinate direction [65]. Then the $n \times n$ correlation matrix of the observed data

$$\mathbf{R} = \begin{pmatrix} \mathrm{cor}[Z(\mathbf{x}^1), Z(\mathbf{x}^1)] & \cdots & \mathrm{cor}[Z(\mathbf{x}^1), Z(\mathbf{x}^n)] \\ \vdots & \ddots & \vdots \\ \mathrm{cor}[Z(\mathbf{x}^n), Z(\mathbf{x}^1)] & \cdots & \mathrm{cor}[Z(\mathbf{x}^n), Z(\mathbf{x}^n)] \end{pmatrix} \tag{6.3}$$

and a covariance matrix

$$\mathrm{Cov}(Z, Z) = \sigma^2 \mathbf{R} \tag{6.4}$$

can be obtained. The distribution of Z depends on the parameters μ, σ^2, θ_l and p_l ($l = 1, \cdots, d$). To estimate the value of those parameters, the likelihood of the observed data should be maximized. The likelihood function[1] can be written as

$$\mathrm{L}(\boldsymbol{\theta}, \mathbf{p}) = \frac{1}{(2\pi)^{\frac{n}{2}} (\sigma^2)^{\frac{n}{2}} |\mathbf{R}|^{\frac{1}{2}}} \exp\left[-\frac{(\mathbf{y} - \mathbf{1}\mu)' \mathbf{R}^{-1} (\mathbf{y} - \mathbf{1}\mu)}{2\sigma^2} \right] , \qquad (6.5)$$

where $\mathbf{1}$ is the $n \times 1$ vector with all elements equal to one. Eqn. (6.5) can be simplified using the natural logarithm and further take derivatives, then the concentrated log-likelihood function is obtained:

$$\mathrm{ConLL}(\boldsymbol{\theta}, \mathbf{p}) = -\frac{n}{2}\log(\widehat{\sigma}^2) - \frac{n}{2}\log(|\mathbf{R}|) . \qquad (6.6)$$

Further the optimal values of $\widehat{\sigma}^2$ and $\widehat{\mu}$ can be expressed as function of $\mathbf{R}$:

$$\widehat{\sigma}^2 = \frac{(\mathbf{y} - \mathbf{1}\widehat{\mu})' \mathbf{R}^{-1} (\mathbf{y} - \mathbf{1}\widehat{u})}{n} , \qquad (6.7)$$

$$\widehat{\mu} = \frac{\mathbf{1}' \mathbf{R}^{-1} \mathbf{y}}{\mathbf{1}' \mathbf{R}^{-1} \mathbf{1}} . \qquad (6.8)$$

The concentrated log-likelihood function depends only on $\mathbf{R}$ and consequently only on the correlation parameters θ_l and p_l ($l = 1, \cdots, d$). By maximizing the concentrated log-likelihood function the optimal value of the correlation parameters are estimated. The prediction $\widehat{y}(\mathbf{x}^*)$ of the objective function $y(\mathbf{x}^*)$ at an unobserved point $\mathbf{x}^*$ is given by

$$\widehat{y}(\mathbf{x}^*) = \widehat{\mu} + \mathbf{r} \mathbf{R}^{-1} (\mathbf{y} - \mathbf{1}\widehat{\mu}) , \qquad (6.9)$$

where $\mathbf{r}$ is the correlation of the point $\mathbf{x}^*$ to the other observed points $\mathbf{X}$. The mean square error (MSE) of the predictor at the point $\mathbf{x}^*$ can be now written as

$$s^2(\mathbf{x}^*) = \widehat{\sigma}^2 \left(1 - \mathbf{r}' \mathbf{R} \mathbf{r} + \frac{(1 - \mathbf{r}' \mathbf{R} \mathbf{r})^2}{\mathbf{1}' \mathbf{R}^{-1} \mathbf{1}} \right) . \qquad (6.10)$$

For convenience the root mean square error (RMSE), $s(\mathbf{x}^*) = \sqrt{s^2(\mathbf{x}^*)}$, is used to represent the predicted deviation of the Kriging model from the actual response. Obviously the RMSE equals zero, if $\mathbf{x}^*$ equals to any of the observed points.

As demonstrated in Fig. (6.1), using four sample points the Kriging surrogate model has a bad approximation of the true function (left), whilst the surrogate model is well fitted using eight sample points (right). Intuitively the question arises how many and where the points should be sampled to assemble a well-fitted Kriging surrogate model. The different

---

[1]A likelihood function yields the probability of given observations in dependence of model parameters.

strategies to generate the sample points will be introduced in the next section: initial and infill sampling.

Figure 6.1: Comparison of two Kriging surrogate models using different sample points.
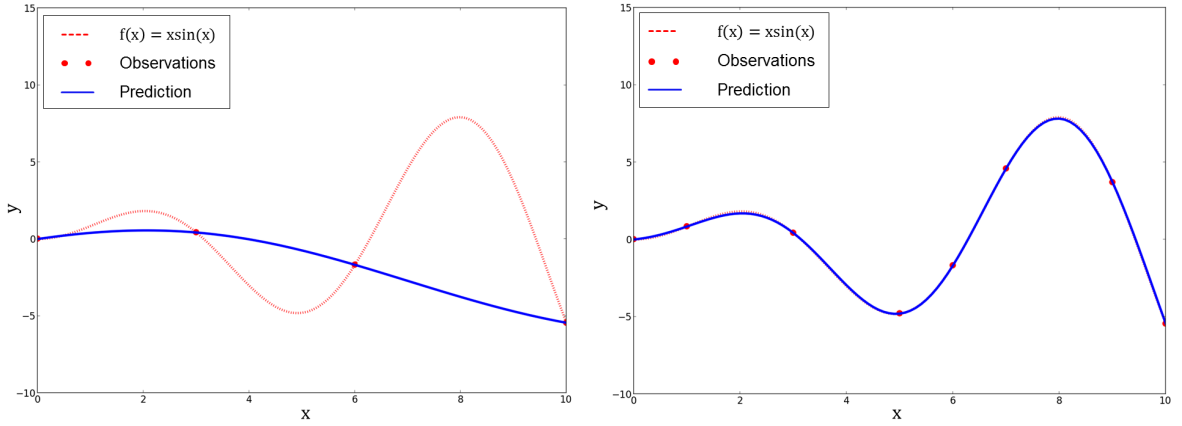
6.3 Initial and Infill Sampling

6.3.1 Initial Sampling

To generate a surrogate model using the Kriging method, a set of the initial sample points, at which the expensive objective function is evaluated, is required and can be generated by the experimental design [98]. However, because the shapes of the functions are usually unknown and the problems to be solved are viewed as black box, it is most important to get the space-filling initial points to avoid getting information from just a certain part of the design domain [83]. Latin Hypercube Sampling (LHS) [115] is one of the popular choices to accomplish that. However, a random generated LHS does not guarantee that the samples are space-filling. Therefore, a so-called maximin LHS is adopted in which the maximin metric, introduced by [64] and further extended in [88], is used to evaluate the space-fillingness of a sampling plan.

Let $d_1, d_2, \cdots, d_m$ be the set of the unique values of distances between all possible pairs of points in a sampling plan $\mathbf{X}$, which are sorted in ascending order. $N_i, i \in \{1, 2, \cdots, m\}$, defines the number of pairs of points in $\mathbf{X}$ separated by the distance d_j. The most widely used definition of distance is the p-norm of the space:

$$d_p\left(\mathbf{x}^{(i_1)}, \mathbf{x}^{(i_2)}\right) = \left(\sum_{j=1}^{k} |x_j^{(i_1)} - x_j^{(i_2)}|^p\right)^{1/p} \tag{6.11}$$

If $p = 1$, this is the rectangular distance, which also referred to as the Manhattan norm,

while $p = 2$ yields the Euclidean norm. In this work, the Euclidean distance is adopted. An LHD is called maximin when the separation distance min $d(\mathbf{x}^{(i_1)}, \mathbf{x}^{(i_2)})(i_1 \neq i_2)$ is maximal among all LHDs of given size n [59]. Morris and Mitchell [88] also define a scalar valued criterion to rank competing sampling plans, which is defined as follow:

$$\Phi_q = \left(\sum_{j=1}^{m} N_j d_j^{-q} \right)^{1/q}. \tag{6.12}$$

The smaller the value of Φ_q, the better the space-filling property will be. By choosing the value for the parameter q, Morris and Mitchell recommend minimizing Φ_q for $q = 1, 2, 5, 10, 20, 50, 100$ and then choosing the best of the resulting plans according to actual value of Eqn. (6.12). When using Φ_q as a criterion to assess the quality of a Latin hypercube sampling plan, a systematic means of optimizing this metric across the space the Latin hypercubes is still required. In this work an algorithm based on evolutionary operation (EVOP) [39] is adopted to determine an optimized Latin hypercube sampling plan. The entire process of generating an optimized LHS plan can be summarized as follows:

1: A random generated hypercube as a starting point for the optimization process.

2: For each $q \in \{1, 2, 5, 10, 20, 50, 100\}$ optimize Φ_q using EVOP:

    – 2.1: In each generation the parent is mutated randomly for a number of times.

    – 2.2: The sampling plan which yields the smallest Φ_q value among all offspring and the parent is selected as the parent for the next generation.

    – 2.3: Repeat the step 2.2 until the maximal number of generations is reached.

3: Choose the best sampling plan from the optimized sampling plans with different values of q.

In Fig. (6.2) sampling plans with ten points using random LHS (left) and maximin LHS (right) are demonstrated. This figure shows that the sampling plan using maximin LHS is more uniformly distributed in the whole domain than the sampling plan using random LHS.

6.3.2 Infill Sampling

Since the surrogate model $\widehat{f}$ is just an approximation of the true objective function f which should be optimized, it is necessary to improve the accuracy of the surrogate model using further informations (infill points) in addition to the initial sample points [39]. There are diverse strategies, which are categorized into two-stage and one-stage varieties in [65], to choose these infill points.

Figure 6.2: The comparison of a sampling plan using random LHS and using maximin LHS.
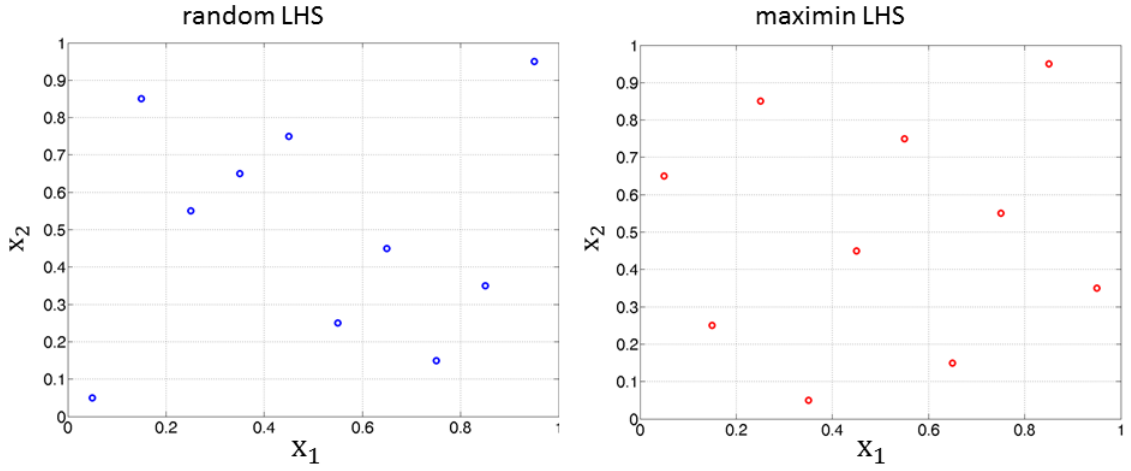
Two-Stage Approach

For the two-stage approach a Kriging model is at first constructed by the current sample points, and the next point to be sampled is found by optimizing an auxiliary function based on this Kriging model. One popular utility function is the expected improvement utility function [68] which is based on the RMSE predicted by the current Kriging model. A parameter w can be added to the expected improvement function for better control of the balance between searching globally in highly uncertain regions (explorative) and search locally around the current minimum (exploitive) [113]. This modified function is called weighted expected improvement utility function (WEIF) and can be expressed as

$$\text{WEIF}(\mathbf{x}) = \begin{cases} s(\mathbf{x})\left[wu(\mathbf{x})\Psi(u(\mathbf{x})) + (1-w)\phi(u(\mathbf{x}))\right], & s(\mathbf{x}) > 0 \\ 0, & s(\mathbf{x}) = 0 \end{cases} \tag{6.13}$$

with

$$u(\mathbf{x}) = \frac{y_{min} - \widehat{y}(\mathbf{x})}{s(\mathbf{x})} , \tag{6.14}$$

where $y_{\min}$ is the current minimum of the objective function values of the sample points, $\widehat{y}(\mathbf{x})$ is the Kriging prediction at the point $\mathbf{x}$ given by Eqn. (6.9), $s(\mathbf{x})$ is the root mean square error in the prediction, and $\Psi(u(\mathbf{x}))$ and $\phi(u(\mathbf{x}))$ are the normal cumulative distribution function and density distribution function, respectively. The value of the adjustable parameter w is between 0 and 1 and controls the balance of the two terms of the Eqn. (6.13). If $w = 0$, the left term vanishes and all emphasis is placed on searching exploratively, whilst $w = 1$ places all emphasis on searching exploitively, as illustrated in Fig. (6.3). However, the research in [132] demonstrates that the choice of the optimal w is very important and unfortunately it is problem dependent. Therefore, in this work a

simple schema $w = |\sin(\pi/18 \cdot i)|$, where i is the iteration number, is adopted to vary w between 0 and 1, so that some iterations are searching globally while some iterations are searching locally.

Figure 6.3: The weighted improvement function values with the different values w.
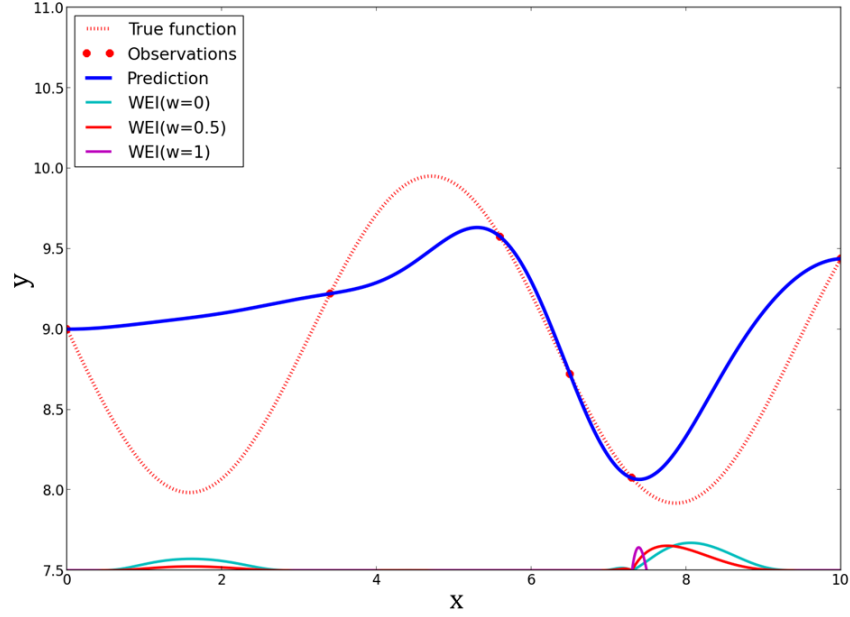
A main drawback of a two-stage method is the possibility of deception [65], because the evaluation of the WEIF strongly relies on the root mean square error of the Kriging predictor. If the initial sample is too sparse, it may give a highly misleading view of the objective function, consequently leading to a bad choice of the next sample point. An extreme case of this deception is shown in Fig. (6.4). To get over this problem the one-stage approach is adopted, which is introduced in the next section.

One-Stage Approach

The main difference between the one-stage and the two-stage approach is that the one-stage approach does not need any information from the Kriging model, which is constructed by the current n observed points [65]. In the one-stage approach a hypothesis is made about a new point $\mathbf{x}^*$ that achieves the goal objective function value f^*. Under this assumption a new surrogate model can be constructed based on the n observed points and the conditional hypothetical point $(\mathbf{x}^*, f^*)$. The corresponding conditional likelihood can be written as

$$\mathrm{CL}(\boldsymbol{\theta}, \mathbf{p}, \mathbf{x}^*) = \frac{1}{(2\pi)^{\frac{n}{2}}(\sigma^2)^{\frac{n}{2}}|\mathbf{C}^{\frac{1}{2}}|}\exp\left[-\frac{(\overline{\mathbf{y}} - \overline{\mathbf{r}}\mu)'\mathbf{C}^{-1}(\overline{\mathbf{y}} - \overline{\mathbf{r}}\mu)}{2\sigma^2}\right] , \qquad (6.15)$$

Figure 6.4: An extremely deceptive function [65]. The Kriging model fitted to those sample points has the root mean square error $s(\mathbf{x}) = 0$ everywhere, therefore the WEIF values are also equal to zero everywhere.
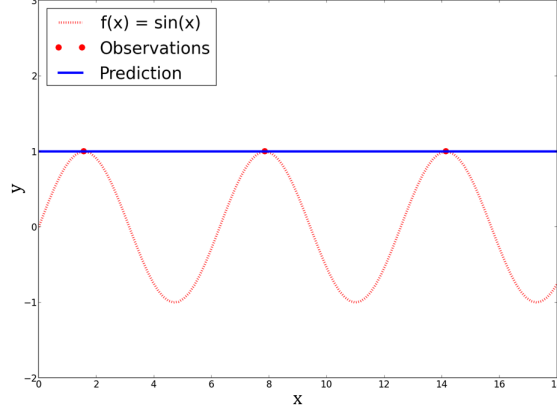
where

$$\mathbf{C} = \mathbf{R} - \mathbf{r}\mathbf{r}', \quad \overline{\mathbf{y}} = \mathbf{y} - \mathbf{r} \cdot f^*, \quad \overline{\mathbf{r}} = \mathbf{1} - \mathbf{r} .$$

Here $\mathbf{R}$ is the correlation matrix of the n sample points, which depends on the parameters $\boldsymbol{\theta}$ and $\mathbf{p}$. The vector $\mathbf{r}$ describes the correlation between $\mathbf{x}^*$ and n sample points. In this case the matrix $\mathbf{C}$ is affected by three parameters: $\boldsymbol{\theta}$, $\mathbf{p}$ and $\mathbf{x}^*$. The Eqn. (6.15) can be simplified using the natural logarithm to get the conditional log-likelihood function:

$$\mathrm{CLL}(\boldsymbol{\theta}, \mathbf{p}, \mathbf{x}^*) = -\frac{n}{2}\log(\widehat{\sigma}^2) - \frac{n}{2}\log\left(|\mathbf{C}|\right) - \frac{(\overline{\mathbf{y}} - \overline{\mathbf{r}}\mu)'\mathbf{C}^{-1}(\overline{\mathbf{y}} - \overline{\mathbf{r}}\mu)}{2\sigma^2} . \tag{6.16}$$

By taking the derivatives of the Eqn. (6.16) with respect to μ and σ^2 and solving them equal to zero, the following equations can be obtained:

$$\widehat{\mu} = \frac{(\overline{\mathbf{r}}'\mathbf{C}^{-1}\overline{\mathbf{y}})}{(\overline{\mathbf{r}}'\mathbf{C}^{-1}\overline{\mathbf{r}})} \tag{6.17}$$

and

$$\widehat{\sigma}^2 = \frac{(\overline{\mathbf{y}} - \overline{\mathbf{r}}\widehat{\mu})\mathbf{C}^{-1}(\overline{\mathbf{y}} - \overline{\mathbf{r}}\mu)}{n} . \tag{6.18}$$

The concentracted form of the conditional log-likelihood function can then be obtained by substituting Eqn. (6.17) and Eqn. (6.18) back into Eqn. (6.16):

$$\mathrm{ConCLL}(\boldsymbol{\theta}, \mathbf{p}, \mathbf{x}^*) = -\frac{n}{2}\log(\widehat{\sigma}^2) - \frac{n}{2}\log\left(|\mathbf{C}|\right) . \tag{6.19}$$

The next sample point $\mathbf{x}^*$ is estimated by maximizing Eqn. (6.19). This approach can avoid the problem of deception, from which the two-stage approach is suffering.

However, the one-stage approach has its own drawbacks: a) the choice of target values

f^* is crucial for the performance of the one-stage approach, which is reported in [50], but the choice of this value can be difficult; b) the one-stage approach becomes more computationally expensive than the two-stage approach, especially for high dimensional problems. If the optimal function value f^{opt} or an appropriate goal is known, the target value f^* can be set to them. However, in practice the optimum is usually not available or the goal is not clear. In this case, one solution is that several search points using several values of $f^* < y_{\min}$ ($y_{\min}$ is the current minimum of the objective function values of the sample points) are computed in a single iteration as suggested in [65].

6.4 One-then-Two-Stage Algorithm

To overcome the drawbacks of the two-stage approach and one-stage approach a hybrid one-then-two-stage Kriging model assisted algorithm is adopted [55], which mainly consists of three parts: initialization of sample points, one-stage selection of points and two-stage selection of points. The procedure of this optimization algorithm is shown in Fig. (6.5).

Figure 6.5: Procedure of the hybrid one-then-two-stage Kriging model assisted algorithm.
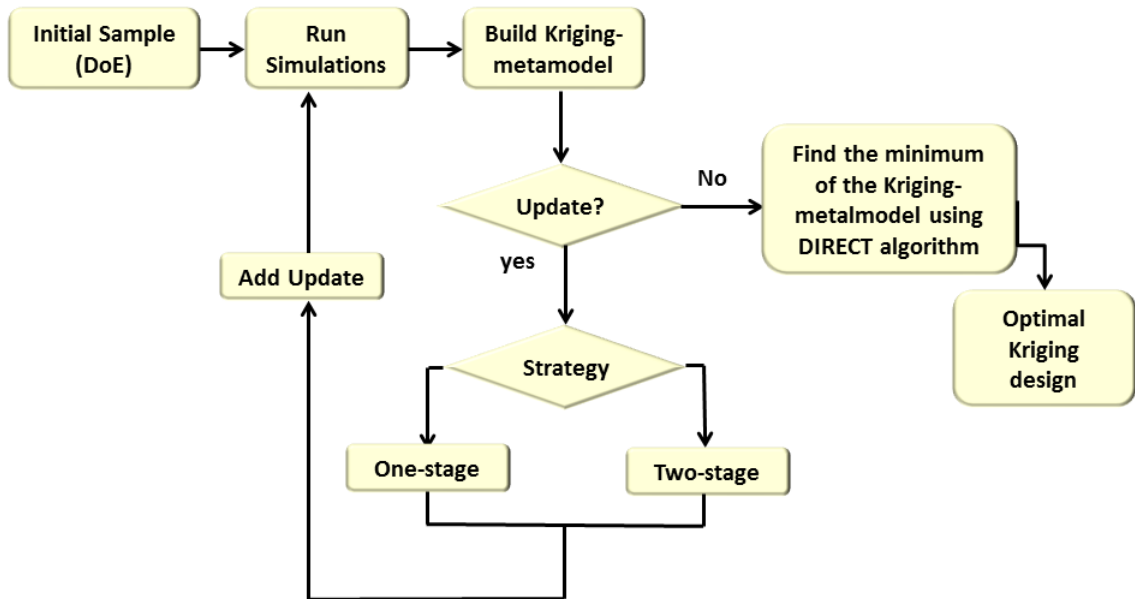
Step 1: Initialization of Sample Points

In this step a small amount of initial sample points is generated using the maximin LHS. Then the objective function values are evaluated on those points. On one hand, to reduce unnecessary evaluations, the number of the points to generate should not be too large. On

the other hand, the number should not be too small to avoid too low accuracy. In this work $4d$ points (d: dimensions of the problem) are sampled at the beginning.

Step 2: One-Stage Selection of Points

In this step further points are chosen using the information of the 4d initial sample points and the one-stage strategy. Since the Kriging response surface could be too inaccurate with such a little amount of sample points, the use of the two-stage approach in such an early stage may be unsuitable. The process of using a one-stage approach to find the next infill point is repeated until $10d$ (d: dimensions of the problem) points are obtained, which is suggested in [68], or the optimum is found (if the optimum value is known or the expected improvement of the design product is archived).

Step 3: Two-Stage Selection of Points

If $10d$ observed points are available and the optimum is still not found in the previous step, the two-stage approach is adopted to get further infill points. Choosing a suitable stop criterion to determine when to stop the surrogate infill process is rather subjective [39]. In this work, when the expected improvement is lower than one percentage of the range of the objective function values, the surrogate infill process is stopped.

Estimating the optimal infill sample points $\mathbf{x}^*$ in step 2 and step 3, and the system parameters $\boldsymbol{\theta}$ and $\mathbf{p}$ are optimization problems themselves. To solve those problems a robust global optimization algorithm - the DIRECT method is adopted, which is introduced in the next section.

6.5 DIRECT Optimization Method

DIRECT (DIviding RECTangles) method is an optimization algorithm developed by Donald R. Jones et al. [67] to find the global minimum of a multi-variate function subject to simple bounds. This algorithm yields a deterministic and unique solution, using no derivative information. The DIRECT method is a modification of the standard Lipschitzian approach which eliminates the need to specify a Lipschitz constant [6]. One of the major problems of Lipschitzian optimization is specifying the Lipschitz constant [67]. Mathematically, the Lipschitz constant K satisfies the relation

$$|f(x_1) - f(x_2)| \leq K||x_1 - x_2||, x_1, x_2 \in \mathbb{R} \tag{6.20}$$

where $f(x)$ is the objective function for the optimization problem. The Lipschitz constant K is considered as a weighting parameter to place the emphasis on global or local search.

In standard Lipschitzan methods, K is usually large, because it must equal or exceed the maximum rate of change of the objective function. As a result, these methods place a high emphasis on global search which leads to slow convergence [67]. In DIRECT algorithm this problem can be solved by carrying out simultaneous searches using all possible constants from zero to infinity. Thus, the algorithm searches both locally and globally, leading to a great speed-up of the convergence.

An essential idea of the DIRECT algorithm is the subdivision of the entire design space into hyper-rectangles of equal length for multidimensional problems [110]. Then the objective functions are only evaluated in the middle of the hyper-rectangles. This is advantageous, because this method can be easily extended to higher dimensions without increasing the number of objective function evaluations for each hyper-rectangle. Subsequently, for each iteration the set of hyper-rectangles is selected and further subdivided, which are most likely to achieve the lowest objective function. This is repeated until the termination criterion is met.

An illustration of an one-dimensional optimization by the DIRECT algorithm is shown in Fig. (6.6). At first, the center of the design space is sampled and the space is subdivided into two domains. During the next iteration the centers of the sub-domains are sampled and the objective functions are evaluated at these sampled points. The domains with the lower objective function value are further subdivided and the center points of the new sub-domains are sampled. This process is iterated until the termination criterion is reached.

This process can be easily extended to higher dimensional-problems. The main difference in higher dimensions compared to one-dimensional problems is the division of the search space. Fig. (6.7) illustrates the optimization using DIRECT algorithm in two dimensions. The process can be summarized by the following steps:

1) Choose the center of the design space as the starting point.

2) Subdivide the rectangle into three rectangles along the longest side.

3) Evaluate the objective function values of the centers of new rectangles.

4) Identify the set of potentially optimal rectangles to be further subdivided.

5) Go back to step 2) until the maximum number of function evaluations is reached or the termination criterion has been met.

More information about the DIRECT algorithm can be found in [66][67].

Figure 6.6: Example of one-dimensional optimization using the DIRECT algorithm [110].
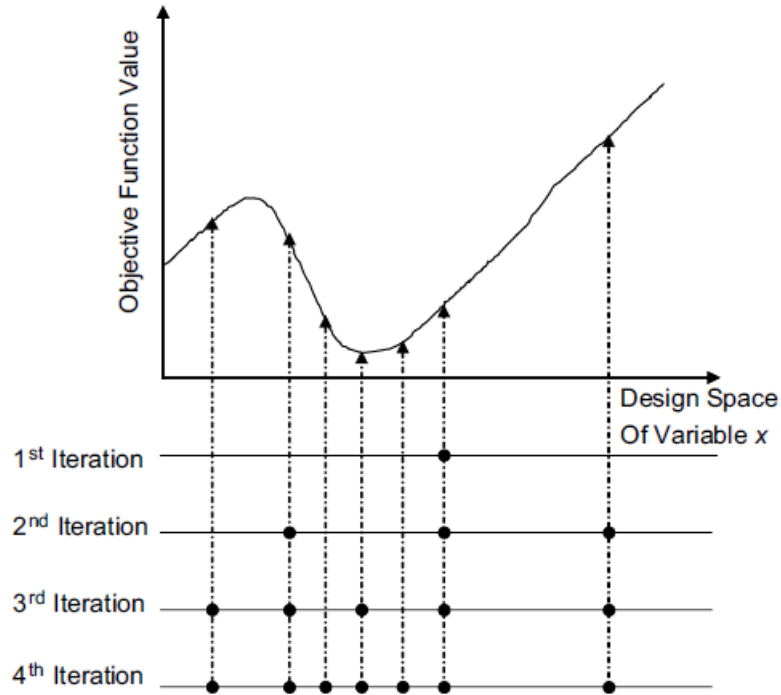
6.6 Analytical Results using One-then-Two Stage Kriging

The proposed algorithm is tested with a few benchmark test functions, which are defined as box-bounded unconstrained problems. The simple descriptions of these test functions are given in Table (6.1). In the colume Domain, the lower and upper bounds for all variables are shown. More information about those test functions can be found in [85]. Three variants of the algorithms are tested using the test functions in Table (6.1):

1. One-then-two approach with the target value f^* set to the global optimum (suppose the global optimum of the function value is known in advance, just the position of the optimum should be evaluated) in the one-stage approach.

2. One-then-two approach with the target value $f^* < y_{\min}$ in the one-stage approach, where $y_{\min}$ is the current minimum of the sample points.

3. Plain two-stage approach with $w = |\sin(\pi/18 \cdot i)|$, where i is the iteration number.

All tests terminate after a first global optimum is found. The initial sample points for these three variants are generated using the maximin LHS. The results are shown in Table (6.2). This method is efficient to locate the global minimum for most of the functional test problems. The only case where the one-then-two approach is not able to find the global optimum is a very complicated 2D Schwefel function [85], which is designed

Figure 6.7: Example of two-dimensional optimization using the DIRECT algorithm and dividing hyper-rectangles [40].
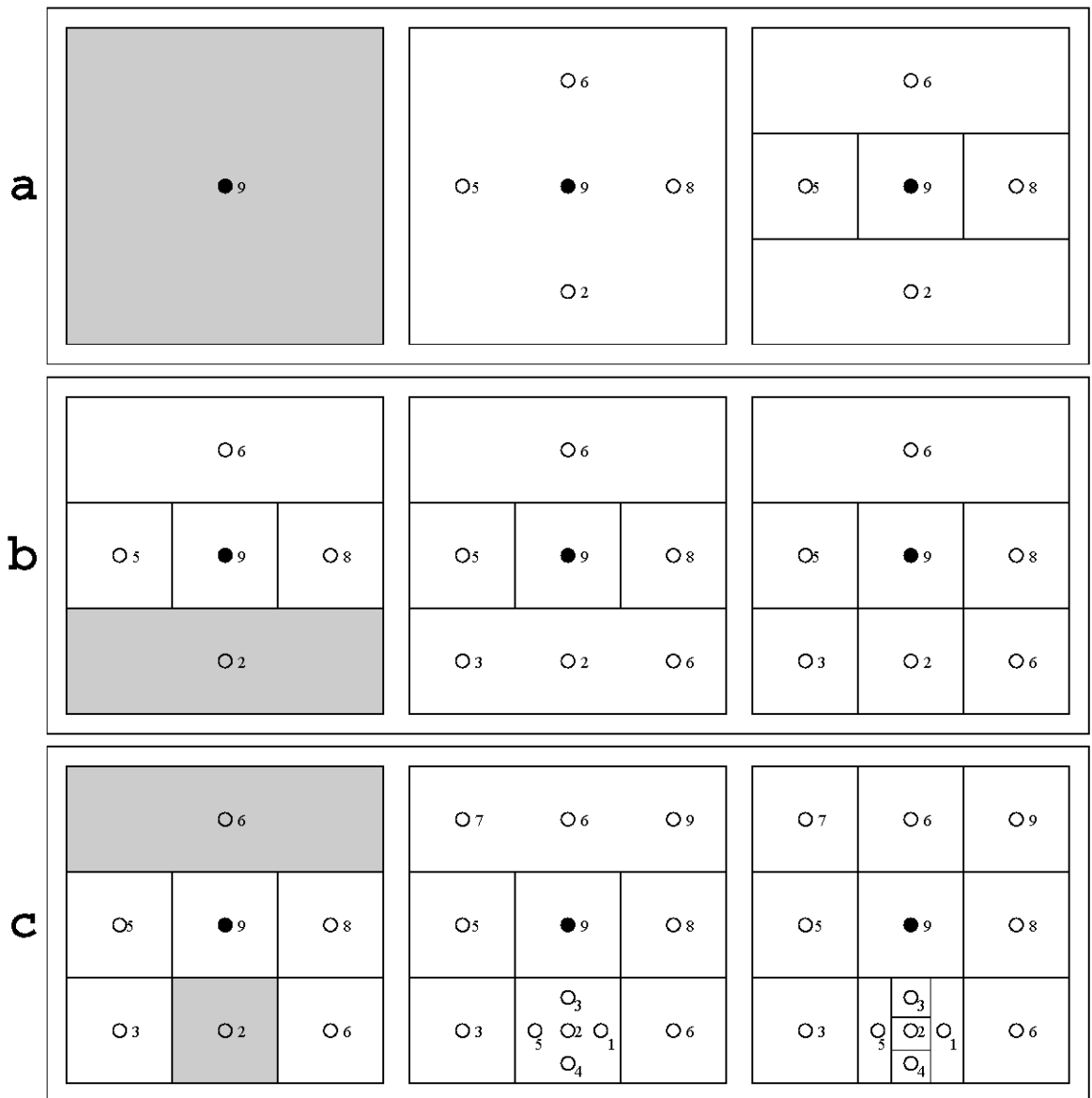
Table 6.1: The box-bounded unconstrained test functions [85]

Function Name	Dimensions	Domain
Humps	1	[-5, 5]
Schwefel 1D	1	[-500, 500]
De Jong's Function	2	[-5.12, -5.12] - [5.12, 5.12]
Branin	2	[-5, 0] - [10, 15]
Six-Hump Camel	2	[-3, -2] - [3, 2]
Rosenbrocks valley	2	[-2.048, -2.048] - [2.048, 2.048]
Michalewiczs function 2	2	$[0, 0]$ - $[\pi, \pi]$
Schwefel 2D	2	[-500, -500] - [500, 500]

Table 6.2: Number of evaluations to get within 1% of the optimal value

Function	One-then-two (optimum is known)	One-then-two (optimum is unknown)	Two-stage
Humps	13	15	fails
Schwefel 1D	13	16	fails
De Jong's Function	10	13	11
Branin	18	24	16
Six-Hump Camel	26	33	fails
Rosenbrock's valley	22	22	18
Michalewiczs function	16	19	fails
Schwefel 2D	fails	fails	fails

to be an especially hard objective function for global optimization. In comparison, the algorithm using plainly the two-stage approach is not sufficient for many problems. Besides, the one-then-two stage algorithm is faster, if the optimal function value is known for the target value f^*. As examples the optimization processes of the one-dimensional Schwefel's function and Hump's function are demonstrated.

6.6.1 Schwefel's Function

Schwefel's function is deceptive in that the global minimum is geometrically distant over the parameter space from the next best local minima. Therefore, the optimization algorithms are potentially prone to convergence in the wrong direction [97]. The one-dimensional Schwefel's function is defined as:

$$f(x) = -x \cdot \sin\left(\sqrt{|x|}\right), x \in [-500, 500]. \tag{6.21}$$

This function has a global minimum located in $(420.9687, -418, 9892)$ and four local minima. The results using the Kriging assisted algorithm with the one-then-two approach are shown in Fig. (6.8). Four initial sample points (red points) are generated by LHS sampling algorithm. Then the one-then-two approach is performed to further sample the infill points (blue points). After a total of 13 points are sampled, the global minimum of the objective function is found. As comparison, the algorithm using the plainly two-stage approach is also adopted to optimize the Schwerfel's function. This algorithm stops, when a local minimum is found.

6.6.2 Hump's Function

The Hump's function is a multi-modal test function which has two local minimums, where the global minimum has a small area relative to the search space. The function is defined as follows:

$$f(x) = 6 - \frac{1}{(x - 0.3)^2 + 0.01} - \frac{1}{(x - 0.9)^2 + 0.04}, x \in [-5, 5]. \tag{6.22}$$

The global minimum of this function is located in $(0.299, -96.500)$. Both one-then-two stage and plainly two-stage Kriging assisted algorithms are adopted to search the global minimum. The results are illustrated in Fig. (6.10) and Fig. (6.11). After 13 sample points, the global minimum is located using the one-then-two stage Kriging assisted algorithm, while just the local minimum is found using the two-stage algorithm.

Figure 6.8: Optimization process of the 1D Schwefel's function using the one-then-stage Kriging assisted algorithm.
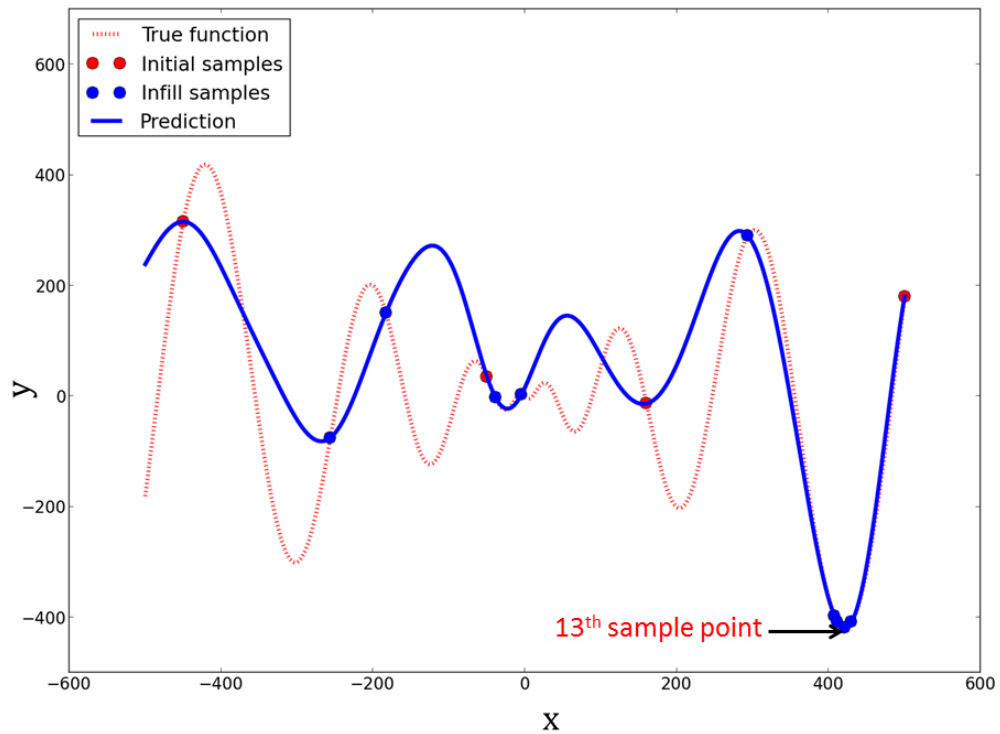
Figure 6.9: Optimization process of the 1D Schwefel's function using the plainly two-stage Kriging assisted algorithm.
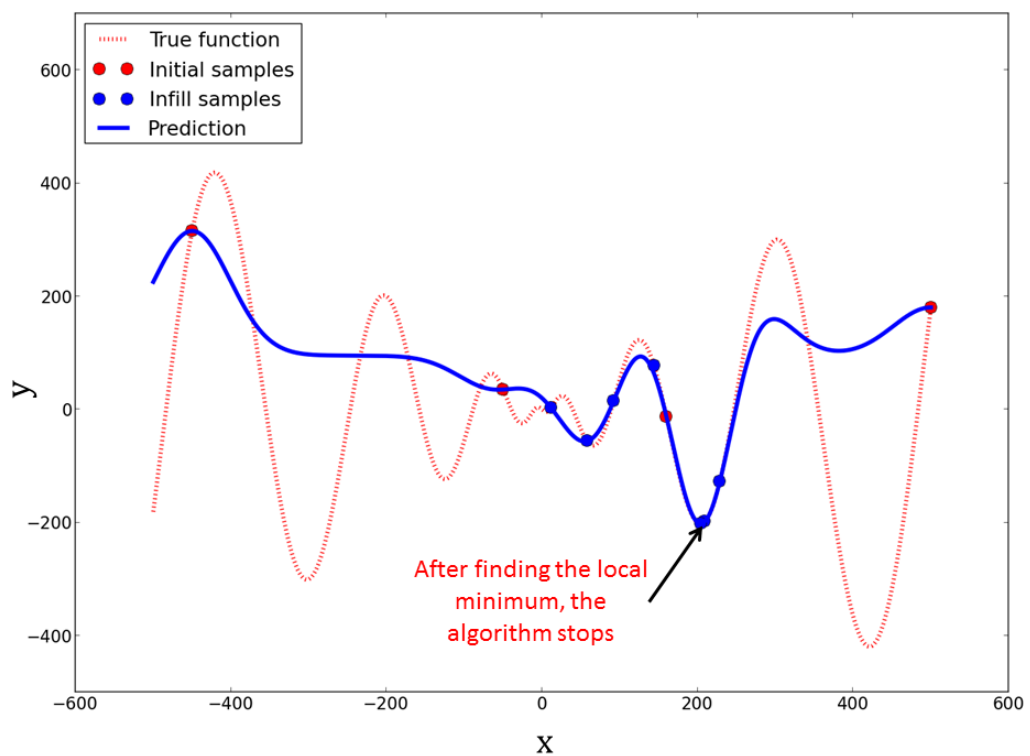
Figure 6.10: Optimization process of the Hump's function using the one-then-two-stage Kriging assisted algorithm.
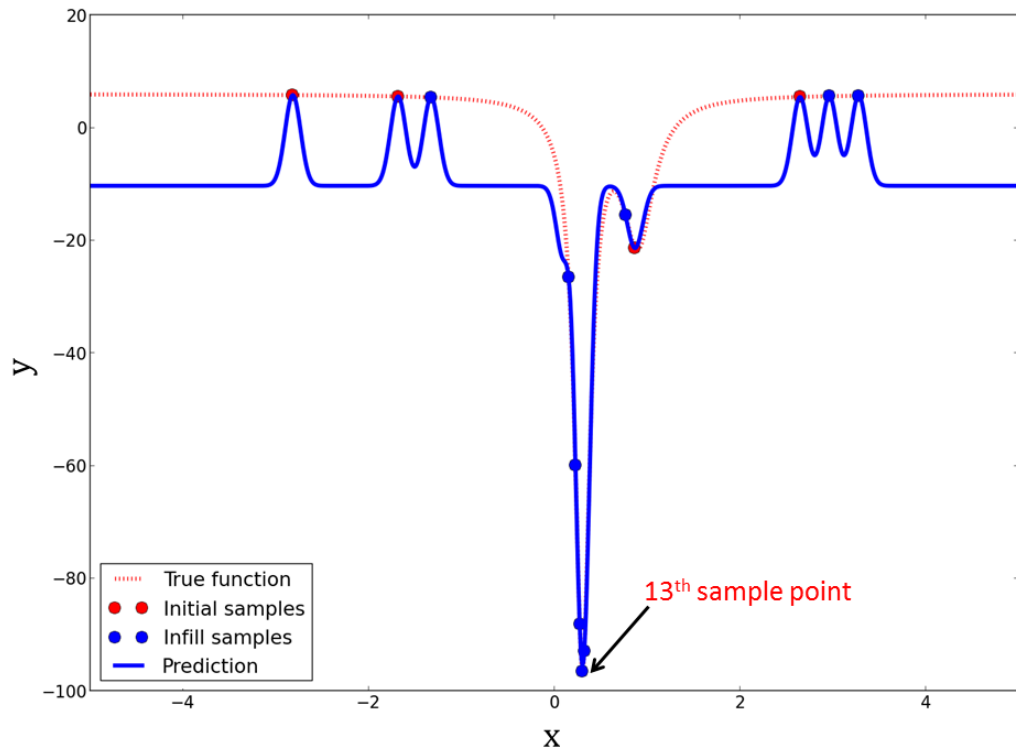
Figure 6.11: Optimization process of the Hump's function using the plainly two-stage Kriging assisted algorithm.
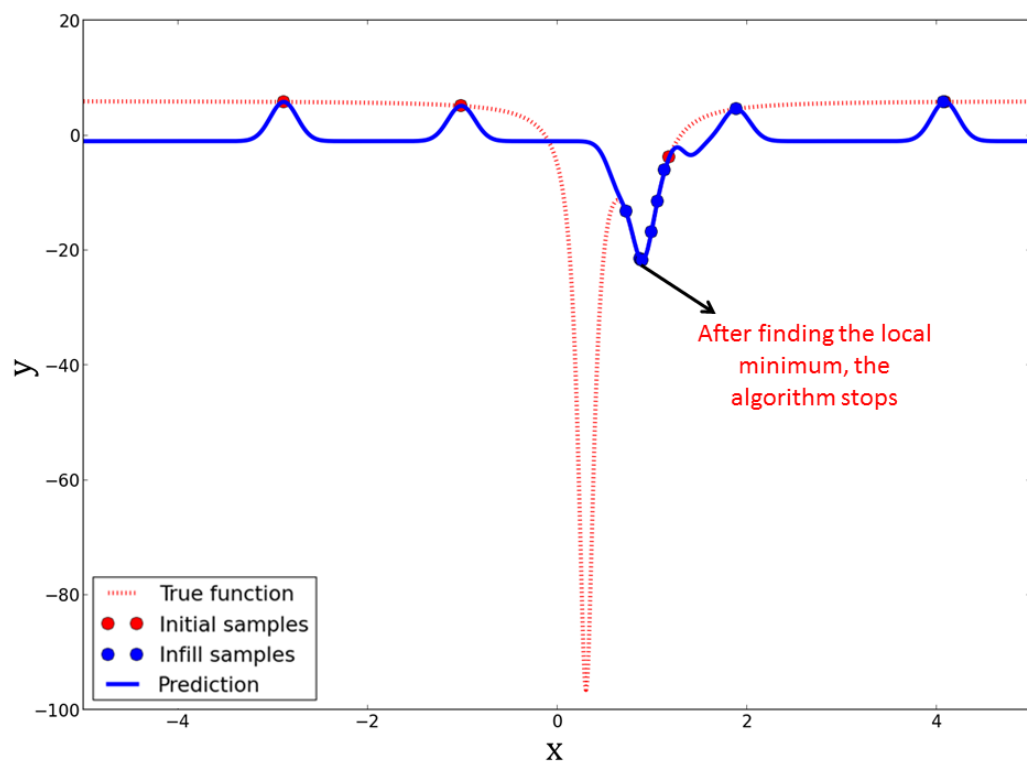
6.7 Optimization of the HV Corona Ring

6.7.1 The Use of Corona Rings for Insulators

There are diverse measures to reduce the electric field strength along the surface of insulators [72]. An option is to use a corona ring at the grounded and energized end fittings of the insulator, which locally reduce the electric field strength in critical areas [105]. Fig. (6.12) shows the field grading effect of installing a corona ring at the energized end of a 250 kV composite insulator. The corona ring should be correctly positioned to get the maximal field grading effect. In this section three geometrical parameters, shown in Fig. (6.13) are considered in an optimization procedure: the major ring radius R_{major}, the radius of the ring tube R_{minor} and the distance between the corona ring and the energized end fitting d.

Figure 6.12: Electric field distribution along the surface of the insulator with and without the corona ring.
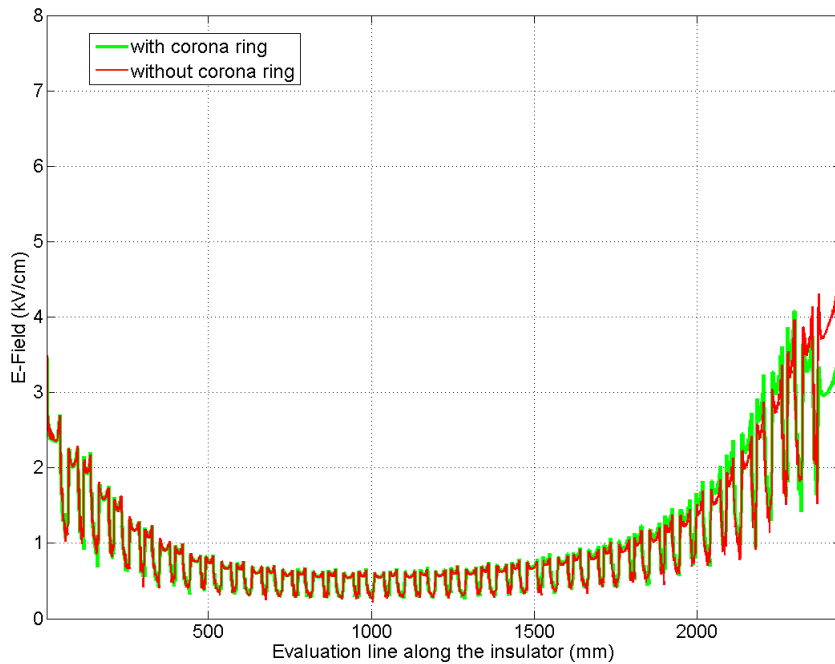
The 3D FEM simulation code MEQSICO is used to accurately calculate electric field distributions along the insulator for various corona ring design parameters. 250 kV high-voltage is applied to the transmission line and the corona ring at the energized end fitting of the insulator. For the dry surface condition of the insulator the electrostatic simulations are carried out. These 3D simulations of large-scale high resolution insulator models that realistically take into account coupling capacitances are very time-consuming. Performing such a 3D simulation takes from almost one hour to a few hours, depending on the complexity and the accuracy of the mesh of the simulation model. Hence, the number of simulation runs should be limited.

Figure 6.13: Three geometrical parameters on the corona ring to optimize.
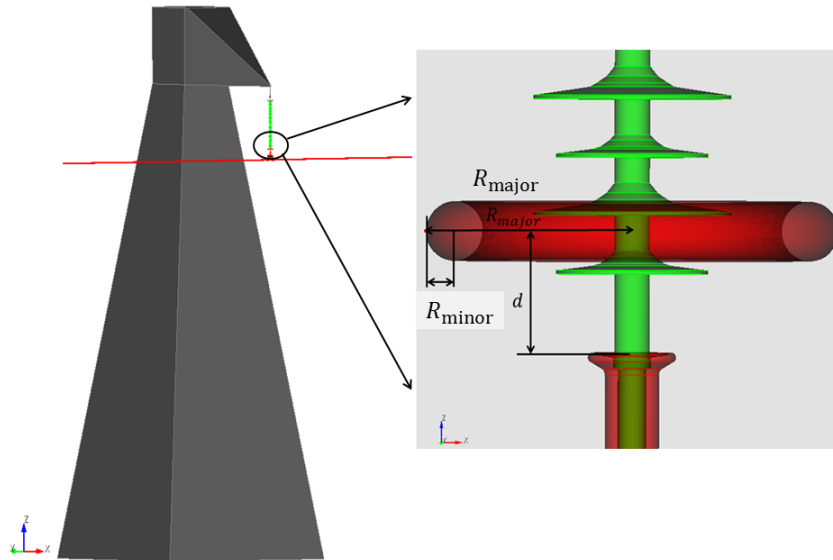
6.7.2 Optimization Results for the Corona Ring Design Problem

The optimization algorithm was applied to the corona ring design problem. The aim of this problem is to find the optimal geometrical parameters of a corona ring so that the electric field at the energized end of the insulator is reduced as much as possible. The three parameters R_{major}, R_{minor} and d are optimized in the calculation domain [170 mm, 250 mm] x [20 mm, 50 mm] x [0 mm, 200 mm]. The software CUBIT is used to generate the mesh for the simulated models. The simulation software MEQSICO is adopted to numerically calculate the electric field distribution along the surface of the long-rod insulator. A script programmed in Python is used as the central control of the entire optimization process. The schematic process of the optimization is shown in Fig. (6.14). The results using the one-then-two stage Kriging algorithm are also compared to the results using the DIRECT optimization algorithm (see Table (6.3)). For comparable results the one-two-stage Kriging algorithm just needs 39 simulations, whilst 157 simulations are required for the DIRECT algorithm. Hence, the optimization process is speeded up with a factor of almost 4. Using the optimal geometrical parameters of the corona ring, the electric field at the energized end fitting is quite well reduced, as shown in Fig. (6.15).

6.8 Summary

In this chapter an adaptive Kriging model-assisted algorithm using one-then-two stage infill strategies is presented, which combines the advantages of the one-stage approach and the two-stage approach. This proposed algorithm is reimplemented using Python and

Figure 6.14: Optimization process using different components and a python script as the main control.
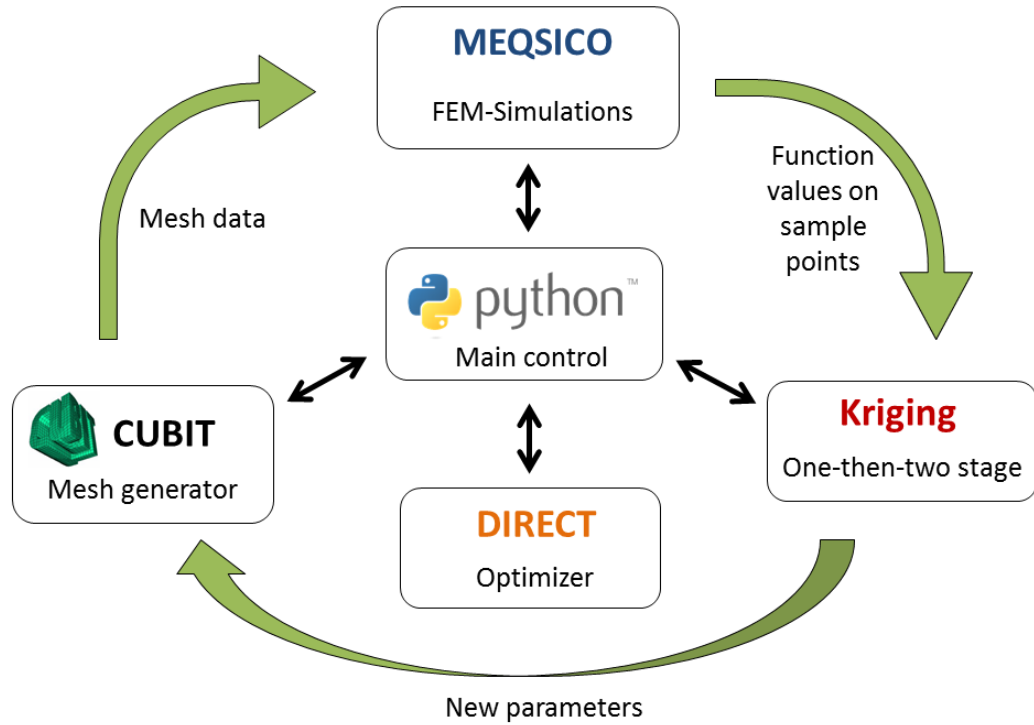
Figure 6.15: Electric field distribution along the insulator with the optimal corona ring.
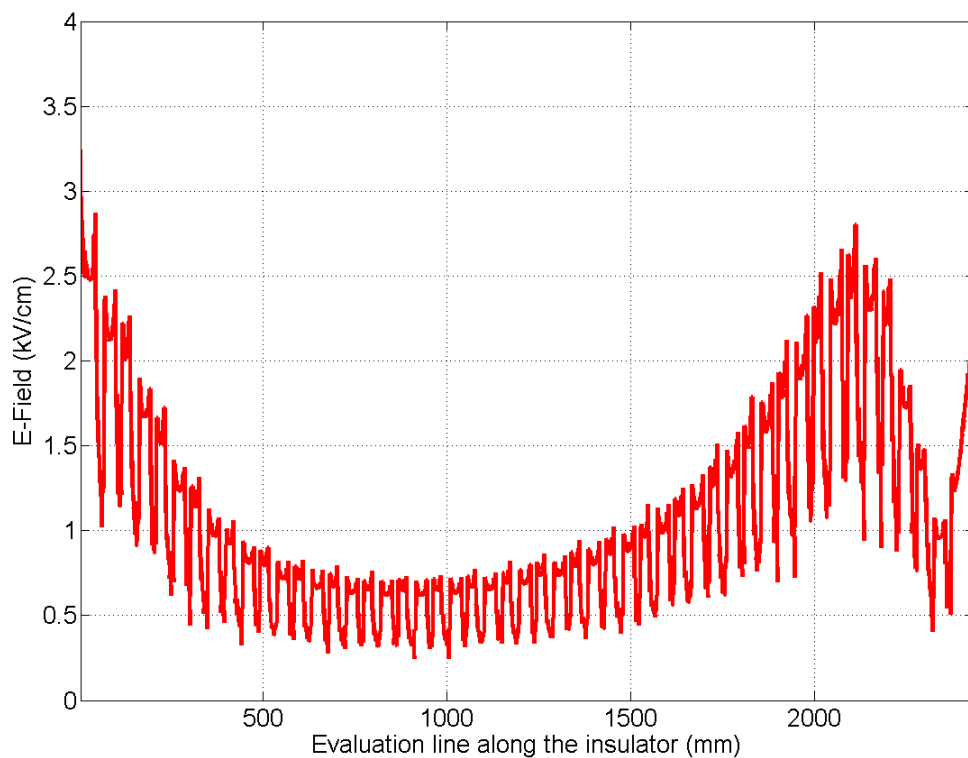
Table 6.3: Results of the corona ring optimization using the one-then-two stage approach Kriging and the DIRECT algorithms

Methods	No. of simulations	d (mm)	R_{minor} (mm)	R_{major} (mm)	E_{opt} (kV/cm)
Kriging (One-then-two stage)	**39**	108.33	49	248.26	2.84
DIRECT	**157**	107.41	48.33	248.52	2.82

successfully tested with some analytical functions. This method is efficient for locating the global minimum for most of the functional test problems. Furthermore, the test for the real world application also yields a good speed-up in the corona ring design optimization process with an acceptable accuracy.

7 Optimization of Large-Scale HV Devices Using the Co-Kriging Method

7.1 Introduction

To evaluate the electric field distribution along the HV devices, electro-static simulations are carried out for the devices with linear materials, whilst electro-quasistatic simulations are carried out for the devices featuring the non-linear field grading material. Due to the high number of degrees of freedom of non-rotationally symmetric discrete 3D FEM models and highly non-linear material characteristics, the computational design and optimization of HV devices is very time consuming. Thus, in real-world applications involving the design of HV devices the number of runs of expensive accurate 3D simulations should be limited.

In chapter 6 an optimization algorithm using the one-then-two stage Kriging method is adopted to optimize the geometrical parameters of the corona ring for insulators. This algorithm shows a rather good speed-up and it still yields reliable results. However, for problems which require a few days to run a simulation, i.e., non-linear electro-quasistatic 3D simulations, the number of runs of expensive FEM simulations should be further limited, but the ordinary Kriging method using just few coarse sample points usually results in an inaccurate approximation. Hence, in this chapter the Co-Kriging method is adopted, which combines the information of the slow but accurate 3D simulations (high level) and extensively, reduced fast but crude 2D simulations (low level). Using this algorithm makes it possible to optimize large-scale HV devices within a reasonable time and with sufficient accuracy at the same time.

7.2 Mathematical Background of the Co-Kriging Method

Co-Kriging is an extension of Kriging methods that exploits the correlation between accurate and coarse model data to improve the prediction accuracy [38]. In this work the autoregressive model is adopted, which assumes that the data of high level evaluations are correct and the different levels of the same model are correlated in some way [70]. This is known as a Markov property, which means that no more can be learnt from the low level if the value of the high level at this point is known. The following mathematical formulations

are based on [38][39].

Supposed two datasets are given: the accurate, expensive to evaluate data with function values $\mathbf{y}_e$ at n_e sample points $\mathbf{X}_e$ (high-fidelity) and the coarse, cheap to evaluate data with function values $\mathbf{y}_c$ at n_c sample points $\mathbf{X}_c$ (low-fidelity) ($\mathbf{X}_e \subset \mathbf{X}_c$). These data can be concatenated to be a combined set of points:

$$\mathbf{X} = \begin{pmatrix} \mathbf{X}_c \\ \mathbf{X}_e \end{pmatrix}. \tag{7.1}$$

Then the values at the points in $\mathbf{X}$ are treated as they are from a stochastic process. This can be denoted using the set of random vectors:

$$\mathbf{Y} = \begin{pmatrix} \mathbf{Y}_c(\mathbf{X}_c) \\ \mathbf{Y}_e(\mathbf{X}_e) \end{pmatrix}. \tag{7.2}$$

Creating a Co-Kriging model can be interpreted as constructing two Kriging models in a sequence [71]. Therefore, the expensive to evaluate data (high-fidelity) can be approximated as the cheap to evaluate data (low-fidelity) multiplied by a scale factor ρ plus a Gaussian process Z_d:

$$Z_e(\mathbf{x}) = \rho Z_c(\mathbf{x}) + Z_d(\mathbf{x}), \tag{7.3}$$

where Z_c, Z_e represent the Gaussian processes of the low-fidelity and high-fidelity datasets respectively, and Z_d represents the Gaussian process of the difference between ρZ_c and Z_e. The covariance matrix is then given by:

$$\text{cov}\{\mathbf{Y}(\mathbf{X}), \mathbf{Y}(\mathbf{X})\} = \begin{pmatrix} \text{cov}\{\mathbf{Y}_c(\mathbf{X}_c), \mathbf{Y}_c(\mathbf{X}_c)\} & \text{cov}\{\mathbf{Y}_e(\mathbf{X}_e), \mathbf{Y}_c(\mathbf{X}_c)\} \\ \text{cov}\{\mathbf{Y}_e(\mathbf{X}_e), \mathbf{Y}_c(\mathbf{X}_c)\} & \text{cov}\{\mathbf{Y}_e(\mathbf{X}_e), \mathbf{Y}_e(\mathbf{X}_e)\} \end{pmatrix}, \tag{7.4}$$

with

$$\begin{aligned} \text{cov}\{\mathbf{Y}_c(\mathbf{X}_c), \mathbf{Y}_c(\mathbf{X}_c)\} &= \text{cov}\{Z_c(\mathbf{X}_c), Z_c(\mathbf{X}_c)\} \\ &= \sigma_c^2 \mathbf{\Psi}_c(\mathbf{X}_c, \mathbf{X}_c), \end{aligned} \tag{7.5}$$

$$\begin{aligned} \text{cov}\{\mathbf{Y}_e(\mathbf{X}_e), \mathbf{Y}_c(\mathbf{X}_c)\} &= \text{cov}\{\rho Z_c(\mathbf{X}_c) + Z_d(\mathbf{X}_c), Z_c(\mathbf{X}_e)\} \\ &= \rho \sigma_c^2 \mathbf{\Psi}_c(\mathbf{X}_c, \mathbf{X}_e), \end{aligned} \tag{7.6}$$

$$\text{cov}\{\mathbf{Y}_e(\mathbf{X}_e), \mathbf{Y}_e(\mathbf{X}_e)\} = \text{cov}\{\rho Z_c(\mathbf{X}_e) + Z_d(\mathbf{X}_e), \rho Z_c(\mathbf{X}_e) + Z_d(\mathbf{X}_e)\}$$
$$= \rho^2 \sigma_c^2 \mathbf{\Psi}_c(\mathbf{X}_e, \mathbf{X}_e) + \sigma_d^2 \mathbf{\Psi}_d(\mathbf{X}_e, \mathbf{X}_e). \tag{7.7}$$

Thus, the complete covariance matrix is:

$$\mathbf{C} = \begin{pmatrix} \sigma_c^2 \mathbf{\Psi}_c(\mathbf{X}_c, \mathbf{X}_c) & \rho \sigma_c^2 \mathbf{\Psi}_c(\mathbf{X}_c, \mathbf{X}_e) \\ \rho \sigma_c^2 \mathbf{\Psi}_c(\mathbf{X}_c, \mathbf{X}_e) & \rho^2 \sigma_c^2 \mathbf{\Psi}_c(\mathbf{X}_e, \mathbf{X}_e) + \sigma_d^2 \mathbf{\Psi}_d(\mathbf{X}_e, \mathbf{X}_e) \end{pmatrix}, \tag{7.8}$$

where σ_c^2 denotes the variance of the process Z_c, σ_d^2 is the variance of the process Z_d, and $\mathbf{\Psi}_c(\mathbf{X}_c, \mathbf{X}_c)$, for example, represents a matrix of correlations based on an exponential correlation function between the data $\mathbf{X}_c$ and $\mathbf{X}_c$. This exponential correlation function between two points $\mathbf{x}^i$ and $\mathbf{x}^j$ is given by

$$\text{cor}(\mathbf{x}_i, \mathbf{x}_j) = \exp\left(-\sum_{l=1}^{d} \theta_l |x_l^i - x_l^j|^{p_l}\right), \tag{7.9}$$

where d is the dimension of the variables. The Co-Kriging prediction of the expensive to evaluate function at the $\mathbf{x}$ can be expressed as:

$$\widehat{y}_e(\mathbf{x}) = \widehat{\mu} + \mathbf{r}^{\mathrm{T}} \mathbf{C}^{-1}(\mathbf{y} - \mathbf{1}\widehat{\mu}) \tag{7.10}$$

with

$$\mathbf{r} = \begin{pmatrix} \rho \sigma_c^2 \mathbf{\Psi}_c(\mathbf{X}_c, \mathbf{x}) \\ \rho^2 \sigma_c^2 \mathbf{\Psi}_c(\mathbf{X}_e, \mathbf{x}) + \sigma_d^2 \mathbf{\Psi}_d(\mathbf{X}_e, \mathbf{x}) \end{pmatrix} \tag{7.11}$$

and

$$\widehat{\mu} = \frac{\mathbf{1}^{\mathrm{T}} \mathbf{C}^{-1} \mathbf{y}}{\mathbf{1}^{\mathrm{T}} \mathbf{C}^{-1} \mathbf{1}}. \tag{7.12}$$

In Eqn. (7.10) there are five parameters to estimate: $\boldsymbol{\theta}_c$, $\boldsymbol{\theta}_d$, $\mathbf{p}_c$, $\mathbf{p}_d$ and ρ. The parameters $\boldsymbol{\theta}_c$, $\mathbf{p}_c$ can be estimated by the Kriging model of the coarse dataset $(\mathbf{X}_c, \mathbf{y}_c)$, while the parameters $\boldsymbol{\theta}_d$, $\mathbf{p}_d$ and ρ are determined by the Kriging model of the residuals $(\mathbf{X}_e, \mathbf{d})$ with

$$\mathbf{d} = \mathbf{y}_e - \rho \mathbf{y}_c(\mathbf{X}_e), \tag{7.13}$$

where $\mathbf{y}_c(\mathbf{X}_e)$ are values of $\mathbf{y}_c$ at the locations of $\mathbf{X}_e$. Thus, a Co-Kriging model can be constructed by two separate Kriging models and performing two maximum likelihood estimation (MLE) of each corresponding Kriging model. Since the cheap to evaluate data is considered to be independent of the expensive to evaluate data, the optimal values of the parameters $\widehat{\boldsymbol{\theta}}_c$ and $\widehat{\mathbf{p}}_c$ can be estimated by maximizing the ln-likelihood function based on the cheap to evaluate data. Then the optimal value of $\widehat{\sigma}_c^2$ can be calculated using

$$\widehat{\sigma}_c^2 = \frac{(\mathbf{y}_{\mathrm{c}} - \mathbf{1}\widehat{\mu}_{\mathrm{c}})^{\mathrm{T}}\mathbf{\Psi}_{\mathrm{c}}(\mathbf{X}_{\mathrm{c}}, \mathbf{X}_{\mathrm{c}})^{-1}(\mathbf{y}_{\mathrm{c}} - \mathbf{1}\widehat{\mu}_{\mathrm{c}})}{n_c} \tag{7.14}$$

with

$$\widehat{\mu}_{\mathrm{c}} = \frac{\mathbf{1}^{\mathrm{T}}\mathbf{\Psi}_{\mathrm{c}}(\mathbf{X}_{\mathrm{c}}, \mathbf{X}_{\mathrm{c}})^{-1}\mathbf{y}_{\mathrm{c}}}{\mathbf{1}^{\mathrm{T}}\mathbf{\Psi}_{\mathrm{c}}(\mathbf{X}_{\mathrm{c}}, \mathbf{X}_{\mathrm{c}})^{-1}\mathbf{1}}, \tag{7.15}$$

where n_c is the number of sample points for the cheap to evaluate data. Similar to the estimation of the $\widehat{\boldsymbol{\theta}}_c$ and $\widehat{\mathbf{p}}_c$, the optimal values of the the parameters $\widehat{\boldsymbol{\theta}}_d$, $\widehat{\mathbf{p}}_d$ and $\widehat{\rho}$ can be obtained by maximizing the ln-likelihood function based on the residuals $(\mathbf{X}_e, \mathbf{d})$. Then the optimal value of $\widehat{\sigma}_d^2$ can be expressed as

$$\widehat{\sigma}_d^2 = \frac{(\mathbf{d} - \mathbf{1}\widehat{\mu}_{\mathrm{d}})^{\mathrm{T}}\mathbf{\Psi}_{\mathrm{d}}(\mathbf{X}_{\mathrm{e}}, \mathbf{X}_{\mathrm{e}})^{-1}(\mathbf{y}_{\mathrm{d}} - \mathbf{1}\widehat{\mu}_{\mathrm{d}})}{n_e} \tag{7.16}$$

with

$$\widehat{\mu}_{\mathrm{d}} = \frac{\mathbf{1}^{\mathrm{T}}\mathbf{\Psi}_{\mathrm{d}}(\mathbf{X}_{\mathrm{e}}, \mathbf{X}_{\mathrm{e}})^{-1}\mathbf{d}}{\mathbf{1}^{\mathrm{T}}\mathbf{\Psi}_{\mathrm{d}}(\mathbf{X}_{\mathrm{e}}, \mathbf{X}_{\mathrm{e}})^{-1}\mathbf{1}}, \tag{7.17}$$

where n_e is the number of sample points for the expensive to evaluate data. Further, the estimated mean square error (MSE) $\widehat{\mathrm{s}}^2(\mathbf{x})$ in the Co-Kriging prediction at the point $\mathbf{x}$ can be calculated using

$$\widehat{\mathrm{s}}^2(\mathbf{x}) \approx \rho^2\widehat{\sigma}_c^2 + \widehat{\sigma}_{\mathrm{d}}^2 - \mathbf{r}^{\mathrm{T}}\mathbf{C}^{-1}\mathbf{r} + \frac{1 - \mathbf{1}^{\mathrm{T}}\mathbf{C}^{-1}\mathbf{r}}{\mathbf{1}^{\mathrm{T}}\mathbf{C}^{-1}\mathbf{1}}. \tag{7.18}$$

More detailed mathematical information about the Co-Kriging model can be found in [38][39][70].

7.3 Optimization Procedure

As described above, the Co-Kriging model is based on at least two datasets. The schematic view of the optimization process based on two datasets is illustrated in Fig. (7.1). The proposed optimization algorithm using the Co-Kriging method can be summarized as:

1) Generate n_c space-filling sample points $\mathbf{X}_c$ using the maximin LHS strategy, which is introduced in chapter 6.

2) Evaluate the cheap to evaluate objective function f_c at the sample points $\mathbf{X}_c$ to get the low fidelity data $(\mathbf{X}_c, \mathbf{y}_c)$.

3) Choose n_e sample points $\mathbf{X}_e$ from the in 1) generated sample points $\mathbf{X}_c$ using the exchange algorithm described in [39].

4) Evaluate the expensive to evaluate objective function f_e at the sample points $\mathbf{X}_e$ to get the high-fidelity data $(\mathbf{X}_e, \mathbf{y}_e)$.

5) Assemble a Co-Kriging model based on the datasets $(\mathbf{X}_c, \mathbf{y}_c)$ and $(\mathbf{X}_e, \mathbf{y}_e)$.

6) Search for the optimum $\mathbf{x}^{\text{opt}}$ of the Co-Kriging surrogate model using the DIRECT algorithm.

7) Evaluate the expensive to evaluate objective function f_e at the point $\mathbf{x}^{\text{opt}}$.

Figure 7.1: The schematic view of the optimization process using the Co-Kriging method.
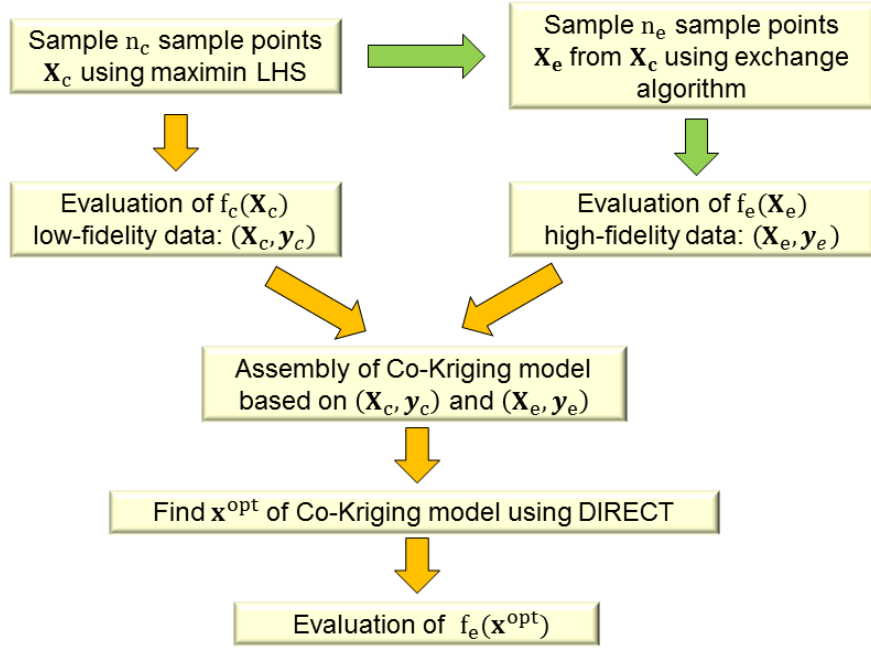
7.4 Demonstation with a One-Variable Analytical Function

In this section the proposed algorithm is tested with a one-variable analytical function to demonstrate how the Co-Kriging method works. Given are a 1D Schwefel's function

$$f_e(x) = -x\sin(\sqrt{|x|}), x \in [-500, 500] \tag{7.19}$$

and an approximated estimation of this function given by

$$f_c(x) = 0.5 f_e(x) + 0.3(x - 50) + 50. \tag{7.20}$$

Assuming that Eqn. (7.20) is cheaper to evaluate than Eqn. (7.19), two datasets $(\mathbf{X}_e, f_e(\mathbf{X}_e))$ and $(\mathbf{X}_c, f_c(\mathbf{X}_c))$ can be obtained. In particular, for the cheap to evaluate

function $f_c(x)$ twenty-one sample points are generated which are uniformly distributed in the whole design domain. This yields the low-fidelity data $(\mathbf{X}_c, f_c(\mathbf{X}_c))$. The expensive to evaluate function $f_e(x)$ is just estimated at four of these points with $\mathbf{X}_e = \{-350, -150, 150, 350\}$ to get the high-fidelity data $(\mathbf{X}_e, f_e(\mathbf{X}_e))$. Fig. (7.2) shows that the graphs of the cheap and expensive to evaluate function are very similar to each other, despite of having different global optimums. Hence, the functions f_c and f_e have some correlation to some extent. As illustrated in Fig. (7.3), a Kriging model based on four sample points $(\mathbf{X}_e, f_e(\mathbf{X}_e))$ shows a poor approximation to this deliberately deceptive function, whilst the Co-Kriging model is very close to the true function f_e, as shown in Fig. (7.4). In this case, the surrogate model is significantly improved by additional twenty-one sample points from the cheap to evaluate function.

Figure 7.2: The expensive function evaluations and the supposedly cheap function evaluations of the one-variable Schwefel's function.
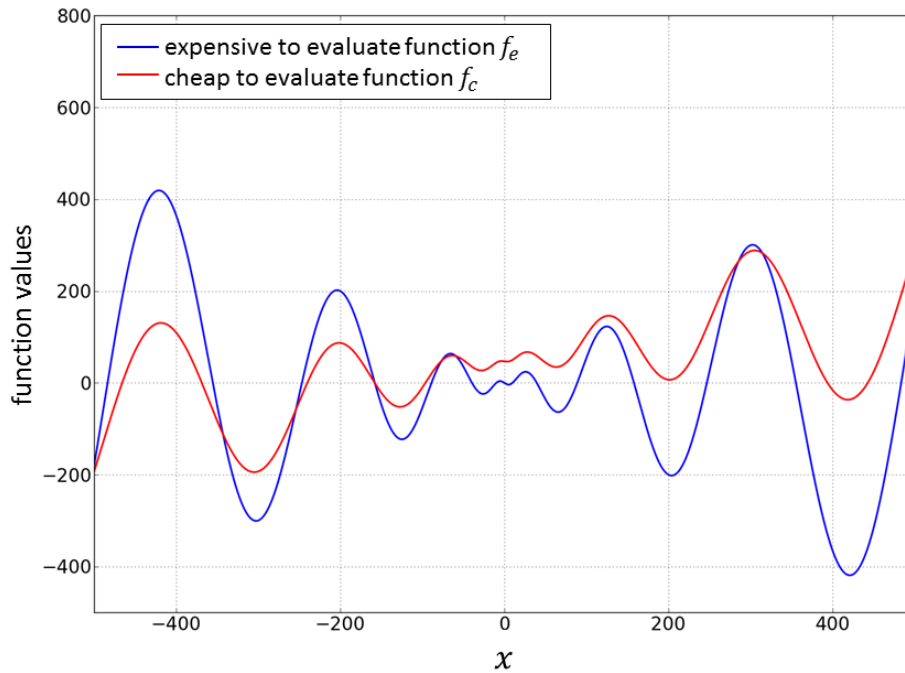
In Fig. (7.5) the estimated MSE $s^2(\mathbf{x})$ in Eqn. (7.18) is shown. Just like for ordinary Kriging, the estimated MSE is zero if $\mathbf{x} \in \mathbf{X_e}$. If $\mathbf{x} \in \mathbf{X}_c/\mathbf{X}_e$, the difference between $\rho \mathbf{Y}_c(\mathbf{X}_e)$ and $\mathbf{Y}_e(\mathbf{X}_e)$ is simple, which can be characterized by low $\boldsymbol{\theta}_d$. The estimated error is also very low.

Figure 7.3: The Kriging interpolation based on the four expensive sample points of the one-variable Schwefel's function.
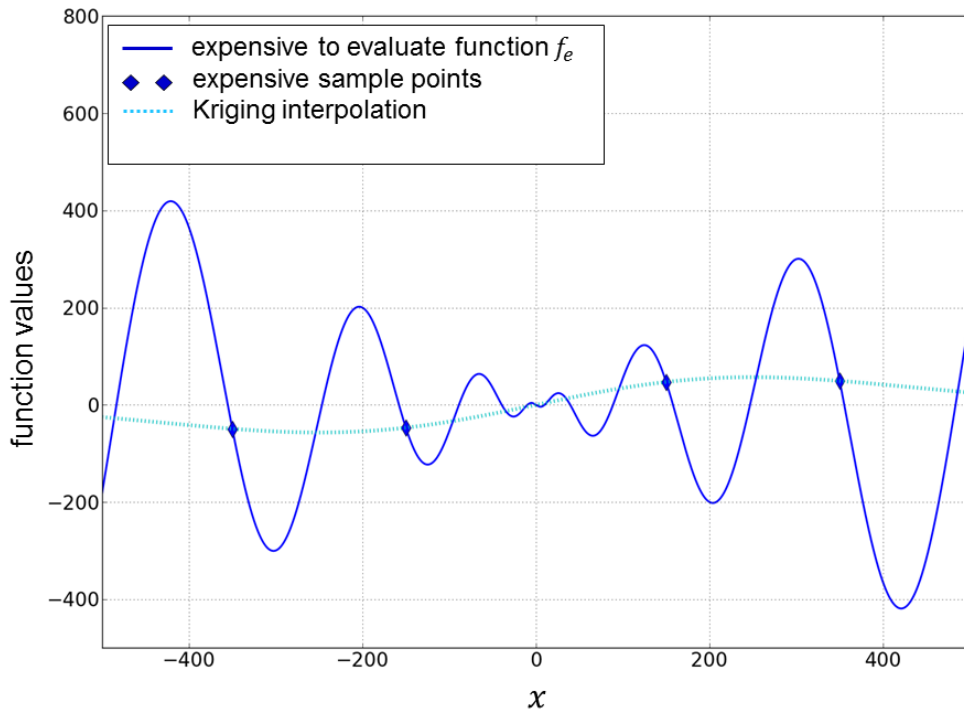
Figure 7.4: The Co-Kriging interpolation of the one-variable Schwefel's function. The Kriging interpolation using four expensive sample points (diamonds) is significantly improved using extensive sample points (circles) from the supposedly cheap to evaluate function [P5].
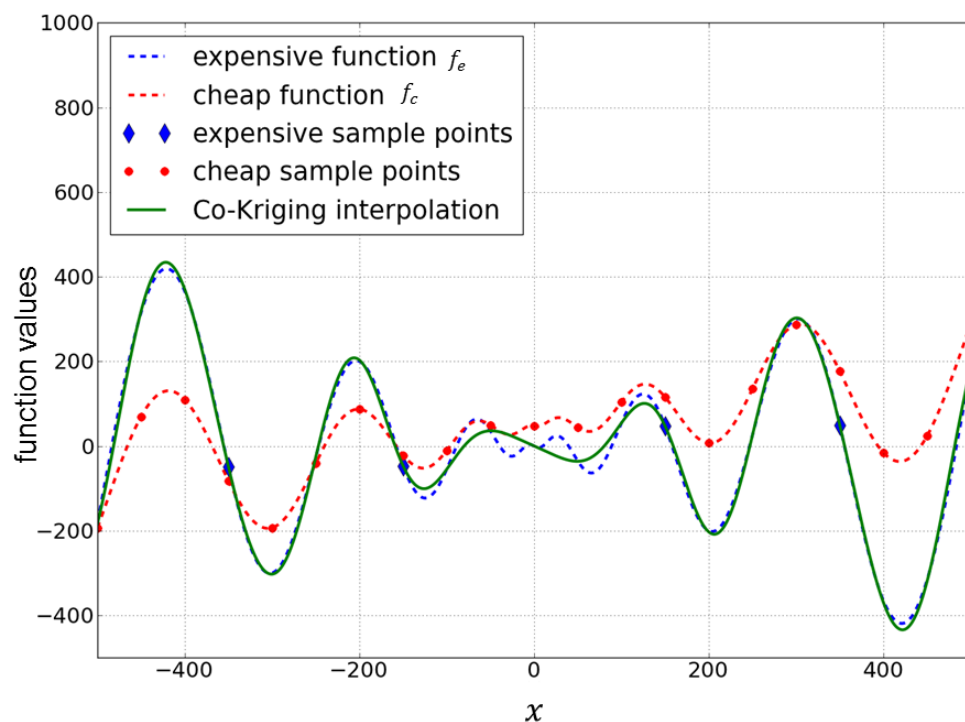
Figure 7.5: The estimated mean square errors in the Co-Kriging prediction for one-variable Schwerfel's function [P5].
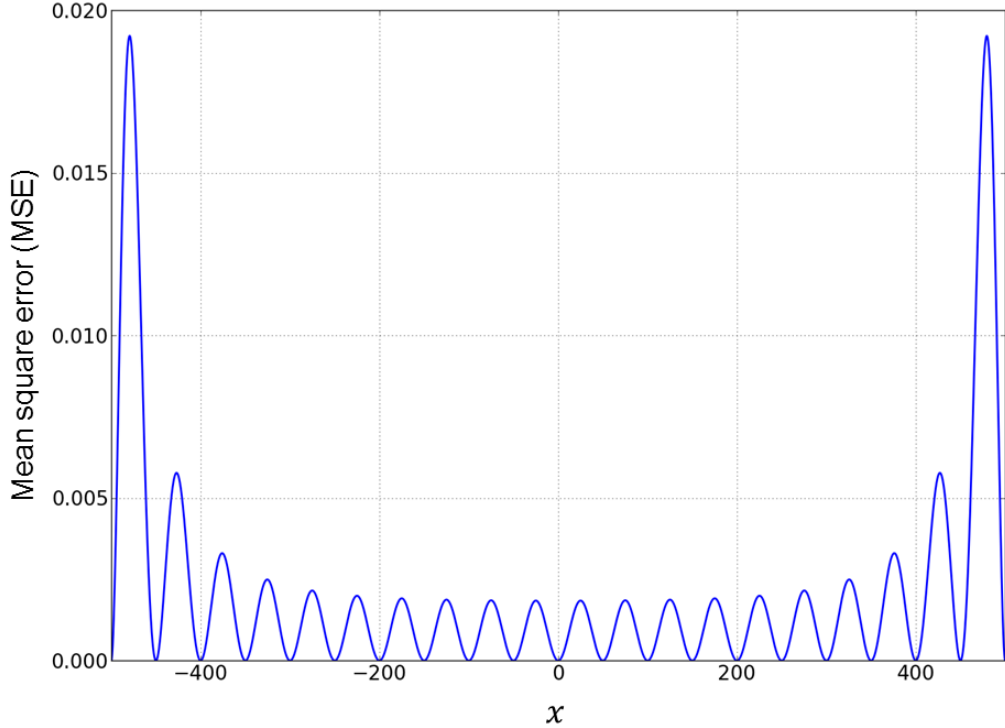
7.5 Optimization of a Corona Ring

In this section a realistic practical problem from HV technology is given to verify the optimization process using the Co-Kriging method. Three geometrical parameters of a corona ring are to be optimized for large scale outdoor insulators, which are also adopted in the chapter 6. To get the optimal field grading effect, three principle geometrical parameters, the ring radius R_{major}, the radius of the ring tube R_{minor} and the distance between the ring and the energized end fitting d, can be optimized in the caculation domain [170 mm, 250 mm] x [20 mm, 50 mm] x [0 mm, 200 mm]. The geometrical details about this real world example are illustrated in Fig. (7.6).

As shown in Fig. (7.6), the whole simulated model including insulator, corona ring, traverse and transmission lines is non-rotationally symmetric. Hence, a 3D model with fine meshes and second order ansatz functions is required to accurately evaluate the electric field strength along the surface of the insulator. This model results in almost 9 million degrees of freedom in the discrete model and it takes almost 60 minutes to run a single simulation including the mesh generation[1]. These 3D accurate FEM simulation results are considered

---

[1]The 3D simulation code MEQSICO is based on C++ and the computer system for these simulations is a 2.8 GHz 48 cores AMD Opteron Linux system.

Figure 7.6: The simulated insulator model with corona ring. There are three geometrical parameters of the corona ring to be optimized. The traverse (grey) is grounded and the transmission lines and corona ring are at HV-level [P5].
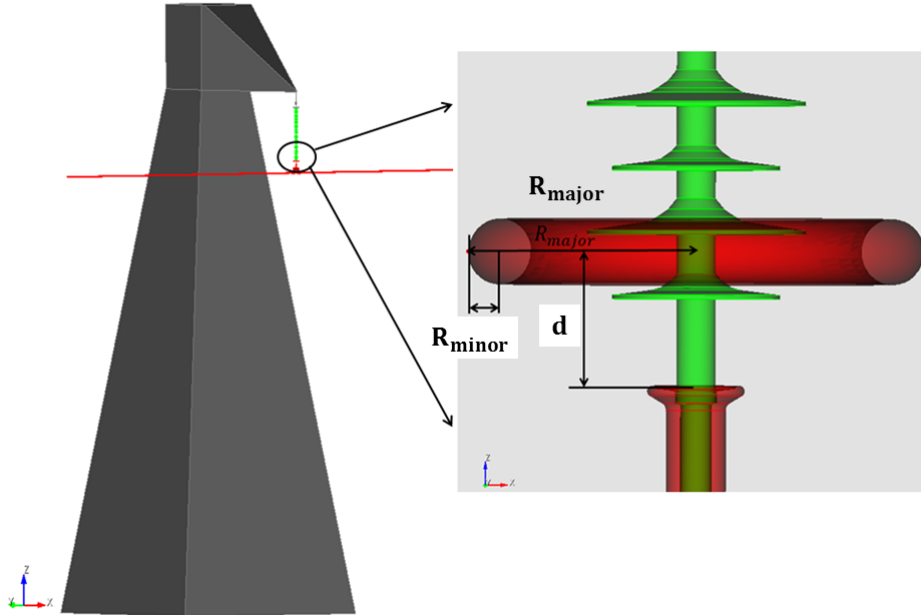
to be high-fidelity expensive to evaluate data. To get a well-fitted Kriging surrogate model using plainly 3D expensive simulation results, a relative large number of sample points are required. Since the simulations of the 3D model are quite time consuming, the number of 3D function evaluations should be limited. In this case, in order to get the information in the regions, where the accurate expensive simulations are not evaluated, the extensive points are sampled and the reduced 2D simulations at these points are carried out. To obtain an approximated cheap to evaluate model, the non-rotational components of the 3D model, namely the non-rotationally symmetrical part of the traverse and transmission lines are removed. Then the remaining part is further reduced into a 2D model, as illustrated in Fig. (7.7). The main difference between the accurate 3D model and the reduced 2D model is that the boundary conditions in the reduced 2D model are also supposed to be rotationally symmetrical (see Fig. (7.8)). This reduced 2D model with first order ansatz functions has just about 58777 degrees of freedom and leads to a significant reduction of computational time[2]. Hence, a large number of sample points for 2D simulations can be chosen to get more information about the evaluation function in the whole design domain. These 2D coarse FEM simulation results are considered to be low-fidelity data. The information about the accurate 3D model and the reduced coarse 2D model are compared and given in Table (7.1).

---

[2]The 2D simulation code eqsLab is based on Matlab and the computer system for these simulations is a 2.67 GHz 2 cores Intel(R) Xeon(R) Windows system.

Figure 7.7: The reduced 2D rotational symmetrical model for the corona ring optimization problem [P5].
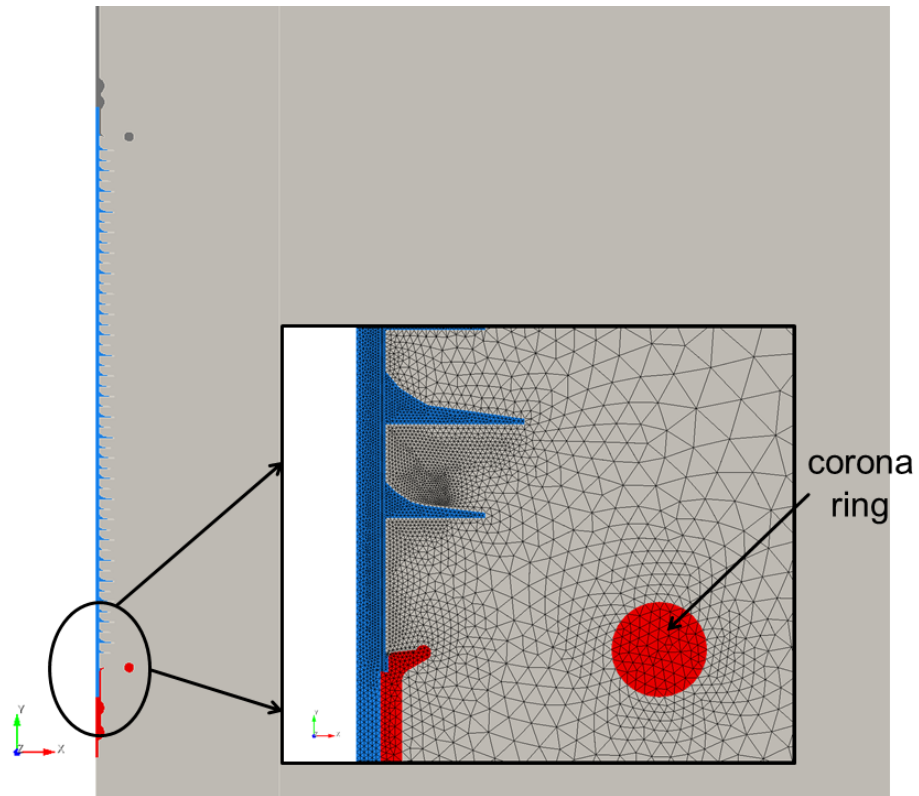
Figure 7.8: Boundary conditions for the reduced 2D model of the corona ring optimization problem.
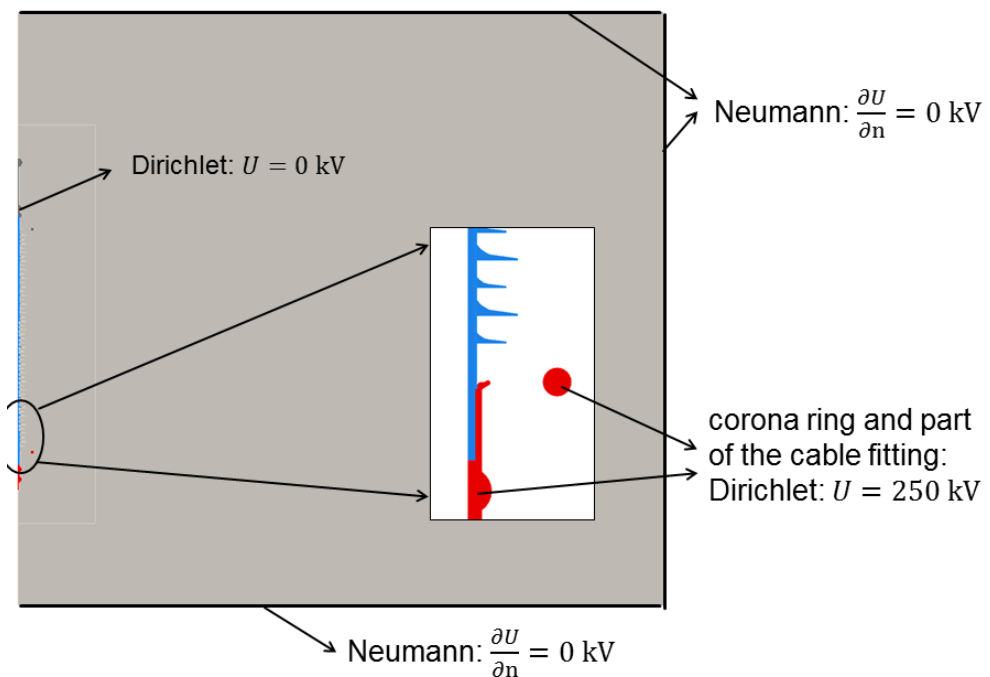
Table 7.1: Information about the hight-fidelity data and low-fidelity data of the corona ring optimization problem in comparison.

	Dimension	Ansatz function	DOF	Evaluation time
High-fidelity data	3D	second order	9 million	60 Min.
Low-fidelity data	2D	first order	58777	6 Min.

Table 7.2: Relative errors using different sample points n_{2D} for 2D reduced simulations [P5].

	$n_{2D} = 40$ $n_{3D} = 10$	$n_{2D} = 60$ $n_{3D} = 10$	$n_{2D} = 80$ $n_{3D} = 10$
rel. error	6.4%	2.48%	1.06%

The influence of the number of sample points for 2D coarse simulations on the accuracy of the surrogate model is also investigated. In this work, different numbers of sample points for reduced 2D simulations ($n_{2D} = 20, 40, 60, 80$) are sampled in the design domain using the space-filling maximin Latin Hypercube sampling strategy. Because of the expense just ten sample points are chosen from these 2D sample points for the expensive accurate 3D simulations using the exchange algorithm. As a reference, the DIRECT method, which is introduced in chapter 6, is adopted to optimize the corona ring using just 3D accurate simulations. The optimum of the electrical field evaluated by the DIRECT method $E_{\text{opt,dir}} = 2.82$ kV/cm is supposed to be the reference value for the optimum. Then the relative modelling error of the Co-Kriging surrogate model can be calculated by

$$\text{rel. error} = \frac{|E_{\text{opt,co}} - E_{\text{opt,dir}}|}{|E_{\text{opt,dir}}|}, \tag{7.21}$$

where $E_{\text{opt,co}}$ is the optimal value of the Co-Kriging surrogate model. The modelling error using different 2D sample points n_{2D} are shown in Table (7.2). Using $n_{2D} = 80$ sample points for 2D simulations the relative error is nearly 1%. The results are also compared to the ordinary Kriging method using the one-then-two stage infill strategy based on merely 3D simulations. For comparable results the optimization process using Co-Kriging method has a rather good speed-up, as shown in Table (7.3).

7.6 Summary

In this chapter an optimization procedure using the Co-Kriging method combining high-fidelity data and low-fidelity data is introduced. For the ordinary Kriging methods based on the high-fidelity data, a certain number of the sample points should be sampled and the expensive function evaluation are carried out at those sample points. If the function

Table 7.3: Optimization results of the corona ring using different methods in comparison [P5].

Method	n_{3D}	n_{2D}	E_{opt} (kV/cm)	location (mm)	total time (h)
DIRECT	157	–	2.82	R_{major} : 248.52 R_{minor} : 48.33 d : 107.41	**157**
Kriging (one-then-two-stage)	39	–	2.84	R_{major} : 248.26 R_{minor} : 49 d : 108.33	**39**
Co-Kriging	10	80	2.85	R_{major} : 248.18 R_{minor} : 48.58 d : 108.29	**18**

evaluation at each sample point is time-consuming, i.e. very complex FEM simulations of large-scale models, the total time of the optimization process could be very large and unreasonable for industrial design processes. Compared to the ordinary Kriging method, the Co-Kriging methods do not only use accurate expensive to evaluate data (high-fidelity) but also extensive coarse cheap to evaluate data (low-fidelity) if low-fidelity data are available. In this case, the number of the sample points for the expensive function evaluations can be reduced, and the information about the regions, where the expensive to evaluate function is not sampled, can be obtained by the sample points for the coarse cheap to evaluate function. Hence, the optimization process using the Co-Kriging method allows a faster but still accurate optimization. This is demonstrated by the analytical function and the realistic corona ring design problem in the previous sections. This method is specially suitable for problems for which the acquisition of high-fidelity data is much more time-consuming than that of low-fidelity data. This is usually the case for the optimization of the large-scale high-voltage devices, especially for the devices with non-linear materials.

However, it is not always easy to acquire low-fidelity data, because the high-fidelity data and the low-fidelity data should have a certain correlation with each other. For high-voltage devices, sometimes an equivalent circle can be used to get the low-fidelity data. FEM simulations with coarse meshes can also be used to the low-fidelity data. As shown in the example of the corona ring optimization problem, the low-fidelity data can in that case be obtained by a dimension reduced 2D model, despite the originally non-rotationally symmetric model. The reduced 2D model is highly correlated with the 3D model, leading to a high accuracy of the Co-Kriging surrogate model. This is because the main components of the 3D model, the insulator and the corona ring are rotationally symmetrical. Hence, the removal of the non-rotationally parts of the 3D model has no strong influence on the electric field strength along the surface of the insulator. In this case, a large number of

sample points for the 2D simulations can be chosen to get more information for the design domains.

However, if the evaluation of the low-fidelity data requires a significant cost, the choice of n_c should be more conservative. In this case, an infill strategy such as the one-stage-approach, the two-stage-approach and the one-then-two stage approach can be adopted to choose the sample points for the low-fidelity data.

8 General Conclusion and Future Work

8.1 General Conclusion

Microvaristor-filled composite materials can be applied in high-voltage devices to reduce the electric field strength if required. Compared to the traditional field grading materials, microvaristor-filled composite materials have some advantages, such as robustness, less sensitivity to external parameters and high non-linearity. However, the lack of sufficient experience in the use of this material for high-voltage devices, especially regarding the design parameters, material degradation process and long-term behavior, results in few commercial applications until now. Hence, in this research the potential applications of the microvaristor-filled composite materials in high-voltage outdoor insulators and gas-insulated bushings are investigated.

In this work a review about properties of microvaristor and microvaristor-filled materials was presented in chapter 2. The fundamental properties of ceramic varistor materials are summarized. Furthermore, some external parameters affecting the electrical properties of microvaristor-filled composite materials are discussed. As a spin-off product of ceramic varistors, microvaristors have similar electrical properties as the varistors, such as electric field dependent conductivity and intrinsic high non-linearity. The nature of the carrier-matrices also have an influence on the electrical properties. It should be noted that the switching points of microvaristor powder and microvaristor-filled materials are differently defined by manufacturers and scientists. Most manufacturers provide just a technical data sheet of microvaristor powders. If they are mixed into an insulating or semiconducting material, electrical properties could be different to the original powders. In this case, characterizations of microvaristor-filled materials using different carrier materials should be carried out for the application.

The first investigation of this work was the application of microvaristor-filled silicone rubber to high-voltage outdoor insulators (chapter 4). For this purpose, finite element simulations based on electro-quasistatic approximations (chapter 3) were carried out to calculate electric field distributions. The initial idea was to apply this material directly onto the surface of insulators. For this option, the local high electric field strength can be well reduced not only at the triple points of water droplets but also across the dry bands on the surface of the insulator. However, this option does not show a sufficient tracking and

erosion resistance in the laboratory test. As a result, this option is unsuitable for outdoor applications. To solve this problem a protection silicone layer above the microvaristor layer is adopted. Using this configuration the potential can be homogenized and the high electric field at the triple points of water drops can be reduced as well. However, the high electric field strength across the dry bands can just be reduced slightly in the presence of the dry bands on the surface.

Another investigation was the application of microvaristor-filled epoxy resin to 550 kV compact high-voltage gas-insulated bushings (chapter 5). Because of limited literature about the microvaristor-filled epoxy resin, the investigation about this composite material was carried out first. For this purpose, samples were produced to explore the necessary filler content and the influence of the temperature. The experimental results showed that 75 m% filler contents are required to have an obvious switching transition of the $E - J$ curve and the switching point is just slightly affected by the temperature from 23°C to 80°C. FEM simulations were performed to determine the suitable switching point and geometrical parameters of the microvaristor-filled epoxy resin. Then the prototype of this compact bushing, which was designed by FEM simulations, was built up and tested in the high-voltage laboratory. Both theoretical and experimental results demonstrate that using the microvaristor-filled epoxy resin allows for a compact design of bushings.

For the design of high-voltage devices, some geometrical parameters and material parameters can be optimized to yield better electric field distributions. For this purpose, an appropriate optimization algorithm is required. One of the major obstacles to the use of optimization is the time-consumption of FEM simulations of large-scale complex problems and the lack of gradient information. In this case, a surrogate model can be adopted, such as Kriging (chapter 6) and Co-Kriging (chapter 7), to speed up time-consuming simulations using model approximation. In this research the Kriging method with one-then-two stage infill strategies and the Co-Kriging method using different levels of datasets were studied and adjusted to optimize large-scale high-voltage devices. Both methods were tested with some analytical functions and applied to the corona ring optimization problem with three geometrical parameters. The results demonstrate that both methods enable a faster but still accurate optimization process.

8.2 Future Work

Based on the results of the present research, the following issues for future investigations can be identified:

- Perform further investigation about the application of the microvaristor-filled epoxy resin in high-voltage outdoor insulators. For example, choose a lower switching point

and a better carrier matrix to apply the microvaristor-filled material directly onto the surface.

- In this work, the conductive layers on the surface of insulators are modelled as layers with constant conductivities. However, the layers may have different humidities. In this case the conductivities are not constant. This may have an influence on the formation of dry bands. Thus, a better model is required to model dry bands and conductive layers.

- Research on thermal behavior of microvaristor-filled epoxy resin in high-voltage bushings is required for the long-therm behavior.

- The optimization algorithm using Kriging and Co-Kriging method is tested with a problem with three geometrical parameters. The study about these methods for a larger number of parameters is also desirable.

A Classification of EQS and MQS Approximations

Three different methods, which are introduced in references [27][54][119], are presented to classify electro-quasistatic and magneto-quasistatic approximations.

Based on Energy Densities

For the selection of a suitable approximation for a slowly time-varying fields problem, the governing electric and magnetic energy density w_e and w_m can be used to classify the approximation [54]. For the case $w_e \gg w_m$, the electro-quasistatic approximation is suitable, whereas the magneto-quasistatic approximation is applicable to the problems with $w_m \gg w_e$. However, for most application problems the electric and magnetic energy densities are not known in advance. To estimate the energies the electric and magnetic fields should be solved at first. Hence, this method is not practical if the electric and magnetic fields are unknown.

Based on the Time Constant

To get over this problem, the classification based on the significant time constant is derived in [54][119]. The time constant of dielectric relaxation is defined as

$$\tau_e = \frac{\varepsilon}{\kappa} \tag{A.1}$$

and the time constant of magnetic diffusion is given by

$$\tau_m = \mu \kappa l^2, \tag{A.2}$$

where ε is the dielectric permittivity, κ is the electric conductivity, μ is the magnetic permeability and l is the characteristic spatial dimension of field problems. With that the transit time τ_{em} is given by the geometric average of τ_e and τ_m:

$$\tau_{em}^2 = \tau_e \tau_m. \tag{A.3}$$

For slowly time-varying fields to be described with a quasistatic model, the characteristic time constant τ should be much greater than the transit time τ_{em}:

$$\left(\frac{\tau_{em}}{\tau}\right)^2 \ll 1 \tag{A.4}$$

With those definitions the valid domains for electro-quasistatic and magneto-quasistationary approximations are classified with the corresponding boundaries, as demonstrated in Fig. (A.1).

Figure A.1: Qualitative boundaries of electro-quasistatic fields and magneto-quasi-stationary fields based on the characteristic time τ of a given field problem [119].
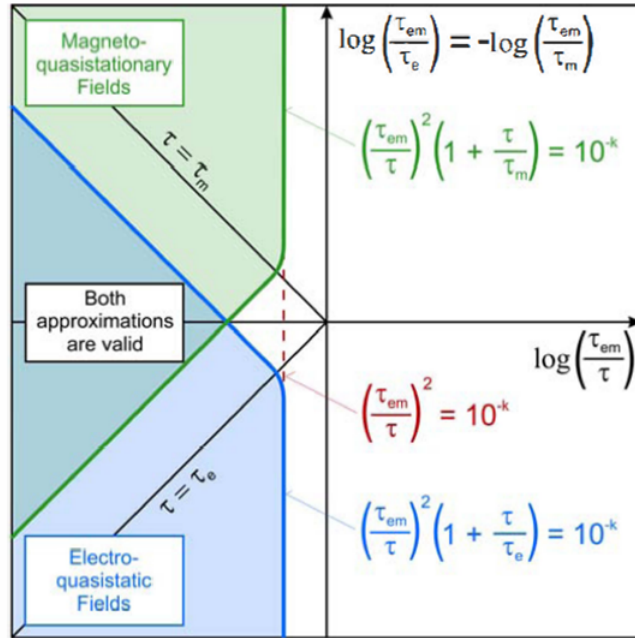
Based on Material Parameters and Frequency

In [27] the classification of the different approximations based on material parameters and frequency is introduced. The upper angular frequency limit w_q for the validity range of slowly varying-field assumptions, respectively the quasistationary approximation, is given by

$$w_q = \frac{c}{d} = \frac{1}{d\sqrt{\varepsilon\mu}}, \tag{A.5}$$

where d denotes the diameter of a finite spatial domain Ω. In this case the displacement current density of the induced field $j\omega\vec{D}_i$ is negligible for the first Maxwell's equation in the frequency domain. This equation can be expressed by dividing the total current density $\vec{J}$

into several components:

$$\text{curl}\vec{H} = \vec{J} + j\omega\vec{D}_o = \kappa\vec{E}_i + \underbrace{\kappa\vec{E}_o + \vec{J}_s + j\omega\vec{D}_o}_{=:\vec{S}_o}, \tag{A.6}$$

with

$$\vec{E} = \underbrace{-j\omega\vec{A}}_{\vec{E}_i}\underbrace{-\text{grad}\varphi}_{\vec{E}_o}, \tag{A.7}$$

where $\vec{E}_i$, $\vec{E}_o$ respectively denotes the solenoidal and irrotational parts of the electric field $\vec{E}$, $\vec{D}_o$ is the electric displacement field with $\vec{D}_o = \varepsilon\vec{E}_o$, $\vec{J}_s$ is the impressed current density of the given source, $\vec{A}$ is the vector potential and φ is the scalar potential.

The first Maxwell's equation (A.6) can be now further simplified by neglecting one of those de-composited components of the total current density $\vec{J}$ under different conditions. These can be summarized into three classifications, as shown in Table (A.1):

a) **The quasistatic field:**

$$|\kappa\vec{E}_o| \ll |j\omega\vec{D}_o| \Leftrightarrow \kappa \ll \omega\varepsilon \Leftrightarrow 1 \ll \omega\tau_e \tag{A.8}$$

In some references in literature, the term of a quasistatic field is used for a quasistationary field. In [27] this term is reserved for slowly time-varying fields satisfying the equations of electrostatics. This approximation is for the case that the conductivity is small or that the frequency is high enough but still well below the upper frequency limit w_q. It leads to omission of the conduction current density produced by E_o and E_i in the Eqn. (A.6).

b) **The displacement-current-free quasistationary field:**

$$|j\omega\vec{D}_o| \ll |\kappa\vec{E}_o| \Leftrightarrow \omega\varepsilon \ll \kappa \Leftrightarrow \omega\tau_e \ll 1 \tag{A.9}$$

For good conductors and frequencies which are not too high, the quasistatic displacement current density $j\omega\vec{D}_o$ is negligible. This is sometimes also called magneto-quasistationary (MQS) field.

c) **The eddy-current-free quasistationary field:**

$$|\kappa\vec{E}_i| \ll |\vec{S}_o| \tag{A.10}$$

This approximation is also called electro-quasistatic (EQS) approximation. Compared to the quasistatic approximation, in which both components $\kappa\vec{E}_o$ and $\kappa\vec{E}_i$ of the conduction current density are neglected, the eddy-current-free quasi-stationary

approximation considers the current density which is produced by $\vec{E}_o$. This approximation is often valid for conductors with moderate conductivity, i.e., semiconductors. If the permeability μ is constant, the range of the valid electro-quasistatic field intensities can be strictly specified. The induced current density $\kappa\vec{E}_i$ can be neglected if the following conditions are met everywhere in the field domain, additionally to $\omega \ll \omega_q$:

$$\omega \ll \omega_q^2\tau_e \Leftrightarrow d \ll \delta, \tag{A.11}$$

where d is the diameter of the field domain Ω and δ denotes the skin depth which is given by

$$\delta = \sqrt{\frac{2}{\omega\mu\kappa}}. \tag{A.12}$$

If the conductivity and the permittivity are not constant, the minimum of the dielectric relaxation time τ_e constant cannot be greater than $\varepsilon_{max}/\kappa_{max}$.

Table A.1: Classification of the quasistationary fields under different material behaviours

Classification	Conditions	Equivalent Conditions	Simplified First Maxwell's Equation
Quasistatic field	$\|\kappa\vec{E}_o\| \ll \|j\omega\vec{D}_o\|$	$\kappa \ll \omega\varepsilon$	$\text{curl}\vec{H} = \vec{J}_s + j\omega\vec{D}_o$
MQS	$\|j\omega\vec{D}_o\| \ll \|\kappa\vec{E}_o\|$	$\omega\varepsilon \ll \kappa$	$\text{curl}\vec{H} = \kappa\vec{E} + \vec{J}_s$
EQS	$\|\kappa\vec{E}_i\| \ll \|\vec{S}_o\|$	$\omega \ll \omega_q^2\tau_e$	$\text{curl}\vec{H} = \kappa\vec{E}_o + \vec{J}_s + j\omega\vec{D}_o$

Literature

References

[1] ABB. *Technical Information: Physical Properties of Zinc Oxide Varistors, Edition 4*. Tech. rep.

[2] R. Abd-Rahman, A. Haddad, and N. Harid. „Dynamic Non-linear Model for Polluted Outdoor Insulators". In: *Proceedings of 7th International Symposium on High Voltage Engineering*. 22-26 August 2011, Hannover Germany.

[3] R. Abd-Rahman, A. Haddad, N. Harid, and H. Griffiths. „Stress Control on Polymeric Outdoor Insulator Using Zinc Oxide Microvaristor Composite". In: *IEEE Transactions on Dielectrics and Electrical Insulation* 19.2 (April 2012), pp. 705–713. DOI: 10.1109/TDEI.2012.6180266.

[4] M. Babuder. „Accelerated Ageing of High-Voltage ZinC Oxide Resistors by Repeated Application of High Current Impulses". In: *International Symposium on High Voltage Engineering*. Yokohama, Japan, 1993.

[5] G. Bachmaier. „Elektrisch nichtlineare Kompositkeramik auf der Basis von Zinkoxid als Füllstoff in einer Polymermatrix zum Steuern elektrischer Felder". MA thesis. Fachhochshule München, Fachbereich Elektrotechnik, 1999.

[6] M. Björkman and K. Holmström. „Global Optimization Using the DIRECT Algorithm in Matlab". In: *AMO - Advanced Modeling and Optimization* 1.2 (1999), pp. 17–37.

[7] G. Blatter and F. Greuter. „Electrical Breakdown at Semiconductor Grain Boundaries". In: *Physical Review B* 34.12 (12 1986), pp. 8555–8572. DOI: 10.1103/PhysRevB.34.8555.

[8] L. Bo and R. S. Gorur. „Modeling Flashover of AC Outdoor Insulators under Contaminated Conditions with Dry Band Formation and Arcing". In: *IEEE Transactions on Dielectrics and Electrical Insulation* 19.3 (2012), pp. 1037–1043. ISSN: 1070-9878. DOI: 10.1109/TDEI.2012.6215110.

[9] B. Boettcher, G. Malin, and R. Strobl. „Stress Control System for Composite Insulators based on ZnO-Technology". In: *Transmission and Distribution Conference and Exposition, 2001 IEEE/PES*. Vol. 2. 2001, pp. 776–780. DOI: `10.1109/TDC.2001.971336`.

[10] S. A. Boggs. „The Increasing Role of Modeling in High Voltage and Materials Engineering". In: *IEEE Electrical Insulation Magazine* 26.5 (2010), pp. 8–22. ISSN: 1089-084X. DOI: `10.1109/MEI.2010.5585004`.

[11] T. Braunsberger, A. Dziubek, W. Kodoll, U. Schümann, and M. Kurrat. „PD between Water Drops Influencing Hydrophobic Processes on SI and EP-Resin Systems". In: *The XIIIth International Symposium on High Voltage Engineering Delft University of Technology, Netherlands*. August, 2003.

[12] T. Braunsberger, S. Feier-Iova, V. Hinrichsen, and M. Kurrat. „Partial Discharge Processes at Sessile Water Drops on Insulating Surfaces". In: *XVI International Conference on Gas Discharges and their Applications, Xi'an, China*. Vol. 1. 11-15 Semptember 2006.

[13] W. Bruckner, W. Moldenhauer, and K.-H. Bäther. „Time Dependence of Degradation in ZnO Varistors". In: *Phys. Status Solidi (a)* 70.1 (1982), pp. 167–175.

[14] John C. Butcher. *Numerical Methods for Ordinary Differential Equations*. John Wiley & Sons, 2003.

[15] T. Christen, L. Donzel, and F. Greuter. „Nonlinear Resistive Electric Field Grading part 1: Theory and Simulation". In: *IEEE Electrical Insulation Magazine* 26.6 (2010), pp. 47–59. ISSN: 0883-7554. DOI: `10.1109/MEI.2010.5599979`.

[16] T. Christen, L. Donzel, F. Greuter, and M. Saltzer. „Fundamentals of Resistive Field Grading". In: *Proceedings: Feldsteuernde Isoliersysteme (ETG-FB 131)*. 22.11.2011-23.11.2011 at Darmstadt, Deutschland.

[17] K. L. Chrzan and F. Moro. „Concentrated Discharges and Dry Bands on Polluted Outdoor Insulators". In: *IEEE Transactions on Power Delivery* 22.1 (2007), pp. 466–471. ISSN: 0885-8977. DOI: `10.1109/TPWRD.2006.887093`.

[18] David R Clarke. „Varistor Ceramics". In: *Journal of the American Ceramic Society* 82.3 (1999), pp. 485–502.

[19] M. Clemens. „Large System of Equations in a Discrete Electromagnetism: Formulation and Numerical Algorithm". In: *IEEE Proc.-Sci. Meas. Technol.* Vol. 152. 2. March 2005.

[20] M. Clemens, T. Steinmetz, and D. Weida. „Numerische Simulation elektro-quasistatischer Hochspannungsfelder mit MEQSICO". In: *Forschungsmagazin der Helmut-Schmidt-Universität, 17. Jahrgang* (Ausgabe 2007), pp. 8–15.

[21] M. Clemens, M. Wilke, Benderskaya G., H. De Gersem, W. Koch, and T. Weiland. „Transient Electro-Quasi-Static Adaptive Simulation Schemes". In: *IEEE Transactions on Magnetics* 40.2 (2004), pp. 1294–1297.

[22] J. Debus and V. Hinrichsen. „Microvaristor Filled Stress Grading Systems For High-Voltage Rotating Electrical Machines". In: *22nd Nordic Insulation Symposium*. 13. - 15. Juni 2011.

[23] J. Debus, V. Hinrichsen, and J. M. Seifert. „Improved Performance of Silicone Rubber Composite Insulators by Microvaristor Filled Components". In: *ISH*. 2011, Hannover, Germany.

[24] J. Debus, V. Hinrichsen, J. M. Seifert, and M. Hagemeister. „Investigation of Composite Insulators with Microvaristor Filled Silicone Rubber Components". In: *2010 International Conference on Solid Dielectrics*. July 4-9, 2010, pp. 1–4.

[25] Srikanth Devanathan and Patrick N. Koch. „Comparison of Meta-Modeling Approaches for Optimization". In: *ASME 2011 International Mechanical Engineering Congress and Exposition*. American Society of Mechanical Engineers. 2011, pp. 827–835.

[26] H. F. Dienel. „Silicon Carbide Varistors: Properties and Construction". In: *Bell Lab. Rec.* 34 (1956), pp. 407–411.

[27] H. K. Dirks. „Quasi-Stationary Fields for Microelectronic Applications". In: *Electrical Engineering (Archiv für Elektrotechnik)* 79.2 (1996), pp. 145–155.

[28] L. Donzel, T. Christen, R. Kessler, F. Greuter, and H. Gramespacher. „Silicon Composite for HV Applications based on Microvaristors". In: *Proceeding of 2004 International Conference on Solid Dielectrices*. Vol. 1. July 5-9, 2004, pp. 403–406. DOI: 10.1109/ICSD.2004.1350376.

[29] L. Donzel, F. Greuter, and T. Christen. „Nonlinear Resistive Electric Field Grading Part 2: Materials and Applications". In: *Electrical Insulation Magazine, IEEE* 27.2 (2011), pp. 18–29. ISSN: 0883-7554. DOI: 10.1109/MEI.2011.5739419.

[30] L. Donzel and H Hagemeister. „Mikrovaristor-Silikon-Compounds für die nichtlineare elektrische Feldsteuerung". In: *1. Burghauser Isolierstoff Kolloquium*. 2007.

[31] K. Eda. „Zinc Oxide Varistors". In: *IEEE Electrical Insulation Magazine* 5.6 (1989), pp. 28–30. ISSN: 0883-7554. DOI: 10.1109/57.44606.

[32] L. Egiziano, V. Tucci, C. Petrarca, and M. Vitelli. „A Galerkin Model to Study the Field Distribution in Electrical Components Empoying Nonlinear Stress Grading Materials". In: *IEEE Transactions on Dielectrics and Electrical Insulation* 6.6 (Dec. 1999), pp. 765–773.

[33] AiF-Mitgliedsvereinigung (MV) Elektrotechnik. „Mikrovaristoren in polymeren Isoliersystemen - Klärung der Einsatzmöglichkeiten in der elektrischen Energietechnik und Untersuchungen zum Betriebsverhalten". In: *Antrag N11542/06*. 2006.

[34] O. Elsässer, F. Messerer, and K. Feser. „Flashover Behavior of Semiconducting Glazed Insulators under Positive Lightning Impulse Stress at Different Climatic Conditions". In: *2000 Annual Report Conference on Electrical Insulation and Dielectric Phenomena*. Vol. 1. 2000, pp. 203–206.

[35] R. Erzinger. „Nichtlineare elektrische Leitfähigkeit von dotierter Zinkoxid-Keramik". PhD thesis. Technische Universität München, 1982.

[36] S. Feier-Iova. „The Behaviour of Water Drops on Insulating Surface Stressed by Electric Field". PhD thesis. Fachbereich Elektrotechnik und Informationstechnik, Technische Universität Darmstadt, 2009.

[37] S. C. Fernando, K. L. Wong, and W. S. T. Rowe. „Detection of Corona and Dry-Band Arc Discharges on Nano-Composite Epoxy Insulators using RF Sensing". In: *Progress In Electromagnetics Research* 125 (2012), pp. 237–254. DOI: `10.2528/PIER12011201`.

[38] A. Forrester, A. Sobester, and Kea. „Multi-Fidelity Optimization via Surrogate Modelling". In: *Proceedings of the Royal Scociety A* 463.463 (2007), pp. 3251–3269. DOI: `doi:10.1098/rspa.2007.1900`.

[39] Alexander Forrester, Andras Sobester, and Andy Keane. *Engineering Design via Surrogate Modelling: A Practical Guide*. John Wiley & Sons, 2008.

[40] Jörg M. Gablonsky. „Modifaction of the DIRECT Algorithm". PhD thesis. Department of Mathematics, Graduate Faculty of North Carolina State University, 2001.

[41] K. M. Geißel. „Untersuchung der Auswirkung mikrovaristorgefüllter Silikone auf die elektrische Charakteristik von Verbundisolatoren". MA thesis. Fachbereich Elektrotechnik und Informationstechnik, Technische Universität Darmstadt, 2012.

[42] Görlich. *Versuchsbericht Nr. 17/13: Überschlagverhalten von Verbundisolatoren mit innerer Feldsteuerschicht bei elektrolytischer Fremdschichtbelastung*. Tech. rep. FG Hochspannungstechnik/Werkstoffe der Elektrotechnik, Hochschule Zittau/Görlitz, 21.11.2013.

[43] R.S. Gorur, E.A. Cherney, R. Hackam, and T. Orbeck. „The Electrical Performance of Polymeric Insulating Materials under Accelerated Aging in a Fog Chamber". In: *IEEE Transactions on Power Delivery* 3.3 (1988), pp. 1157–1164. ISSN: 0885-8977. DOI: 10.1109/61.193898.

[44] H. Gramespacher, J. Svahn, F. Greuter, and T. Christen. „Microvaristor Based Field Grading Elements for HV Terminations". In: *13th International Symposium on High Voltage Engineering*. 2003.

[45] F. Greuter and G. Blatter. „Electrical Properties of Grain Boundaries in Polycrystalline Compound Semiconductors". In: *Semiconductor Science and Technology* 5.2 (1990), pp. 111–136.

[46] F. Greuter, M. Siegrist, P. Kluge-Weiss, R. Kessler, L. Donzel, R. Loitzl, and H.J. Gramespacher. „Microvaristors: Functional Fillers for Novel Electroceramic Composites". English. In: *Journal of Electroceramics* 13.1-3 (2004), pp. 739–744. ISSN: 1385-3449. DOI: 10.1007/s10832-004-5185-9.

[47] Z. Guan, L. Wang, B. Yang, X. Liang, and Z. Li. „Electric Field Analysis of Water Drop Corona". In: *IEEE Transactions on Power Delivery* 20.2 (2005), pp. 964–969. ISSN: 0885-8977. DOI: 10.1109/TPWRD.2004.837672.

[48] T. K. Gupta. „Application of Zinc Oxide Varistors". In: *Journal of the American Ceramic Society* 73.7 (1990), pp. 1817–1840.

[49] T. K. Gupta and H. Pietsch. „Method of Producing Homogeneous ZnO Nonlinear Powder Compositions". Pat. US4297250. 1981.

[50] H. M. Gutmann. „A Radial Basis Function Method for Global Optimization". In: *Journal of Global Optimization* 19.3 (2001), pp. 201–227. DOI: 10.1023/A:1011255519438.

[51] R. Hackam. „Outdoor High Voltage Polymeric Insulators". In: *1998. Proceedings of 1998 International Symposium on Electrical Insulating Materials*. 1998, pp. 1–16. DOI: 10.1109/ISEIM.1998.741674.

[52] A. Haddad, H. Griffiths, and R. T. Waters. „Principles of Anti-Fog Design for Polymeric Insulators". In: *2007. ICSD '07. IEEE International Conference on Solid Dielectrics*. 2007, pp. 302–305. DOI: 10.1109/ICSD.2007.4290812.

[53] R. Hartings. „Electric Fields Along a Post Insulator: AC-Measurements and Calculations". In: *IEEE Transactions on Power Delivery* 9.2 (1994), pp. 912–918. ISSN: 0885-8977. DOI: 10.1109/61.296274.

[54] Hermann A. Haus, Jamens Melcher, Markus Zahn, and Manuel L. Silva. „Electromagnetic Fields and Energy". In: *MIT OpenCourseWare: Massachusetts Institute of Technology*. http://ocw.mit.edu/resources/res-6-001-electromagnetic-fields-and-energy-spring-2008 (Accessed 17 Nov, 2014).: Springer, 2008.

[55] G. Hawe and J. Sykulski. „A Hybrid One-Then-Two Stage Algorithm for Computationally Expensive Electromagnetic Design Optimization". In: *COMPEL: The International Journal for Computation and Mathematics in Electrical and Electronic Engineering* 26.2 (2007), pp. 236–246.

[56] David Derek Hinde. „Corona Discharge on the Surface of High Voltage Composite Insulators". PhD thesis. Faculty of Built Environment, Engineering, School of Electrical, and Electronic Systems, Queensland University of Technology, Australia, 2009.

[57] V. Hinrichsen and A. Küchler. „Field Grading Fundamentals". In: *ETG-Fachbericht 131: Feldsteuernde Isoliersysteme.* 22.-23.11.2011 in Darmstadt.

[58] R. Hiptmair, F. Krámer, and J. Ostrowski. „A Robust Maxwell Fomulation for All Frequencies". In: *IEEE Transactions on Magnetics* 44.6 (2008), pp. 682–685.

[59] B. Husslage, G. Rennen, E. R. van Dam, and D. den Hertog. „Space-Filling Latin Hypercube Designs for Computer Experiments". In: *Optimization and Engineering* 12(4) (2011), pp. 611–630.

[60] *IEC 60093: Method of Test for Insulating Material for Electrical Purposes: Volume Resistivity and Surface Resistivity of Solid Electrical Insulating Materials, 1980.* German. Dec. 1993.

[61] *IEC 60507: Artificial Pollution Test on High-Voltage Ceramics and Glass Insulators to be used on A.C. Systems.* 2012.

[62] *IEC standard 60137: Insulated Bushings for Alternating Voltages above 1000 V, edition 6.0.* 2008.

[63] S. Ishibe, M. Mori, M. Kozako, and M. Hikita. „A New Concept Varistor With Epoxy/Microvaristor Composite". In: *IEEE Transactions on Power Delivery* 29.2 (2014), pp. 677–682. ISSN: 0885-8977. DOI: `10.1109/TPWRD.2013.2281850`.

[64] M. E. Johnson, L. M. Moore, and D. Ylvisaker. „Minmax and Maximin Distance Designs". In: *Journal of Statistical Planning and Inference* 26.2 (1990), pp. 131–148.

[65] D. R. Jones. „A Taxonomy of Global Optimization Method based on Response Surfaces". In: *Journal of Global Optimization* 21 (2001), pp. 345–383. DOI: `10.1023/A:1012771025575`.

[66]   D. R. Jones. „Direct Global Optimization Algorithm". In: *Encyclopedia of Optimization*. Springer US, 2001, pp. 431–440. DOI: 10.1007/0-306-48332-7_93.

[67]   D. R. Jones, C. D. Perttunen, and B. E. Stuckman. „Lipschitzian Optimization without the Lipschitz Constant". In: *Journal of Optimization Theory and Applications* 79.1 (October 1993), pp. 157–181.

[68]   D. R. Jones, M. Schonlau, and W. J. Welch. „Efficient Global Optimization of Expensive Black-Box Functions". In: *Journal of Global Optimization* 13 (1998), pp. 455–492.

[69]   G.G. Karady. „Flashover Mechanism of Non-ceramic Insulators". In: *IEEE Transactions on Dielectrics and Electrical Insulation* 6.5 (1999), pp. 718–723. ISSN: 1070-9878. DOI: 10.1109/94.798128.

[70]   M. C. Kennedy and A. O' Hagan. „Predicting the Output from a Complex Computer Code when Fast Approximations are Avaiable". In: *Biometrika* 87.1 (2000), pp. 1–13.

[71]   S. Koziel, S. Ogurtsov, I. Couckuyt, and T. Dhaene. „Cost-Efficient Electromagnetic-Simulation-Driven Antenna Desing using Co-Kriging". In: *Microwaves, Antennas and Propagation, IET* 6.14 (2012), pp. 1521–1528.

[72]   A. Küchler. *Hochspannungstechnik: Grundlagen - Technologie - Anwendungen.* Springer-Verlag Berlin Heidelberg, 2009.

[73]   J Lang. *Adaptive Multilevel Solution of Nonlinear Parabolic PDE System: Theory, Algorithm and Applications.* Springer, Berlin, Hedelberg, New York, 2001.

[74]   L. Lebensztajn, C.A.R. Marretto, M.C. Costa, and J. Coulomb. „Kriging: A Useful Tool for Electromagnetic Device Optimization". In: *IEEE Transactions on Magnetics* 40.2 (2004), pp. 1196–1199. ISSN: 0018-9464. DOI: 10.1109/TMAG.2004.824542.

[75]   L. M. Levinson. „Advance in Varistor Technologie (Ceramics Transactions)". In: 3 (1989).

[76]   L. M. Levinson. *Electronic Ceramics: Properties: Devices, and Applications.* Electrical and Computer Engineering. Taylor & Francis, 1987. ISBN: 9780824777616.

[77]   M. Li, G. Li, and S. Azarm. „A Kriging Metamodel Assisted Multi-Objective Genetic Algorithm for Design Optimization". In: *Journal of Mechanical Designs* 130 (2008). DOI: 10.1115/1.2829879.

[78]   J.S.T. Looms. *Insulators for High Voltages.* IEE power engineering series: 7. Peregrinus, 1988.

[79]   ABB Switzerland Ltd. *Microvaristor Powder Certificate, Document No.: 1HC0088933.* Tech. rep. 2012.

[80] S. Matsui, Y. Suzuki, N. Nakashima, F. Kasaki, O. Fujii, and E. Matsuda. „State of the Art of Semiconducting Glazed Insulators for Tranmission Line in Heavily Contaminated Area". In: *Proceedings of the 5th International Conference on Properties and Applications of Dielectric Material.* Vol. 2. May , 1997, pp. 726–729.

[81] M. Matsuoka. „Nonohmic Properties of Zinc Oxide Ceramics". In: *J. Appl. Phys.* 10.6 (1971), pp. 736–746.

[82] M. Matsuoka, T. Masuyama, and Y. Iida. „Voltage Nonlinearity of Zinc Oxide Ceramics Doped with Alkali Metal Oxide". In: *Japanese Journal of Applied Physics* 8.10 (1969), p. 1275.

[83] M. D. McKay, R. J. Beckman, and W. J. Conover. „A Comparison of Three Methods for Selecting Values of Input Variables in the Analysis of Output from a Computer Code". In: *Technometrics, Special 40th Anniversary Issue* 42.1 (Feb. 2000), pp. 55–61.

[84] Mohammad Reza Meshkatoddini. „Metal Oxide ZnO-Based Varistor Ceramics". In: *Advances in Ceramics - Electric and Magnetic Ceramics, Bioceramics, Ceramics and Environment* (2011). DOI: 10.5772/23601.

[85] Marcin Molga and Czeslaw Smutnicki. „Test Function for Optimization Needs". In: *Test Function for Optimization Needs* (2005).

[86] V. M. Moreno and R.S. Gorur. „Corona-induced Degradation of Nonceramic Insulator Housing Materials". In: *2001 Annual Report. Conference on Electrical Insulation and Dielectric Phenomena.* 2001, pp. 640–643. DOI: 10.1109/CEIDP.2001.963625.

[87] V.M. Moreno and R.S. Gorur. „Effect of Long-term Corona on Non-ceramic Outdoor Insulator Housing Materials". In: *IEEE Transactions on Dielectrics and Electrical Insulation* 8.1 (February 2001), pp. 117–128. ISSN: 1070-9878. DOI: 10.1109/94.910434.

[88] M. D. Morris and T. J. Mitchell. „Exploratory Designs for Computational Experiments". In: *Journal of Statistical Planning and Inference* 43.3 (1995), pp. 381–402.

[89] K. Mukae, K. Tsuda, and I. Nagasawa. „Non-Ohmic Properties of ZnO-Rare Earth Metal Oxide-Co_3O_4 ceramics". In: *Japanese Journal of Applied Physics* 16(8) (1977).

[90] D. Müllegger and J. Kindersberger. „Temperature Dependent Electrical Characteristic of ZnO Microvaristor Powder". In: *ETG Workshop "Werkstoffe mit nichtlinearen dielektrischen Eigenschaften".* ETG-Fachbericht 110. VDE-Verlag Berlin - Offenbach, 2008, pp. 45–48.

[91] Daniel Müllegger. „Untersuchung und Simulation der elektrischen Eigenschaften von Microvaristormaterialien". PhD thesis. Fakultät für Elektrotechnik und Informationstechnik der Technischen Universität München, 2012.

[92] J. Ozawa. „Degradation of Zinc Oxide Elements by Lightning and Switching Surges". In: *Cigré 33-87 (WG 06) 10 IWD* (1987).

[93] H. R. Philipp and L. M. Levinson. „Degradation Phenomena in Zinc Oxide Varistors: A Review". In: *Advances in ceramics: 7.* 1983.

[94] A. J. Phillips, D. J. Childs, and H. M. Schneider. „Aging of Non-Ceramic Insulators due to Corona from Water Drops". In: *IEEE Transactions on Power Delivery* 14.3 (1999), pp. 1081–1089. ISSN: 0885-8977. DOI: 10.1109/61.772357.

[95] Andrew J. Phillips et al. „Electric Fields on AC Composite Tranmission Line Insulators". In: *IEEE Transactions on Power Delivery* 23.2 (April 2008), pp. 823–830.

[96] G. E. Pike. „Electronic Properties of ZnO Varistors: A New Model". In: *Symposium B Grain Boundaries in Semiconductors.* Ed. by G. E. Pike Edited H. J. Leamy and C. H. Seager. Vol. 5. MRS Proceedings. 1981. DOI: 10.1557/PROC-5-369.

[97] H. Pohlheim. *Examples of Objective Function for GEATbx version 3.7.* Tech. rep. November 2005.

[98] N. Quttineh and K. Holmström. „The Influence of Experimental Designs on the Performance of Surrogate Model based Costly Global Optimization Solvers". In: *Studies in Informatics and Control* 18 (2009), pp. 87–95.

[99] Rahisham-Abd Rahman. „Investigation of ZnO Microvaristor for Stress Control on Polymeric Outdoor Insulators". PhD thesis. School of Engineering, Cardiff University, August 2012.

[100] U. van Rienen, M. Clemens, and T. Weiland. „Simulation of Low-Frequency Fields on High-Voltage Insulators with Light Contaminations". In: *IEEE Transactions on Magnetics* 32.2 (May 1996), pp. 816–819.

[101] U. van Rienen, J. Flehr, U. Schreiber, S. Schulze, U. Gimsa, W. Baumann, D. G. Weiss, J. Gimsa, R. Benecke, and Pau H.-W. „Electro-Quasistatic Simulation in Bio-Systems Engineering and Medical Engineering". In: *Advances in Radio Science: Kleinheubacher Berichte (Katlenburg-Lindau: Copernicus)* 3 (2005), pp. 39–49.

[102] John S. Rigden. *Macmillan Encyclopedia of Physics.* Simon & Schuster, New York, 1996.

[103]   S. M. Rowland. „Prevention of Dry-Band Arc Damage on ADSS Cables“. In: *IEEE Transactions on Dielectrics and Electrical Insulation* 13.4 (August 2006), pp. 765–772.

[104]   K. Sato and Y. Takada. „A Mechanism of Degradation in Leakage Currents through ZnO Varistors“. In: *Journal of Applied Physics* 53.12 (1982), pp. 8819–8826.

[105]   F. Schmuck. *Use of Corona Rings to Control the Electrical Field along Transmission Line Composite Insulators*. Tech. rep. Technical Brochure 284. 2005.

[106]   J. Schulte-Fischedick and J. M. Seifert. „Design and Test of High Voltage Insulators“. In: *Conference on Silicone Insulation*. Jun 6-7, 2013.

[107]   J. M. Seifert and M. Clemens. „Practical Experiences with Field Controlled Composite Insulators in Production and Application“. In: *ETG-Fachbericht 131: Feldsteuernde Isoliersysteme*. 22.-23.11.2011.

[108]   J. M. Seifert, V. Hinrichsen, J. Debus, M. Clemens, D. Weida, and M. Hagemeister. „Einsatz von Feldsteuermaterialien in Hochspannungsisolatoren - Potentiale und Risiken“. In: *ETG-Fachbericht 110: Werkstoffe mit nichtlinearen dielektrischen Eigenschaften*. 2008.

[109]   J. M. Seifert and D. Stefanini. „High Pollution Resistant Composite Insulators“. In: *2008 International Conference on High Voltage Engineering and Application*. 2008, pp. 32–35. DOI: 10.1109/ICHVE.2008.4773866.

[110]   Eng Swee Siah, M. Sasena, J. L. Volakis, P.Y. Papalambros, and R.W. Wiese. „Fast Parameter Optimization of Large-Scale Electromagnetic Objects using DIRECT with Kriging Metamodeling“. In: *IEEE Transactions on Microwave Theory and Techniques* 52.1 (2004), pp. 276–285. ISSN: 0018-9480. DOI: 10.1109/TMTT.2003.820891.

[111]   P. P. Silvester and R. L. Ferrari. *Finite Elements for Electrical Engineers*. Cambridge University Press, 1996.

[112]   W. Sima, F. P. Espino-Cortes, E. A. Cherney, and S. H. Jayaram. „Optimization of Corona Ring Design for Long-Rod Insulators using FEM Based Computational Analysis“. In: *Conference Record of the 2004 IEEE International Symposium on Electrical Insulation*. 2004, pp. 480–483. DOI: 10.1109/ELINSL.2004.1380655.

[113]   A. Sobester, S. J. Leary, and A. J. Keane. „On the Design of Optimization Strategies Based on Global Response Surface Approximation Models“. In: *Journal of Global Optimization* 33.1 (2005), pp. 31–59.

[114]   D. Stefanini, J. M. Seifert, M. Clemens, and D. Weida. „Three dimensional FEM electrical field calculations for EHV composite insulator strings". In: *2010 IEEE International Power Modulator and High Voltage Conference (IPMHVC)*. 2010, pp. 238–242. DOI: `10.1109/IPMHVC.2010.5958337`.

[115]   Michael Stein. „Large Sample Properties of Simulations using Latin Hypercube Sampling". In: *Technometrics* 29.2 (1987), pp. 143–151.

[116]   T. Steinmetz, N. Gödel, G. Wimmer, M. Clemens, S. Kurz, and M. Bebendorf. „Efficient Symmetric FEM-BEM Coupled Simulation of Electro-Quasistatic Fields". In: *IEEE Transactions on Magnetics* 44.6 (2008), pp. 1346–1349.

[117]   T. Steinmetz, N. Gödel, G. Wimmer, M. Clemens, S. Kurz, M. Bebendorf, and S. Rjasanow. „Symmetric Coupling of the Finite-Element and the Boundary-Element Method for Electro-Quasistatic Field Simulations". In: *Scientific Computing in Electrical Engineering*. Vol. 11. Mathematics in Industry. Springer Berlin Heidelberg, 2007, pp. 309–315.

[118]   T. Steinmetz, M. Helias, G. Wimmer, L. O. Fichte, and M. Clemens. „Electro-Quasi-Static Field Simulations based on a Discrete Electromagnetism Formulation". In: *IEEE Transactions on Magnetics* 42.4 (2006), pp. 755–758. ISSN: 0018-9464. DOI: `10.1109/TMAG.2006.872488`.

[119]   T. Steinmetz, S. Kurz, and M. Clemens. „Domains of Validity of Quasistatic and Quasistationary Field Approximations". In: *2009 XV International Symposium on Theoretical Engineering (ISTET)*. 2009, pp. 1–5.

[120]   T. Steinmetz, G. Wimmer, and M. Clemens. „Numerical Simulation of Transient Electro-Quasistatic Fields using Advanced Subspace Projection Techniques". In: *Advances in Radio Science* 4 (2006), pp. 49–53.

[121]   R. Strobl, W. Haverkamp, and G. Malin. „A Novel Heat-Shrinkable Medium Voltage Termination System based on Ceramic Stress-Grading Technology". In: *Journal of Electroceramics* 99.26 (2000), pp. 68–73.

[122]   R. Strobl, W. Haverkamp, and G. Malin. „I(O)XSU-F - Neue Generation wärmeschrumpfender Mittelspannungsendverschl/"usse basierend aud ZnO-Technologie". In: *Elektrizitätswirtschaft 99 (2000), Heft 26* (2000), pp. 68–73.

[123]   R. Strumpler, P. K. Weiss, and F. Greuter. „Smart Varistor Composites". In: *8th CIMTEC-World Ceramic Congress and Forum on New Materials, Intelligent Materials and Systems*. 1995, pp. 15–22.

[124] S. Wang, X. Liang, and L. Huang. „Experimental Study on the Pollution Flashover Mechanism of Polymer Insulators". In: *2000 IEEE Power Engineering Society Winter Meeting.* Vol. 4. 2000, pp. 2830–2833. DOI: 10.1109/PESW.2000.847332.

[125] D. Weida, S. Böhmelt, and M. Clemens. „Design of ZnO Microvaristor End Corona Protection for Electrical Machines". In: *Conference Record of the 2010 IEEE International Symposium on Electrical Insulation (ISEI).* 2010, pp. 1–4. DOI: http://dx.doi.org/10.1109/ELINSL.2010.5549550.

[126] D. Weida, C. Richter, and M. Clemens. „Design of ZnO Microvaristor Material Stress-Cone for Cable Accessories". In: *IEEE Transactions on Dielectrics and Electrical Insulation* 18.4 (2011), pp. 1262–1267. ISSN: 1070-9878. DOI: 10.1109/TDEI.2011.5976125.

[127] D. Weida, T. Steinmetz, and Clemens. „Electro-Quasistatic High-Voltage Field Simulations of Insulator Structures Coverd with Thin Resistive Pollution or Nonlinear Grading Material". In: *2008 IEEE International Power Modulators and High Voltage Conference.* May 27-31, 2008, pp. 580–583.

[128] D. Weida, T. Steinmetz, and M. Clemens. „Electro-Quasistatic High Voltage Field Simulations of Large Scale Insulator Structures Including 2D Models for Nonlinear Field-Grading Material Layers". In: *IEEE Transactions on Magnetics* 45.3 (2009), pp. 980–983. ISSN: 0018-9464. DOI: 10.1109/TMAG.2009.2012492.

[129] D. Weida, T. Steinmetz, M. Clemens, and J. Seifert. „Benefits of Higher Order Elements for Electrostatic Simulations of Large-Scale 3D Insulator Structures". In: *29th IEEE Electrical Insulation Conference (EIC 2009).* 2009, pp. 558–561.

[130] D. Weida, T. Steinmetz, M. Clemens, J. Seifert, and V. Hinrichsen. „Electro-Quasistatic High-Voltage Field Simulation of Large Scale 3D Insulator Structures Including 2D Models for Conductive Pollution Layers". In: *Advanced Computer Techniques in Applied Electromagnetics, IOS Press* (2008), pp. 431–437.

[131] T. Weiland. „Time Domain Electromagnetic Field Computation with Finite Difference Methods". In: *International Journal of Numerical Modelling: Electronic Networks, Devices and Fields* 9 (1996), pp. 259–319.

[132] S. Xiao, M. Rotaru, and J. K. Sykulski. „Exploration versus Exploitation Using Kriging Surrogate Modelling in Electromagnetic Design". In: *COMPEL: The International Journal for Computation and Mathematics in Electrical and Electronic Engineering* 31.5 (2012), pp. 1541–1551.

Publications published by this Author

[P1]   F. Lehretz, H. Ye, Heinz Denndörfer, J. Seifert, and M. Clemens. „Investigation of Electrical Properties of Microvaristor/Epoxy Resin Compounds". In: *Technische Akademie Esslingen Seminar – Epoxid- und Polyurethanharze in Elektrotechnik und Elektronik - Epoxy and Polyurethane Resins in Electrical and Electronic Engineering.* Ostfildern, Germany, 06.05.2014 - 08.05.2014.

[P2]   D. Weida, J. Nevoigt, H. Ye, M. Clemens, D. Stefanini, and J. M. Seifert. „Effects of Microvaristor Material on the Occurrence of Partial Discharges upon Insulators in Rain Test". In: *2010 IEEE International Power Modulator and High Voltage Conference (IPMHVC).* 2010, pp. 497–500. DOI: 10.1109/IPMHVC.2010.5958403.

[P3]   H. Ye and M. Clemens. „Optmization of Corona Ring Design for Composite Insulator Strings Using Adaptive Kriging Metamodeling". In: *9th International Symposium on Electric and Magnetic Fields (EMF 2013), Bruges, Belgium.* 23.-25.04.2013.

[P4]   H. Ye, M. Clemens, J. Schulte-Fischedick, and J. Seifert. „Investigation of Electrical Field Grading of Bushings with Microvaristor Filled Epoxy Resin Components". In: *2014 IEEE International Power Modulator and High Voltage Conference (2014 IPMHVC), Santa Fe, USA.* 2014.

[P5]   H. Ye, M. Clemens, and J. Seifert. „Dimension Reduction for the Design Optimization of Large Scale High-Voltage Devices Using Co-Kriging Surrogate Modelling". In: *16th Biennial Conference on Electromagnetic Field Computation (CEFC2014), Annecy, France.* Paper accepted, prepare for publication. 2014.

[P6]   H. Ye, M. Clemens, and J. Seifert. „Optimierung des Koronarings für Langstabisolatoren basierend auf einem adaptive Meta-Modell". In: *5. RCC Fachtagung "Werkstoffe zur Anwendung in der elektrischen Energietechnik unter den besonderen Anforderungen der Hochspannungs-Gleichstrom-Übertragung (HGÜ)", Berlin Germany.* 2012, pp. 191–194.

[P7]   H. Ye, M. Clemens, and J. M. Seifert. „Electroquasistatic Field Simulation for the Layout Improvement of Outdoor Insulators Using Microvaristor Material". In: *IEEE Transactions on Magnetics* 49(5) (2013), pp. 1709–1712. ISSN: 0018-9464. DOI: 10.1109/TMAG.2013.2243423.

Supervised Master Thesis

[T1] Malek Laouti. ,,Elektro-quasistatische Feldsimulation zur Bestimmung des Verhalten von nichtlinearen mikrovaristorgefüllten polymer Isolierstoffen bei äußerer Benetzung durch Wassertropfen". MA thesis. Fachbereich E - Elektrotechnik, Informationstechnik, Medientechnik, Bergische Universität Wuppertal, 2011.